TECHNISCHE
UNIVERSITÄT
DRESDEN

Trapping of chaotic orbits
in 4D symplectic maps

Diplomarbeit
zur Erlangung des wissenschaftlichen Grades
Diplom-Physiker

vorgelegt von

Steffen Lange

geboren am 06.02.1988 in Dresden

Institut für Theoretische Physik
Fachrichtung Physik
Fakultät für Mathematik und Naturwissenschaften
Technische Universität Dresden
2012

Eingereicht am 25. Mai 2012

1. Gutachter: Prof. Dr. Roland Ketzmerick
2. Gutachter: Prof. Dr. Katrin Padberg-Gehle

Abstract

The statistics of Poincaré recurrences for generic Hamiltonian systems exhibits a power-law decay. This is caused by trapping of chaotic orbits close to regular tori. The mechanism of the trapping is well understood for systems with one degree of freedom, but is an open question in higher dimensional systems. In this thesis the global structure of the regular tori in such systems is revealed. Chaotic orbits are found to be trapped in a sticky region at the outer border of these structures. Investigations of the dynamics within the sticky region lead to the conjecture that the sticky region results from a combination of overlapping resonance zones.

Zusammenfassung

Die Statistik der Poincaré-Rückkehrzeiten in generischen Hamilton'schen Systemen zeigt einen algebraischen Abfall, welcher durch das Hängenbleiben von chaotischen Orbits in der Nähe von regulären Tori verursacht wird. Der zugrundeliegende Mechanismus ist gut verstanden für Systeme mit einem Freiheitsgrad, während dies eine offene Frage in höher dimensionalen Systemen darstellt. In der vorliegenden Arbeit wird die globale Struktur der regulären Tori in diesen Systemen aufgedeckt. Es wird weiterhin festgestellt, dass chaotische Orbits in einer Region hängenbleiben, welche sich an der Außenseite der regulären Strukturen befindet. Untersuchungen zur Dynamik innerhalb dieser Region führen zu der Vermutung, dass diese Region aus einer Kombination von überlappenden Resonanzzonen hervorgeht.

Contents

1 Introduction

The dynamics of many classical systems can be expressed in terms of momentum and position coordinates in phase space. In Hamiltonian systems the initial momentum and position coordinates uniquely determine the subsequent coordinates at all times. Despite this fact, there are systems whose dynamics are hard to predict since they depend sensitively on the initial conditions. An example for such a system is the weather, which may change drastically just due to the flap of a butterfly [1]. This behavior is referred to as chaos. The counterpart of chaos is regular motion for which the dynamics of similar initial conditions separate only moderately with increasing time. Chaotic dynamics occur in various fields such as plasma physics, atomic physics, astronomy, and chemistry, see, e.g., reference [2].

A major interest lies in understanding the transport properties of these systems [3–5]. One aspect of transport in closed Hamiltonian systems results from the Poincaré recurrence theorem. Poincaré proved that almost all orbits started in a phase-space region return to that region at some point in time t [6]. The statistics $P(t)$ of Poincaré recurrences t depends on the type of dynamics. For a fully chaotic system the probability that an orbit returns to the initial area is analogous to a coin toss. That is, with probability p the orbit returns within in the next time step and with probability $1-p$ it does not. In this case, the statistics of Poincaré recurrences $P(t)$ decays exponentially [7]

$$P(t) = (1-p)^t \sim \mathrm{e}^{-\ln \frac{1}{1-p} t} \,.$$

However, generic Hamiltonian systems are not fully chaotic but rather mixed. Their phase space contains both chaotic and regular regions. For such a mixed phase space the statistics of Poincaré recurrences exhibit a power-law decay [8],

$$P(t) \sim t^{-\gamma} \,.$$

Thus, $P(t)$ decreases more slowly for a generic system than for a fully chaotic system. The reason for this behavior are chaotic orbits of the mixed system, which are trapped for long times in the vicinity of regular regions and hence have large recurrence times.

This trapping is well understood for systems with one degree of freedom [9]. In the

2D phase space of such systems the regular orbits are located on invariant lines, which form islands surrounded by a chaotic sea. Partial barriers of codimension one exist close to the boundary of the regular islands, which allow for a limited exchange of chaotic phase-space volumes across them. This partial transport barrier causes the trapping of chaotic orbits close to the regular islands. However, this trapping mechanism cannot be generalized to systems with more than one degree of freedom. This is because the manifolds acting as partial barriers in the 2D phase space have codimension greater than one in higher dimensional phase spaces and are therefore no barriers to transport.

The majority of physically relevant systems have more than one degree of freedom and much less is known about these higher dimensional systems. E.g., only a few concepts exist for describing the structure of the regular tori in these systems [10, 11]. The investigation of higher dimensional systems is challenging because a phase space with more than three dimensions is beyond human perception. Thus, the dynamics of these systems is often studied in the lower dimensional frequency space, where chaotic orbits propagate along the Arnold web. This propagation is a combined effect of Arnold diffusion [12], denoting the transport along resonances, and transport perpendicular to resonances due to the overlap of resonance zones [13, 14]. While the latter is also present in 2D systems, the Arnold diffusion is unique to higher dimensional systems. In this context different types of trapping for higher dimensional systems are conjectured: First chaotic orbits are trapped at resonance junctions due to generalized partial barriers surrounding the resonance zones [2]. A possible nature of such barriers is described by Wiggins [15]. Secondly, lines in frequency space with pairwise noble frequency ratio inhibit the propagation along the Arnold web [2, 16]. A further possibility is that, the trapping is caused by the complement of the Arnold web which consists of the most robust tori [2, 17]. Although numerical examples for all of these types of trapping have been found, their relevance and underlying mechanisms remain unclear.

In this thesis the trapping is examined for a coupled standard map with two degrees of freedom. The different types of trapping are explained in chapter 2 along with some basic principles of symplectic maps and trapping mechanisms. Various methods to visualize the 4D phase space are introduced in chapter 3. In chapter 4 visualizations of the phase space lead to an understanding of the global structure of the regular regions. It turns out that these regions form 4D regular islands which are based on one parameter families of regular invariant lines, such as center manifolds. In chapter 5 the trapping of chaotic orbits is investigated by examining trapped orbits first in phase space and then in frequency space. A sticky region is identified which is responsible for the trapping. It is located at the outer border of the regular islands. The transport within the sticky region is quantified and discussed with respect to transport along the

Arnold web and the proposed types of trapping. It is conjectured that an ensemble of overlapping resonance zones is the origin of the sticky region. The thesis concludes with a summary and outlook in chapter 6.

2 Power-law trapping in 2D and 4D

Typical Hamiltonian systems are neither fully integrable nor fully chaotic [18]. One question which arises from this fact is how this coexistence influences chaotic dynamics. This chapter introduces the phenomena related to the trapping of chaotic orbits in Hamiltonian systems. First some fundamental terms such as Hamiltonian systems and chaos are established. Then in Section 2.2 the Poincaré recurrences $P(t)$ are defined, which exhibit a power-law for mixed phase spaces. The explanation of this behavior requires the discussion of the phase-space structure of Hamiltonian systems in Section 2.3. Based on this structure the origin of the power-law is the trapping of chaotic orbits close to regular domains. The trapping mechanism for two dimensions is presented in Section 2.4 and compared to the situation of trapping in four dimensions in Section 2.6, for which much less is known. This motivates further investigations of the 4D case, for which example systems are defined in Section 2.7.

2.1 Hamiltonian dynamics

A Hamiltonian system $H(\boldsymbol{p}(t), \boldsymbol{q}(t), t)$ with N degrees of freedom is a dynamical system defined on the phase space $(\boldsymbol{p}(t), \boldsymbol{q}(t)) \in U \subseteq \mathbb{R}^N \times \mathbb{R}^N$, where $\boldsymbol{p}$ and $\boldsymbol{q}$ denote the momentum and the position vectors, and the time $t \in \mathbb{R}$ [19]. The equations of motion are given by

$$
\begin{aligned}
\dot{\boldsymbol{p}} &= - \frac{\partial H(\boldsymbol{p}, \boldsymbol{q}, t)}{\partial \boldsymbol{q}}, \\
\dot{\boldsymbol{q}} &= \frac{\partial H(\boldsymbol{p}, \boldsymbol{q}, t)}{\partial \boldsymbol{p}}.
\end{aligned}
\tag{2.1}
$$

The dynamics of the Hamiltonian system $H(\boldsymbol{p}(t), \boldsymbol{q}(t), t)$ can be reduced to a $2N$-dimensional Poincaré map F by using a Poincaré section [19, section 1.3]. F is a symplectic map implying that it is an orientation and volume preserving diffeomor-

phism on the phase space

$$
\begin{aligned}
&F \colon U \to U \,, \\
&(\boldsymbol{p}', \boldsymbol{q}') = F(\boldsymbol{p}, \boldsymbol{q}) \,.
\end{aligned}
\tag{2.2}
$$

The iterations of the map F are

$$
\boldsymbol{x}(t) \equiv F^t(\boldsymbol{x}(0)) \equiv \underbrace{F \otimes \ldots \otimes F}_{t}(\boldsymbol{x}_0)
$$

with the abbreviation $\boldsymbol{x} \equiv (\boldsymbol{p}, \boldsymbol{q})$ and the initial vector $\boldsymbol{x}(0) \equiv \boldsymbol{x}_0$. Note that also backward iterations are possible using the inverse map F^{-1}, i.e., $t \in \mathbb{Z}$. A sequence $\{\boldsymbol{x}(t)\}_{t \in \mathbb{N}}$ is called orbit.

Many Hamiltonian systems exhibit chaotic dynamics [19, section 1]. Chaos means that orbits $\boldsymbol{x}(t)$ of the system depend sensitively on their initial condition $\boldsymbol{x}(0)$: a small deviation of the initial condition, $\triangle \boldsymbol{x}_0 = \boldsymbol{x}'(0) - \boldsymbol{x}(0)$ with $||\triangle \boldsymbol{x}_0|| \ll 1$, leads to an orbit $\boldsymbol{x}'(t)$ exponentially diverging from the original one, $||\boldsymbol{x}(t) - \boldsymbol{x}'(t)|| \sim \mathrm{e}^{\lambda t}$. Such an orbit $\boldsymbol{x}(t)$ is called chaotic and regions containing just chaotic orbits are denoted chaotic as well.

This thesis deals with symplectic maps F rather than with the corresponding Hamiltonian systems $H(\boldsymbol{p}(t), \boldsymbol{q}(t), t)$. Therefore, the following introduction to the theory of trapping of chaotic orbits is mostly formulated in terms of such maps. Accordingly, invariant means always invariant with respect to a map. A nice overview of the basic principles of Hamiltonian systems, mixed phase space, and trapping for kicked systems with one degree of freedom is presented by Michler [20, sections 2 and 3].

2.2 Poincaré recurrences

Based on the volume preservation of the symplectic map F, see Eq. (2.2), the Poincaré recurrence theorem can be proved [6, 19, section 7.1.3]. It states that for a symplectic map F with a confined phase space U every region $\Gamma \subseteq U$ is mapped almost completely onto itself in the limits of large times. That is, $\forall \boldsymbol{x}(0) \in \Gamma \backslash \Gamma_0 \colon \exists t \in \mathbb{N} \colon \boldsymbol{x}(t) \in \Gamma$, where the excluded subset $\Gamma_0 \subseteq \Gamma$ is of measure zero. The first time t an orbit returns to its initial region Γ is called Poincaré recurrence. The statistics of Poincaré recurrences $P(t)$ gives the probability that an orbit $\boldsymbol{x}(t)$, with $\boldsymbol{x}(0) \in \Gamma$, has not returned to Γ until time t.

The Poincaré recurrence theorem does not predict anything about the features of $P(t)$, except that it has to be monotonically decreasing with time t. For a fully chaotic

map F_{chaotic} the statistics $P(t)$ is analog to the probability of a coin toss not to end up on "heads" within t flips. It reads $P(t) = 1/2^t$ and hence for such a map F_{chaotic} the statistics $P(t)$ decreases exponentially like $P_{\text{chaotic}}(t) \sim \mathrm{e}^{-\gamma t}$ [21, 22]. On the contrary, the statistics of Poincaré recurrences of a generic symplectic map F exhibits an much slower algebraic decay $P(t) \sim t^{-\gamma}$ [8]. The reason for this different behavior is outlined in the following sections for 2D and 4D maps.

For the well studied case of 2D symplectic generic maps the exponent γ is found to be on average $\gamma \approx 1.5$ [8, 23–29]. For the much less investigated higher dimensional maps, in which the power-law decay of $P(t)$ also occurs, the exponent is found to be $1.1 < \gamma < 1.5$ for 4D, $1.7 < \gamma < 2$ for 6D [30] and $1.3 < \gamma < 5.5$ for maps with $N = 25$ degrees of freedom [31]. Shepelyansky conjectures that for all generic cases the exponent has the universal average value of $\gamma \approx 1.3 \ldots 1.4$, independent of the degrees of freedom [32].

There exist other statistics than $P(t)$, which are based on the Poincaré recurrence theorem. One is the survival time $S(t)$, which denotes the probability that an orbit is still in the initial region Γ at time t. If the initial region for the survival times $S(t)$ is chosen to be the complement of the initial region for the Poincaré recurrences $P(t)$ with a power-law $P(t) \sim t^{-\gamma}$, $S(t)$ will exhibit a power-law $S(t) \sim t^{-(\gamma-1)}$ [7]. The survival time $S(t)$ is for some numerical investigations a more suitable quantity than the Poincaré recurrences $P(t)$.

2.3 KAM theorem

Central for the understanding of the power-law behavior of $P(t)$ is the structure of mixed phase spaces. This structure can be explained by the help of the KAM theorem, which is shortly introduced in this section based on references [19, 33]. The introduction of the necessary fundamental concepts of, e.g., canonical transformations is omitted for brevity and can be found in the above references.

Consider a symplectic map F with N degrees of freedom, whose corresponding time-independent Hamiltonian $H(\boldsymbol{p}, \boldsymbol{q})$ is integrable, i.e., a canonical transformation exists that converts the phase space coordinates $(\boldsymbol{p}(t), \boldsymbol{q}(t))$ to action–angle coordinates $(\boldsymbol{I}(t), \boldsymbol{\Theta}(t)) \in \mathbb{R}^N \times \mathbb{T}^N$. For these new coordinates the equations of motions Eq. (2.1) change to

$$
\begin{aligned}
\dot{\boldsymbol{I}} &= -\frac{\partial H(\boldsymbol{I})}{\partial \boldsymbol{\Theta}} = 0 \,, \\
\dot{\boldsymbol{\Theta}} &= \frac{\partial H(\boldsymbol{I})}{\partial \boldsymbol{I}} =: \boldsymbol{\omega}(\boldsymbol{I}) \,,
\end{aligned}
\tag{2.3}
$$

with the N-dimensional vector of the fundamental frequencies $\boldsymbol{\omega} \in \mathbb{T}^N$. The domain $\mathbb{T} \equiv [0, 2\pi)$ of each angle Θ_i is periodic. Consequently, an initial point $\boldsymbol{x}_0 = (\boldsymbol{p}(\boldsymbol{I}_0, \boldsymbol{\Theta}_0), \boldsymbol{q}(\boldsymbol{I}_0, \boldsymbol{\Theta}_0))$ in phase space leads to an orbit

$$\boldsymbol{x}(t) = (\boldsymbol{p}(\boldsymbol{I}(t), \boldsymbol{\Theta}(t)), \boldsymbol{q}(\boldsymbol{I}(t), \boldsymbol{\Theta}(t)))$$

with

$$\begin{aligned} \boldsymbol{I}(t) &= \boldsymbol{I}_0 \,, \\ \boldsymbol{\Theta}(t) &= (\boldsymbol{\Theta}_0 + \boldsymbol{\omega}(\boldsymbol{I}_0)t) \mod 2\pi \,, \end{aligned} \tag{2.4}$$

where the modulus emphasizes the periodicity of $\mathbb{T}^N$. An orbit $\boldsymbol{x}(t)$ whose dynamics can be expressed as in Eq. (2.4) is called regular orbit. In the phase space of an integrable Hamiltonian all orbits are regular. An orbit of such a regular phase space is located on a N-dimensional invariant manifold representing a torus. A torus is characterized by its fundamental frequencies $\boldsymbol{\omega}(\boldsymbol{I}_0)$ and can be parametrized by the angles $\boldsymbol{\Theta} \in \mathbb{T}^N$ and possesses the tangential vectors $\{\boldsymbol{e}_{\Theta_i}(\boldsymbol{\Theta}_0, \boldsymbol{I}_0)\}_{i=1\ldots N}$ at angles $\boldsymbol{\Theta}_0$. The dual vectors $\{\boldsymbol{e}_{I_i}(\boldsymbol{\Theta}_0, \boldsymbol{I}_0)\}_{i=1\ldots N}$ are the directions in which the actions $\boldsymbol{I}$ change, thus pointing towards other tori.

Generic Hamiltonian systems H are neither integrable nor fully chaotic [18]. They are considered to be a sum

$$H = H_0 + K \cdot H_1$$

of an integrable Hamiltonian H_0 and a perturbation in form of a nonintegrable Hamiltonian $K \cdot H_1$. The parameter $K > 0$ determines the strength of the perturbation. The KAM theorem makes statements about the tori of the phase space of H, depending on their fundamental frequencies $\boldsymbol{\omega}$. That is, frequencies $\boldsymbol{\omega}$ fulfilling a resonance condition

$$\boldsymbol{m} \cdot \boldsymbol{\omega} = 0 \tag{2.5}$$

for any $\boldsymbol{m} \in \mathbb{Z}^N \backslash \{\boldsymbol{0}\}$ are called commensurable and the corresponding torus is called resonant torus. The set of resonant tori is dense in phase space of H_0 but of measure zero. The nonresonant tori with frequencies $\boldsymbol{\omega}$, which do *not* fulfill

$$|\boldsymbol{m} \cdot \boldsymbol{\omega}| > \epsilon(\boldsymbol{\omega})|\boldsymbol{m}|^{-(N+1)} \qquad |\boldsymbol{m}| \equiv \sum_{i=1}^{N} |m_i| \qquad \forall \, \boldsymbol{m} \in \mathbb{Z}^N \backslash \{\boldsymbol{0}\} \tag{2.6}$$

with some prefactor $\epsilon(\boldsymbol{\omega})$ independent of K, are considered to be close to resonant

tori [19, section 7.3]. The remaining set of nonresonant tori, which are not close to resonant tori are of finite measure in the phase space. From Eqs. (2.4) and (2.5) follows that orbits on nonresonant tori are dense on these tori for $t \to \infty$.

For $K = 0$ the phase space of H is identical to the regular phase space of the integrable Hamiltonian H_0. For a small perturbation $K \ll 1$ all resonant tori cease to exist as well as the tori close to them. These regular tori are replaced by chaotic regions and new regular tori of a different topology. The details of this break-up process of resonant tori are presented in Section 2.4.1 for 2D maps and in Section 2.5.1 for 4D maps. The remaining nonresonant tori are deformed but still present in the slightly perturbed phase space. They are referred to as KAM-tori. Hence, the former regular phase space contains now both regular regions with KAM-tori and chaotic regions. Such a phase space is called near-integrable. When the perturbation is increased further, more and more KAM tori break, starting with the tori, which are closest to resonances in the sense of Eq. (2.6). A broken KAM torus is called Cantorus as its remnants are given by Cantor sets in phase space [34].

Note that for systems with an external driving the resonance condition Eq. (2.5) is generalized to

$$\boldsymbol{m} \cdot \boldsymbol{\omega} = 2\pi n \qquad (2.7)$$

with $\boldsymbol{m} \in \mathbb{Z}^N \backslash \{\boldsymbol{0}\}$ and $n \in \mathbb{Z}$. The resonance condition Eq. (2.7) is abbreviated as

$$\underbrace{m_1 : \ldots : m_N}_{N} : n \qquad (2.8)$$

and said to be a coupling resonance if $n = 0$ [13]. The value $|\boldsymbol{m}|$ of the coefficient $\boldsymbol{m}$, see Eq. (2.6), is denoted as order of the resonance.

2.4 Trapping in 2D

The algebraic decay of the statistics of Poincaré recurrences $P(t)$ for generic 2D symplectic maps is well understood, see, e.g., reference [9]. The reason for the power-law behavior of $P(t)$ is that some chaotic orbits stay in confined regions close to the KAM tori for long time spans . This phenomenon is called trapping and these regions are denoted as sticky regions.

In the following sections the mechanism governing the trapping in the 2D phase space is outlined. First the break-up process of resonant tori is examined in Section 2.4.1. Then some of the resulting structures are identified to cause the trapping close to KAM

tori. The so-called partial barriers are investigated in Section 2.4.2.

2.4.1 Resonant tori - Poincaré-Birkhoff theorem

In Section 2.3 only the nonresonant tori are said to survive in case of a small perturbation of the integrable Hamiltonian. In this section the fate of the resonant tori is explained for the 2D phase space by using the Poincaré-Birkhoff theorem in more detail. Furhtermore, structures crucial to the trapping mechanism are introduced.

In the 2D phase space the tori are 1D invariant, closed lines with one fundamental frequency ω, according to Eq. (2.3). Hence, a torus is resonant if its frequency ω is a rational number $\omega = n/m$, see Eq. (2.7). Every orbit on this resonant torus is a periodic orbit with period m. The Poincaré-Birkhoff theorem states that in case of a perturbation not all periodic orbits on this torus cease to exist. A number of $2km$ of them with period m and with some $k \in \mathbb{N}$ remain when the resonant torus breaks up.

In order to discuss the stability properties of these periodic points $\boldsymbol{x}_f$, the Jacobian matrix $DF^m(\boldsymbol{x}_f)$ of the mth iteration of the symplectic map F at each periodic point $\boldsymbol{x}_f$ has to be analyzed. For any symplectic map F the eigenvalues of the Jacobian matrix $DF^m(\boldsymbol{x}_f)$ occur in form of four-tuples $(\lambda, \bar{\lambda}, 1/\lambda, 1/\bar{\lambda})$ [33, section 3.3]. Here two cases are of interest, because there are only two eigenvalues for the $N = 2$ case such that two of the four possibilities coalesce. The first of the two cases is that both eigenvalues of $DF^m(\boldsymbol{x}_f)$ have a real part unequal to zero. Then the linearized dynamics around $\boldsymbol{x}_f$ has a stable and an unstable direction and $\boldsymbol{x}_f$ is called hyperbolic periodic point. The second case is both eigenvalues of $DF^m(\boldsymbol{x}_f)$ being purely imaginary. Then the linearized dynamics around $\boldsymbol{x}_f$ is stable and given by tori centered around $\boldsymbol{x}_f$. Hence, $\boldsymbol{x}_f$ is called an elliptic periodic point. According to the Poincaré-Birkhoff theorem, the $2km$ periodic points remaining from a broken resonant torus form a chain of alternating hyperbolic and elliptic periodic orbits.

The dynamics in the vicinity of an elliptic point can be approxmiated by a Hamiltonian similar to the one presented in Section 2.3 given by an integrable part with a small perturbation. Hence, this subsystem denoted as regular island is again subject to both the KAM theorem and the Poincaré-Birkhoff theorem. This leads to a self-similar structure of islands and their subislands in the phase space, which is referred to as hierarchical structure [35].

From the existence of the stable direction of a hyperbolic point $\boldsymbol{x}_f$ follows the existence of a smooth stable invariant manifold $W^s(\boldsymbol{x}_f) \equiv \{\boldsymbol{x} \in U : \lim_{t \to \infty} F^t \boldsymbol{x} = \boldsymbol{x}_f\}$ in the phase space U. Analogously, for an unstable direction a smooth unstable invariant manifold $W^u(\boldsymbol{x}_f) \equiv \{\boldsymbol{x} \in U : \lim_{t \to \infty} F^{-t} \boldsymbol{x} = \boldsymbol{x}_f\}$ exists. The point-like intersections

of two manifolds $W^s(\boldsymbol{x}_f)$ and $W^u(\boldsymbol{x}'_f)$ are called homoclinic points if $\boldsymbol{x}_f = \boldsymbol{x}'_f$ and heteroclinic points if $\boldsymbol{x}_f \neq \boldsymbol{x}'_f$. These points lead to chaotic dynamics [36]. If the regions of phase space subject to such chaos are extended, then they are usually referred to as chaotic sea.

2.4.2 Trapping mechanism

The manifolds and cantori introduced in Sections 2.3 and 2.4.1 can be used to explain the trapping mechanism in the 2D phase space by constructing partial transport barriers causing chaotic orbits to stay for long times close to regular tori. Every torus of the 2D phase space is a 1D barrier to transport, enclosing a region of the phase space. This implies that a chaotic orbit outside the enclosed region can never cross the torus in order to get to the inside and vice versa. However, in a perturbed system the vicinity of every KAM torus contains 1D invariant manifolds W^s and W^u. When intersecting, these manifolds form a partial barrier with the property to exchange certain small volumes of the phase on either side of them. In addition to the described kind of partial barrier, which is referred to as broken separatrix, the cantori are also relevant partial barriers.

There exists a hierarchy of such partial barriers in the vicinity of the remaining KAM tori. Based on this hierarchy of partial barriers the exponent γ for the Poincaré recurrences $P(t) \sim t^{-\gamma}$ can be estimated. In order to do so, the hierarchical structure is modeled by a random walk on 2D regions of different size, which are separated by partial barriers with different transition probabilities. For details on the modeling see Meiss and Ott [25]. There the exponent γ is obtained as the solution of an exponential equation. In this context log-periodic oscillations of $P(t)$ can be addressed to nonreal solutions of this equation.

2.5 Transition to higher dimensions

Although the power-law of the Poincaré recurrences $P(t)$ is still present in higher dimensional maps, the trapping mechanism outlined in Section 2.4 for 2D maps can not simply be generalized. In order to understand the trapping in higher dimensional maps, this thesis focuses on 4D maps. The reason for this choice is that the structures found in a 4D phase space are much easier to generalize to higher dimensions than the structures found in a 2D phase space. Thus, by understanding the trapping mechanism for the 4D maps it should be possible to understand this mechanism for even higher dimensional maps.

Before presenting conjectures about the mechanism causing the power-law of $P(t)$

in 4D symplectic maps the structural differences of the 4D phase space compared to 2D phase space are pointed out. Therefore, firstly the break-up of the resonant tori is discussed in Section 2.5.1. Then additional structures of the 4D phase space are introduced in Sections 2.5.2 and 2.5.3, which are not present in the 2D phase space.

2.5.1 Resonant tori – structures in phase space

Although the KAM theorem is valid for arbitrary degrees of freedom, there is no genuine generalization of the Poincaré-Birkhoff theorem outlined in Section 2.4.1 to higher dimensions [37, section 2.8]. Therefore, in this section the behavior of the resonant tori of the 4D symplectic map is discussed based on the results from Todesco [11].

The 2D resonant tori of 4D symplectic maps are separated in three classes depending on the character of the fulfilled resonance condition Eq. (2.7)

$$(\boldsymbol{m} \cdot \boldsymbol{\omega}) \mod 2\pi = 0\,.$$

Since the following results are obtained by using normal forms, they are only valid in the vicinity of certain fixed points of the system.

Firstly, the case $\boldsymbol{m} = l \cdot (n, 0)$ with $l \in \mathbb{Z}$ and $n \in \mathbb{N}$ is denoted *single-uncoupled resonance*. Each orbit on a torus with a single-uncoupled resonance is located on n 1D rings along the nonresonant angle Θ_2, which are densely filled by the orbit and which are uniformly distributed along the other angle Θ_1 with a distance $\triangle\Theta_1 = 2\pi/n$. Analogously, the case $\boldsymbol{m} = l \cdot (0, n)$ is a single-uncoupled resonance, where the rings of the orbits are along the other angle. Consequently on a torus with a single-uncoupled resonance an infinity of such rings exist, which are referred to as single-uncoupled resonance parabolic fixed lines of period n. In case of a perturbation only two of these fixed lines remain, one being elliptic and the other hyperbolic. As for the fixed points of a 2D map the terms elliptic and hyperbolic state that a fixed line is stable or unstable under small deviations of initial conditions.

The second case $\boldsymbol{m} = l \cdot (n_1, n_2)$ with $l, n_1 \in \mathbb{Z}$ and $n_2 \in \mathbb{N}$ is denoted *single-coupled resonance*. Each orbit on a torus with a single-coupled resonance is located on a 1D line, which is filled densely by the orbit. Consequently, on a torus with a single-coupled resonance an infinity of such lines exist, which are referred to as single-coupled resonance parabolic fixed lines. In case of a perturbation only two of these fixed lines remain, one being elliptic and the other hyperbolic.

The last case $\boldsymbol{m} = l_1 \cdot (n_{11}, n_{12}) + l_2 \cdot (n_{21}, n_{22})$ with $l_1, l_2, n_{11}, n_{21} \in \mathbb{Z}$ and $n_{12}, n_{22} \in \mathbb{N}$ is denoted *double resonance*. Each orbit on a torus with a double resonance consists of $n_{11}n_{22}$ points. Consequently, on a torus with a double resonance an infinity of such

periodic orbits exist, which are referred to as parabolic fixed points of period $n_{11}n_{22}$. In case of a perturbation only four of these periodic orbits remain. Todesco describes different options for the stability of these orbits, which are omitted here for brevity.

Furthermore, single-coupled and single-uncoupled resonances are referred to as rank-1 resonances, whereas a double resonance is also referred to as rank-2 resonance.

2.5.2 Center manifold and NHIM

In a 4D phase space a fixed point is not just elliptic or hyperbolic but can rather combine two properties, for example giving an elliptic–hyperbolic fixed point. This refers to the two pairs of eigenvectors of the Jacobian matrix belonging to the fixed point. The chaotic and regular structures arising from such fixed points are discussed in this section based on the center manifold theorem, see, e.g., reference [38, section 2.7]. The theorem is valid for general dynamical systems, but applied here to the special case of 4D symplectic maps.

The hyperbolic component of an elliptic–hyperbolic fixed point $\boldsymbol{x}_f$ to smooth 1D invariant manifolds $W^s(\boldsymbol{x}_f)$ and $W^u(\boldsymbol{x}_f)$ known from the 2D case in Section 2.4.1. The stable manifold $W^s(\boldsymbol{x}_f)$ is contracting meaning that all orbits $\boldsymbol{x}(t) \subset W^s(\boldsymbol{x}_f)$ converge to $\boldsymbol{x}_f$ for $t \to \infty$, whereas the unstable manifold $W^u(\boldsymbol{x}_f)$ is expanding meaning that all orbits $\boldsymbol{x}(t) \subset W^u(\boldsymbol{x}_f)$ converge to $\boldsymbol{x}_f$ for negative times $t \to -\infty$.

Regarding the elliptic component of an elliptic–hyperbolic fixed point $\boldsymbol{x}_f$ the center manifold theorem states that there exists locally a 2D invariant manifold C containing $\boldsymbol{x}_f$. Further, the eigenspace of the elliptic eigenvalues is tangential to C at $\boldsymbol{x}_f$. Such a manifold C is referred to as center manifold. The dynamics restricted to a center manifold C is topologically equivalent to the dynamics in the vicinity of a 2D elliptic fixed point. This implies, that the center manifold C consists of a one-parameter family of 1D tori, with action I_0 as parameter. In this sense a center manifold C is equivalent to a regular island around an elliptic fixed point of the 2D phase space, see Section 2.4.1. This statement extends to the perturbed case, for which Graff found the center manifold C to contain a Cantor set of KAM tori of positive measure [39]. Note that there are examples of center manifolds C that exist globally [38]. This is remarkable, since the theorem grants the center manifold C to be defined and smooth only on a local domain, which can even vanish. The discussed properties of an elliptic–hyperbolic fixed point apply correspondingly to the cases of hyperbolic–hyperbolic and elliptic–elliptic fixed points. E.g., two 2D center manifolds exist at an elliptic–elliptic fixed point.

There are special center manifolds, which are called normally hyperbolic invariant manifolds, abbreviated as NHIM, see, e.g., Wiggins [40]. In 4D a NHIM C_{NHIM} is the

center manifold of an elliptic–hyperbolic fixed point. The term *normally hyperbolic* refers to fact that normally to C_{NHIM} the expansion and contraction is much bigger than tangentially to C_{NHIM}, due to the hyperbolic component of the fixed point. For a map with N degrees of freedom a NHIM is the center manifold of a $N - 1$ times elliptic and one times hyperbolic fixed point. Note that the term NHIM applies to any invariant manifold which is normally hyperbolic. However, since their construction via fixed points is more concrete, the following discussions involving NHIMs restrict to this case.

Center manifolds and especially NHIMs are neither analytically nor numerically easily obtained due to the few conditions they have to fulfill. They are usually approximated algebraically by power series, see, e.g., references [41–43].

2.5.3 Arnold web

In contrast to the tori of 2D maps the tori of higher dimensional systems are not barriers to transport in the phase space. An important consequence of this is the so-called Arnold web [12, 33, 44], which is covered in this section.

A torus of a $2N$-dimensional map F is a N-dimensional manifold and thus has the codimension N. But, in order to be a barrier in phase space a manifold has to have codimension one. This is only true for regular tori in a 2D phase space. Consequently, the tori of a 4D map and all higher dimensional maps do not separate different chaotic regions of the mixed phase space. On top of that, all resonant tori, which are dense in the unperturbed system are replaced by regular regions surrounded by chaotic channels in the perturbed system. Thus, the chaotic regions are dense in the perturbed system and not separated by the remaining KAM tori. Hence, each chaotic orbit can access any region of phase space. Note that in a 2D phase space the chaotic regions are also dense, but separated from each other by the 1D tori. In 2D maps the perturbation has to be increased above a critical value in order to obtain global chaotic motion [45, 46].

The net-like structure of broken resonant tori by which the chaotic regions are interconnected is called Arnold web. The slow component of the diffusion of chaotic orbits along this web is called Arnold diffusion. The Arnold diffusion and Arnold web are discussed in more detail in frequency space in Section 2.6.2.

2.6 Trapping in 4D

The algebraic decay of the statistics of Poincaré recurrences $P(t)$ for generic 4D symplectic maps is subject to extensive studies, see Section 2.2. As for 2D maps the reason

for the power-law behavior of $P(t)$ is the trapping of chaotic orbits in sticky regions. However, the structures governing the trapping in 2D are not sufficient to explain the trapping in higher dimensions. The reason is that the stable and unstable manifolds forming partial barriers in 2D have dimension one and thus are not barriers in higher dimensional spaces. Additionally a hierarchical structure as for the 2D phase space is not theoretically granted since the Poincaré-Birkhoff theorem is not valid for higher dimensional maps, see Section 2.5.1.

Therefore, in the following sections two conjectures about the trapping mechanism in higher dimensional maps are presented. Firstly, the concept of generalized partial barriers devised by Wiggins [15] is outlined in Section 2.6.1. Secondly, the approach of frequency analysis to the trapping phenomena is highlighted in Section 2.6.2.

2.6.1 Generalized partial barriers (NHIM)

One approach to the trapping mechanism in higher dimensional maps is the attempt to generalize the concept of partial barriers. Once such structures are found the mechanism can be understand analogously to the 2D case. Wiggins recognized that structures affiliated with NHIMs can form higher dimensional broken separatrices independent of the dimension of the phase space [15]. The concept and limitations of these generalized partial barriers is discussed in this section. Moreover, higher dimensional analogues of broken separatrices are studied in references [47–49].

In Section 2.5.2 NHIMs C_{NHIM} are introduced as invariant manifolds of codimension two, which are attached to a fixed point that is elliptic apart from a 2D hyperbolic component. Therefore, stable and unstable manifolds $W^s(C_{\mathrm{NHIM}})$ and $W^u(C_{\mathrm{NHIM}})$ can be defined, containing all points that contract to or expand from the NHIM C_{NHIM}. These manifolds are of codimension one and are therefore barriers in phase space. In this sense a NHIM C_{NHIM} with $W^s(C_{\mathrm{NHIM}})$ and $W^u(C_{\mathrm{NHIM}})$ is the equivalent of a hyperbolic fixed point $\boldsymbol{x}_f$ with its stable and unstable manifolds $W^s(\boldsymbol{x}_f)$ and $W^u(\boldsymbol{x}_f)$ in the 2D phase space. But unlike there, the intersections of the stable and unstable manifolds do not result automatically in partial barriers. The intersection sets have to fulfill certain conditions [15]. However, checking these conditions is laborious. Nevertheless, some examples are presented by Wiggins and his approach is considered, e.g., in reference [49].

Wiggins also relates the transport resulting from these generalized partial barriers to Arnold diffusion. In terms of the NHIMs C_{NHIM}, the Arnold diffusion occurs roughly speaking *tangent* to $W^s(C_{\mathrm{NHIM}})$ and $W^u(C_{\mathrm{NHIM}})$, whereas the transport due to partial barriers occurs transverse to these manifolds. The transport due to the latter is believed to be dominant.

In conclusion, although a generalization of the 2D trapping mechanism in form of higher dimensional partial barriers is possible, the relevance of this mechanism in higher dimensions is not clear. One reason for this is that finding structures in a generic system, which fulfill the requirements for such partial barriers, is difficult.

2.6.2 Frequency analysis

Transport in higher dimensional phase spaces is often studied in frequency space, see, e.g., references [2, 4, 5, 16, 50, 51]. The conjectures about trapping motivated from such investigations are outlined in this section, mainly based on the work by Martens, Davis, and Ezra [2, 16]. In order to discuss these conjectures, the frequency space is briefly introduced here. A more detailed introduction follows in Section 3.2.

The aim of the frequency analysis is to numerically obtain the fundamental frequencies $\boldsymbol{\omega} \in \mathbb{T}^N$ for orbits started on certain N-dimensional torus. The vector $\boldsymbol{\omega}$ can then be checked for resonances and visualized in frequency space if $N \leq 3$. For a 4D map every torus appears as a point in the 2D frequency space and the set of all tori fills some 2D area densely. When the system is weakly perturbed this area is interrupted by empty bands, which lie around lines representing resonance conditions 2.7. This complies with the break-up of the resonant tori and tori close to them according to the KAM theorem. Hence, the bands are called resonance zones. The width of these zones increases with the strength of the perturbation, which corresponds to the break-up of KAM tori closest to the resonance, and is bigger for resonances of lower order, both as implied by Eq. (2.6). According to Sections 2.4.1 and 2.5.1 the broken tori are replaced partially by chaotic regions. This means the set of the resonance zones represents the Arnold web connecting the chaotic regions. It is possible to map chaotic orbits which are close to tori to the frequency space. For reasons of continuity these orbits mimic the dynamics of the tori close to them. Thus, for small time spans t frequencies $\boldsymbol{\omega}(t)$ can be assigned to such an orbit. The transport of a chaotic orbit can be examined by means of this time dependent frequency $\boldsymbol{\omega}(t)$. Consequently, Arnold diffusion manifests as the propagation of the frequency $\boldsymbol{\omega}(t)$ along the resonances. Also transport perpendicular to the resonances is possible, which allows for a chaotic orbit to propagate from one resonance zone to another when they overlap. This enables chaotic orbits to propagate along a resonance zone to an intersection of resonances, called resonance junction or rank-2 resonance, and continue from there along a different resonance zone. The propagation along the resonances turns out to be orders of magnitude slower than perpendicular to the resonances [50].

In Section 2.4.2 two kinds of partial barriers are distinguished, namely broken sepa-

ratrices and cantori. Martens, Davis, and Ezra attempt to generalize both in terms of the frequency space [2, 16]. According to the authors the broken separatrix structures are given by the boundaries of the rank-1 resonance zones. One reason for this correspondence is the dimension of such a resonance-zone boundary in phase space. The line of a rank-1 resonance in the 2D frequency space represents a 3D region in the 4D phase space, as the resonant tori, formerly located on this line, form a one parameter family of 2D tori. Consequently, a 2D resonance zone in frequency space represents a 4D chaotic region in phase space. Hence, the boundary of the resonance zone is a 3D surface. This surface is assumed to be a generalized broken separatrix, e.g., of the kind described in Section 2.6.1. The influence of such broken separatrices is observed by means of trapping of chaotic orbits in the vicinity of a resonance junction. Such a junction is a point at which two resonance conditions, and consequently infinitely many other, are satisfied. Such a point represents a periodic orbit in phase space. It is conjectured that the propagation along one resonance zone is blocked by the broken separatrices of the other resonance zones intersecting at the junction [2]. This union of separatrices leads to the trapping at the junction. It seems to be left to chance on which resonance zone an orbit continues after the trapping [50]. In this context, it is observed that the transport rate along the Arnold web is determined by this trapping near resonance junctions rather than by the diffusion in between them [2]. Additionally, the Arnold diffusion is faster along resonances of lower order than of higher order. This rapid transport along low-order resonances is in accord with the so called resonance streaming, see [2] for futher references.

Besides the separatrix structures Martens, Davis, and Ezra also convey the cantori barriers into frequency space. They do so by noting that sometimes the transport across lines with one pairwise noble frequency ratio,

$$\frac{\omega_i}{\omega_j} = \text{noble number} \,, \tag{2.9}$$

appears to be inhibited. Noble numbers are highly irrational numbers [9]. In a 2D phase space KAM tori with such a frequency ratio to the external driving lead to cantori with strongly inhibited transport across them. In higher dimensions tori fulfilling a pairwise condition are thought to be the generalization of such irrational KAM tori. In this sense, a line with one pairwise noble frequency ratio represents a one parameter family of cantori in frequency space. Although, this is an object with a sufficient dimension to be a barrier, it is not always observed to be relevant for the transport along resonances [2, 16]. If such an object inhibits the transport across it, it will have holes with a more rapid transport [16, 51]. These holes are at intersections with resonances, where Eqs. (2.7)

and (2.9) are satisfied simultaneously.

Besides generalizations of broken separatrices and cantori, the complement of the Arnold web may explain the trapping. This complement consists of the KAM tori, which break up only at very strong perturbations. For the 2D maps these are the KAM tori with noble numbers as frequency. An effective generalization of noble numbers for higher dimensions is presented by Kim and Ostlund [17]. Chaotic orbits may be trapped in the fractal looking structure of the complement of the Arnold web. Additionally, resonance zones can be locally narrowed by the complement of the Arnold web, which may inhibit the transport. This is denoted as pinching but not covered here [16].

2.7 Example system

The trapping mechanism in 4D systems is studied in the next chapters based on Sections 2.5 and 2.6. A typical model system used for the study of higher dimensional maps is the coupled standard map. In order to introduce it, first the 2D standard map is presented in Section 2.7.1 and serves as a reference for the 2D case. Then the 4D coupled standard map is presented in Section 2.7.2 as the model of concern.

2.7.1 Standard Map

In this section the well studied 2D standard map is introduced with the parameters used in this thesis. This map has a very generic phase space. Therefore, it is a good reference of a 2D system. It is needed for comparison with the 4D case.

The Hamiltonian $H_{2D}(p, q, t)$ of the kicked rotor is

$$H_{2D}(p, q, t) = T_{2D}(p) + \sum_{n \in \mathbb{Z}} \delta(t - n) V_{2D}(q), \qquad T_{2D}(p) = \frac{p^2}{2},$$
$$V_{2D}(q) = \frac{K}{4\pi^2} \cos(2\pi q) \tag{2.10}$$

with the kinetic energy T_{2D}, the potential V_{2D}, and the kicking strength K. As the Hamiltonian $H_{2D}(p, q, t)$ has a time periodic driving for resonances applies Eq. (2.7). The domains of the momentum p and position q are $p \in [-0.5, 0.5)$ and $q \in [0, 1)$ with
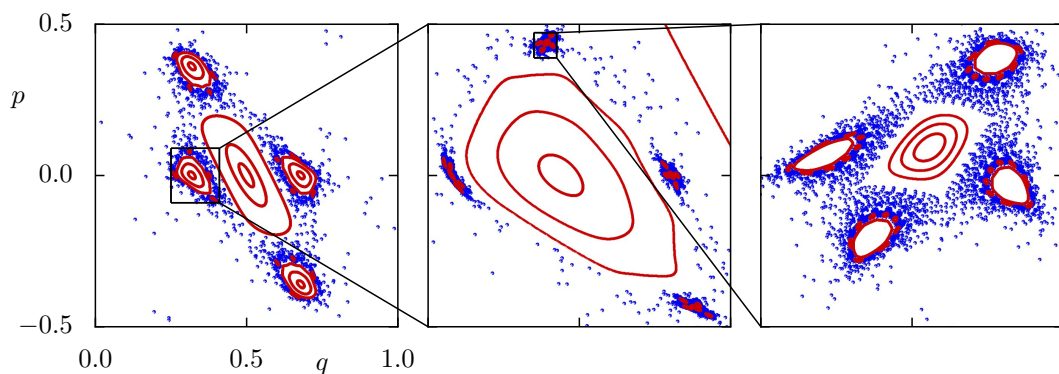
Figure 2.1: Hierarchical phase space of the 2D map F_{2D} for K=2.5. Some regular orbits (red points) and a trapped orbit (blue points) with length $T \approx 50 \cdot 10^3$ are shown. The zoom boxes show smaller regular islands forming a hierarchical structure in which the chaotic orbit is trapped.

periodic boundaries. From the Hamiltonian $H_{2D}(p, q, t)$ follows the symplectic map F_{2D}

$$(p', q') = F_{2D}(p, q) , \tag{2.11}$$
$$p' = p + \frac{K}{2\pi} \sin(2\pi q') ,$$
$$q' = q + p ,$$

solving the equation of motion emerging from Eq. (2.10) over one period of the driving. The kicking strength is chosen $K = 2.5$.

The phase space of F_{2D} is shown in Figure 2.1 on different scales with regular orbits in red and a trapped, chaotic orbit in blue. On the largest scale the central elliptic fixed point with its regular island is visible. This island is surrounded by four further regular islands. In their center are elliptic periodic points of period four. These periodic points indicate a chain of four elliptic and four hyperbolic periodic points. The hyperbolic points are in between the elliptic points and are not shown in the picture. This island-around-island structure is seen again on smaller scale in the magnifications of the middle and right picture. The chaotic orbit is trapped within this hierarchical structure.

2.7.2 Coupled Standard Map

In this section the 4D standard map, devised by Froeschlé [52], is introduced together with the parameters used in this thesis. In the literature 4D maps are mainly studied for weakly coupling [4, 44, 46, 53, 54]. The focus in this thesis, however, is on a strong coupling. This map is the model of concern throughout the following sections. Finally, some first aspects of the 4D phase space of the map are discussed.

The Hamiltonian $H_N(\boldsymbol{p}, \boldsymbol{q}, t)$ of N coupled, kicked rotors is

$$H_N(\boldsymbol{p}, \boldsymbol{q}, t) = T_N(\boldsymbol{p}) + \sum_{n \in \mathbb{Z}} \delta(t - n) V_N(\boldsymbol{q}) , \qquad\qquad T_N(\boldsymbol{p}) = \sum_{i=1}^{N} \frac{p_i^2}{2} ,$$

$$V_N(\boldsymbol{q}) = \sum_{i=1}^{N} \frac{K_i}{4\pi^2} \cos(2\pi q_i) + \frac{\xi}{4\pi 2} \cos\left(2\pi \left(\sum_{i=1}^{N} q_i\right)\right)$$

$$(2.12)$$

with kinetic energy T_N, potential V_N, kicking strengths K_i and coupling parameter ξ. The domains of the momentum $\boldsymbol{p}$ and position $\boldsymbol{q}$ are $\boldsymbol{p} \in [-0.5, 0.5)^N$ and $\boldsymbol{q} \in [0, 1)^N$ with periodic boundaries. From the Hamiltonian $H_N(\boldsymbol{p}, \boldsymbol{q}, t)$, follows for $N = 2$ the symplectic map F_{4D}

$$(\boldsymbol{p}', \boldsymbol{q}') = F_{4D}(\boldsymbol{p}, \boldsymbol{q}) , \qquad\qquad\qquad\qquad\qquad\qquad (2.13)$$

$$p_1' = p_1 + \frac{K_1}{2\pi} \sin(2\pi q_1') + \frac{\xi}{2\pi} \sin\left(2\pi \left(q_1' + q_2'\right)\right) ,$$

$$p_2' = p_2 + \frac{K_2}{2\pi} \sin(2\pi q_2') + \frac{\xi}{2\pi} \sin\left(2\pi \left(q_1' + q_2'\right)\right) ,$$

$$q_1' = q_1 + p_1 ,$$

$$q_2' = q_2 + p_2 ,$$

where the kicking strengths are set to $K_1 = 2.25$ and $K_2 = 3.0$. By the choice of the coupling parameter ξ a weakly coupled 4D map F_{WC} with $\xi = 0.1$ and a strongly coupled map F_{SC} with $\xi = 1$ are defined. Note that in the literature the coupling parameter is usually chosen to be very small $\xi < 10^{-2}$ [2, 4, 10, 46]. In contrast to this also strongly coupled systems are very interesting and relevant objects of investigations [55]. Therefore, the present work focuses on the strongly coupled map F_{SC}. For comparison the weakly coupled system F_{WC} can be found in appendix A.2.

Since the phase space of F_{SC} is due to the strong coupling more perturbed than the phase space of F_{2D}, the regular tori of F_{SC} are confined to a much smaller region. F_{SC} has an elliptic–elliptic fixed point $\boldsymbol{x}_f$ at the center $\boldsymbol{x}_f = (0, 0, 0.5, 0.5)$. The linearization of the map at $\boldsymbol{x}_f$ is given by the Jacobian $DF_{SC}(\boldsymbol{x}_f)$

$$DF_{SC}(\boldsymbol{x}_f) = \left(\frac{\partial(F_{SC}(\boldsymbol{x}_f) \cdot \boldsymbol{e}_j)}{\partial x_i}\right)_{ij} = \begin{pmatrix} 1 + B_1 + C & C & B_1 + C & C \\ C & 1 + B_2 + C & C & B_2 + C \\ 1 & 0 & 1 & 0 \\ 0 & 1 & 0 & 1 \end{pmatrix}$$

with $B_i = K_i \cos(2\pi(p_i + q_i))$ and $C = \xi \cos(2\pi(p_1 + p_2 + q_1 + q_2))$. The eigenvalues

$\{\lambda_i\}_{i=1...4}$ of the Jacobian $DF_{\mathrm{SC}}(\boldsymbol{x}_f)$ at an elliptic–elliptic fixed point $\boldsymbol{x}_f$ can be written as $\{\lambda_i\}_{i=1...4} = \{\mathrm{e}^{\mathrm{i}\omega_1}, \mathrm{e}^{-\mathrm{i}\omega_1}, \mathrm{e}^{\mathrm{i}\omega_2}, \mathrm{e}^{-\mathrm{i}\omega_2}\}$. The frequencies are $\omega_1/(2\pi) \approx 0.30632$ and $\omega_2/(2\pi) \approx 0.12173$. Each eigenvalue has a corresponding 2D eigenvectorspace tangential to a 2D center manifold, see Section 2.5.2.

In discussions about the phase space the notation $\boldsymbol{e}_{p_j}$ and $\boldsymbol{e}_{q_j}$ or $\boldsymbol{e}_i$ is used for the normalized base vectors of the momentum and position coordinates. The center of the phase space $(0.5, 0.5, 0, 0)$ is used as point of origin.

3 Representations of the 4D phase space

The 4D phase space of the coupled standard maps F_{WC} and F_{SC} introduced in Section 2.7.2 cannot be visualized directly like the 2D phase space of the standard map F_{2D} introduced in Section 2.7.1. Instead, lower dimensional representations of the phase space have to be used for investigations of F_{WC} and F_{SC}. These representations are listed in this chapter. First visualization methods for higher dimensional phase spaces are presented in Section 3.1. Secondly, in Section 3.2 the frequency space is explained and some issues of frequency analysis are discussed. As an application of the introduced representations, the tori structure of F_{SC} is examined in the phase and the frequency space in Section 3.3.

3.1 Visualization methods of the 4D phase space

Since phenomena occurring in 2D symplectic maps, such as trapping, are studied mainly in phase space, it is useful also for 4D symplectic maps to visualize their 4D phase space. This enables a direct comparison of the structures in 4D phase space with the known structures in the 2D case. Therefore in this section different methods are introduced, which attempt to visualize the 4D phase space. A regular orbit of the strongly coupled 4D map F_{SC} serves as an example for the different methods.

3.1.1 2D Projections

Since a 2D phase space is given by the momentum–position plane (p, q), a 4D phase space can be visualized by two momentum–position planes, (p_1, q_1) and (p_2, q_2). Thus, orbits in the 4D phase space are projected onto planes. Instead of the planes (p_1, q_1) and (p_2, q_2) any other skew planes can be used. Also a different number of planes, e.g., the three planes (p_1, q_2), (p_2, q_1), and (p_1, p_2) can be considered simultaneously.

This method of 2D projections allows for a direct comparison with 2D phase spaces, especially for weakly coupled maps such as F_{WC}. In this case the 2D projections of the
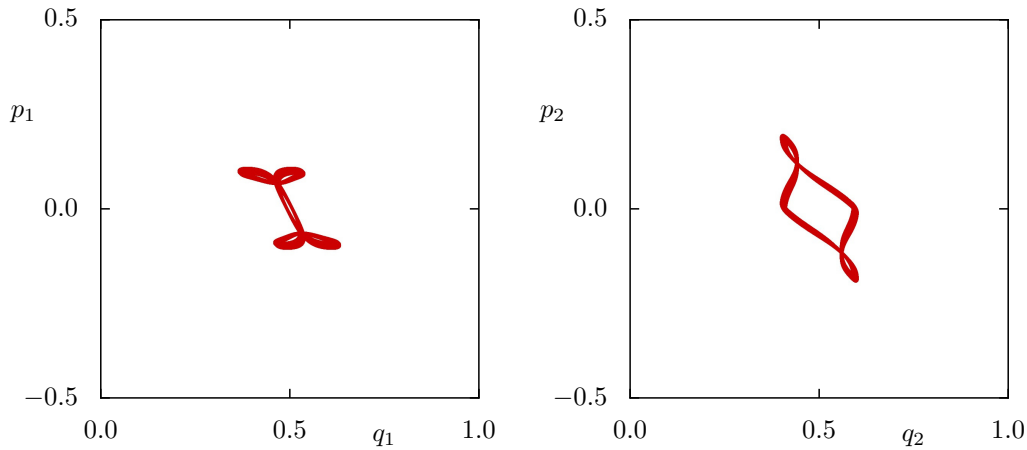
Figure 3.1: 2D projections of a regular orbit (red) with length $T = 10^5$ of the strongly coupled 4D map F_{SC}, see Eq. (2.13).

map without coupling can be compared to the projections of the map with different coupling parameters. However, for orbits of a strongly coupled map the 2D projections are hard to interpret. This is demonstrated by the example in Figure 3.1, where the regular torus looks like it intersects itself. Nevertheless, 2D projections of orbits are used for the analysis of fundamental frequencies as introduced in Section 3.2.

3.1.2 Method of color and rotation

Since the 3D space is comprehensible, it can be employed for visualizing the 4D phase space. However, on a 2D screen a 3D space is only understandable by *rotation*, which reveals the spatial relations regarding the missing dimension.

In order to visualize the 4D phase space with the available 3D space, every point of the 4D phase space is projected to the 3D space of three coordinates and colored corresponding to the remaining coordinate, see, e.g., reference [56]. As an example, Figure 3.2 shows the regular orbit from Figure 3.1 projected to the coordinates (p_1, q_1, q_2) using a red to blue colormap for p_2. This color map is used throughout the thesis for the method of color and rotation.

In the method of color and rotation objects are depicted with all their spatial relations. This is advantageous for objects with a dimension $D \leq 3$, e.g., 2D tori, as seen in Figure 3.2, because such objects are depicted with their real dimensionality, and thus their principle structure is visible. Therefore this method is particularly useful, when visualizing a few number of tori. However, visualizations of several orbits or even orbits filling or covering a 4D object can look irritating. For such cases the method of sections and rotation presented in Section 3.1.3 is preferred.
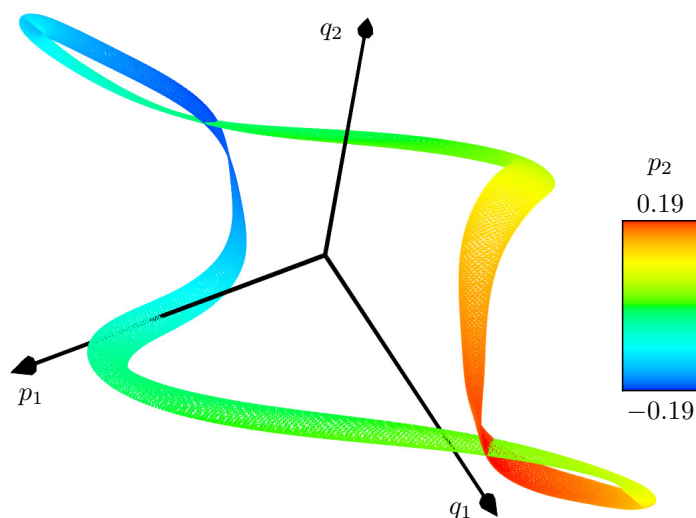
Figure 3.2: 3D projection of a regular orbit with length $T = 10^5$, same as in Figure 3.1, according to the method of color and rotation. The orbit is projected to the coordinates (p_1, q_1, q_2) using a red to blue colormap for p_2 as indicated by the colorbar.

3.1.3 Method of phase-space sections

The 4D phase space can also be visualized in the 3D space by depicting a thin 3D section of it. Such a section $s_{\boldsymbol{n}, D, \epsilon}$ of the phase space $U \subset \mathbb{R}^4$ is defined, e.g., by the normal form of a planar equation

$$s_{\boldsymbol{n}, D, \epsilon} \equiv \left\{ \boldsymbol{x} \in U \colon |\boldsymbol{x} \cdot \boldsymbol{n} - D| < \epsilon \right\}, \tag{3.1}$$

with the parameters $D \in \mathbb{R}$, a normalized vector $\boldsymbol{n} \in R^4$, and $1 \gg \epsilon > 0$. Only points, which are elements of $s_{\boldsymbol{n}, D, \epsilon}$, are depicted in the 3D space according to the orthonormal coordinates $\{\boldsymbol{e}_i\}_{i=1,2,3}$, for which $\boldsymbol{e}_i \cdot \boldsymbol{e}_j = \delta_{ij}$ and $\boldsymbol{e}_i \cdot \boldsymbol{n} = 0$. Therefore, for an orbit of length T typically only $\sim T \cdot \epsilon$ points are visible in the section.

Depictions for several sections with different parameters $\boldsymbol{n}$, D, ϵ give an idea of the 4D phase space. In this thesis the parameters of Eq. (3.1) are chosen as $\boldsymbol{n} = \boldsymbol{e}_{p_2}$, $D = 0$, and $\epsilon \in [10^{-4}, 10^{-5}]$, such that points are elements of the section when their p_2 coordinate fulfills $|p_2| < \epsilon$. In the following this set of parameters is abbreviated with $|p_2| < \epsilon$. Points of regular and chaotic orbits are shown as red and blue points, respectively and for regular orbits usually 4000 points within the section are shown, see, e.g., Figures 3.3 and 3.4(a). Such a depiction of the phase space in form of a section is referred to as *phase-space section* [10, 52, 57, 58].

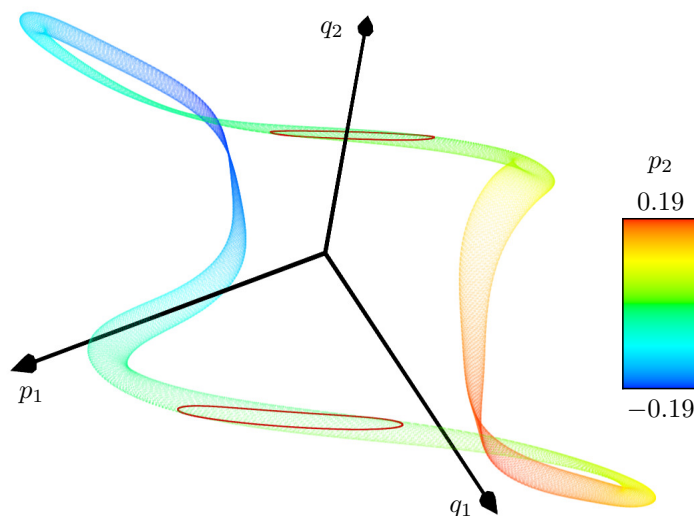Note that phase-space sections can deceive about the real dimensionality and connec-

Figure 3.3: Visualization of a regular orbit (red ellipses), same as in Figure 3.1, in form of a phase-space section. The section parameters are $\boldsymbol{n} = \boldsymbol{e}_{p_2}$, $D = 0$, and $\epsilon = 10^{-5}$, abbreviated by $|p_2| < 10^{-5}$. The orbit is iterated until 4000 points are in the section. For comparision the projection of the same orbit as in Figure 3.2 is shown with a reduced opacity.

tion of objects. E.g., in Figure 3.3 a 2D torus appears as two separated ellipses. These two separated objects occur because the torus intersects the section twice. Depending on the orbit even more intersections and therefore more separated objects belonging to the same orbit are possible.

The 1D ellipses resulting from the 2D torus in Figure 3.3 illustrate the fact that objects of the 4D phase space appear in the phase-space section with a dimension reduced by one. Hence, compared to the method of color and rotation, see Section 3.1.2, the method of section and rotation has the advantage, that 4D objects are depicted as 3D objects, such that they become comprehensible. For instance a family of tori appears as a family of ellipses, forming a 3D island, see Figure 3.4(a).

In Figure 3.4 a phase-space section for the weakly coupled 4D map F_{WC} is shown with regular orbits and a chaotic orbit, compared to the phase space of the 2D map F_{2D} with $K = 2.25$. Since, according to Eqs. (2.11) and (2.13), the 4D map F_{WC} corresponds to two standard maps with parameters K_1 and K_2, that are *weakly* coupled, the depicted phase-space section looks similar to the phase space of the standard map F_{2D} with a parameter $K = K_1$.

Additionally in some figures a chaotic orbit $\boldsymbol{x}(t)$ is not just colored blue but rather every point of the orbit has a color representing its time t. This is referred to as *orbit colored by time t* and the same color map used for the method in Section 3.1.2 is employed for this, see for example Figure 5.5(b).
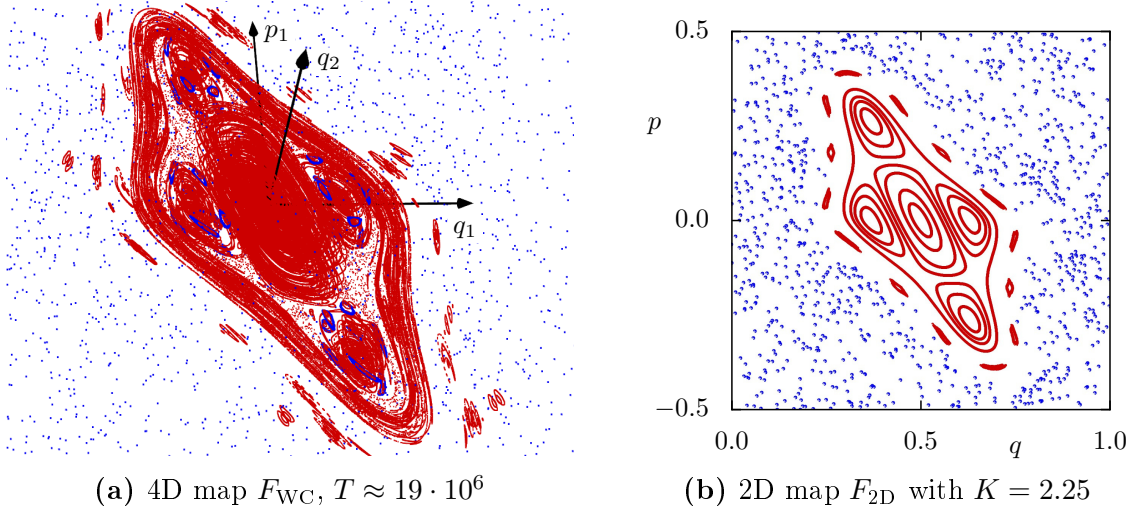
(a) 4D map F_{WC}, $T \approx 19 \cdot 10^6$ **(b)** 2D map F_{2D} with $K = 2.25$

Figure 3.4: Example for a phase-space section for (a) the 4D map F_{WC}, see Eq. (2.13). Shown is the section $|p_2| < \epsilon$, with regular tori (red, $\epsilon = 10^{-5}$) and an example of a trapped orbit (blue, $\epsilon = 10^{-4}$). For comparison the phase space of the 2D map F_{2D} with $K = 2.25$, see Eq. (2.11) is shown in (b), with regular tori (red) and a chaotic orbit (blue). The captions contain the corresponding map and for (a) the length T of the trapped orbit.

3.2 Frequency space

Instead of depicting the original 4D phase space, it is sometimes advantageous to examine the dynamics in the 2D frequency space, because this space requires only half of the dimensions. Also the transport in a higher dimensional phase space is often studied by means of this frequency analysis, see Section 2.6.2. While Section 2.6.2 only gives a brief discussion of the known dynamics in frequency space the frequency analysis is introduced in more detail here. The calculation of the fundamental frequencies $\boldsymbol{\omega}$ as suggested by Laskar [14, 59, 60] is explained in Section 3.2.1. The issues of this method which are especially encountered for the strongly disturbed map F_{SC} are discussed in Section 3.2.2 and solutions are suggested. The parameters of the numerical analysis of fundamental frequencies which are motivated by this discussion are presented in Section 3.2.3.

3.2.1 Analysis of fundamental frequencies

The term frequency analysis refers to the fundamental frequencies $\boldsymbol{\omega}$ of a torus of a symplectic map F. One way to obtain the frequencies $\boldsymbol{\omega}$ is by Laskar's numerical analysis of fundamental frequencies [14, 59, 60], which is outlined here for N degrees of freedom.

Generally, Laskar's frequency analysis seeks to approximate a function $\boldsymbol{z}\colon [0,T] \to \mathbb{C}^N$, by a quasiperiodic function $\tilde{\boldsymbol{z}}(t)$. For example choosing $\boldsymbol{z}(t)$ to be the N-dimensional vector

$$\boldsymbol{z}(t) \equiv \boldsymbol{q}(t) - \mathrm{i}\boldsymbol{p}(t)\,, \tag{3.2}$$

with momentum and position $\boldsymbol{p}$, $\boldsymbol{q} \in \mathbb{R}^N$, this means for the components of $\tilde{\boldsymbol{z}}(t)$

$$\tilde{z}_i(t) = \sum_{m=1}^{M} \mathrm{e}^{\mathrm{i}\tilde{\omega}_{i,m}t} \tilde{a}_{i,m} + \frac{1}{T} \int_0^T \mathrm{d}t\, z_i(t) \tag{3.3}$$

with frequencies $\tilde{\omega}_{i,m} \in \mathbb{T}$ and complex amplitudes $\tilde{a}_{i,m} \in \mathbb{C}$. The average value of $\boldsymbol{z}(t)$, represented by the second term in Eq. (3.3), can be subtracted from $\boldsymbol{z}(t)$ beforehand and is therefore neglected in the following. In order to determine the parameters $\tilde{\omega}_{i,m}$ and $\tilde{a}_{i,m}$, the original function $\boldsymbol{z}(t)$ is projected onto elements of the base $\{\mathrm{e}^{\mathrm{i}\tilde{\omega}t}\}_{\tilde{\omega} \in \mathbb{T}}$ via a scalar product

$$\phi_i(\tilde{\omega}) \equiv \langle \mathrm{e}^{\mathrm{i}\tilde{\omega}t} | z_i(t) \rangle_\chi \,, \tag{3.4}$$

which is defined as

$$\langle f(t)|g(t)\rangle_\chi = \frac{1}{T} \int_0^T \mathrm{d}t\, \bar{f}(t)g(t)\chi(t)\,, \tag{3.5}$$

where the limits of the integral are given by the domain of $\boldsymbol{z}(t)$. The window function $\chi(t)$ is a positive weight function, which is normalized with respect to the limits of the integral

$$\frac{1}{T} \int_0^T \mathrm{d}t\, \chi(t) = 1\,.$$

The window function $\chi(t)$ is such that the considered product $\boldsymbol{z}(t)\chi(t)$ is a quasiperiodic function. As in references [14, 59, 60] the Hanning window filter is used here defined as

$$\chi(t) = (1 - \cos(2\pi t/T))\,.$$

This increases the accuracy of the discrete Fourier transformation which is performed in the following.

Laskar suggests to identify the first frequencies $\tilde{\omega}_{i,1}$ with the frequencies $\tilde{\omega}_i^{\max}$ at which the absolute value of the overlap $\phi_i(\tilde{\omega})$ is maximal,

$$|\phi_i(\tilde{\omega}_i^{\max})| = \max_{\tilde{\omega} \in \mathbb{T}} |\phi_i(\tilde{\omega})| = \max_{\tilde{\omega} \in \mathbb{T}} |\langle e^{i\tilde{\omega}t} | z_i(t) \rangle_\chi| \qquad (3.6)$$

which leads to

$$\tilde{\omega}_{i,1} = \tilde{\omega}_i^{\max}$$
$$\tilde{a}_{i,1} = \phi_i(\tilde{\omega}_i^{\max}).$$

This corresponds to an orthogonal projection of $\boldsymbol{z}(t)$ to the base vectors $\{e^{i\tilde{\omega}_{i,1}t}\}_{i=1...N}$. This algorithm can be applied again to the remaining function $z_i^{(1)}(t)$

$$z_i^{(1)}(t) \equiv z_i(t) - e^{i\tilde{\omega}_{i,1}t}\tilde{a}_{i,m}. \qquad (3.7)$$

The resulting exponential functions $\{e^{i\tilde{\omega}t}\}_{\tilde{\omega} \in \mathbb{T}}$ are not orthonormal to each other with respect to the scalar product of Eq. (3.4). Therefore, for every component i the newly obtained exponential function $e^{i\tilde{\omega}_{i,2}t}$ has to be orthonormalized with respect to the first one $e^{i\tilde{\omega}_{i,1}t}$. Iterations of this process determine successively higher orders of Eq. (3.3).

In particular, this algorithm can compute the fundamental frequencies $\boldsymbol{\omega}$ of regular tori. Laskar suggests that a component of the frequency vector ω_i is the dominant frequency $\tilde{\omega}_{i,1}$ of the corresponding projection $z_i(t)$, see Eqs. (3.2) and (3.3). Laskar mentions two restrictions to the algorithm: the method should give accurate frequencies for rapidly decreasing amplitudes $\tilde{a}_{i,m}$ [14] and for systems not so far from integrability [60]. Furthermore, the algorithm can be applied to some chaotic orbits for a certain time span. Opposed to the frequencies of a regular torus, the obtained frequencies $\boldsymbol{\omega}(t)$ will not be constant but time dependent.

3.2.2 Problems of Laskar's method

The frequency analysis is based on projections of phase-space vectors. This causes problems for strongly perturbed maps such as F_{SC}, see Section 2.7.2. Since such maps are seldom studied, these issues are not discussed in the literature. The problems are presented here along with suggestions for their solution.

In the following the complex vector $\boldsymbol{z}(t)$ of a regular orbit $\boldsymbol{x}(t)$ is considered according to Eq. (3.2). First of all the numerically obtained frequencies $\tilde{\boldsymbol{\omega}}$ are compared to the fundamental frequencies $\boldsymbol{\omega}$ of the orbit $\boldsymbol{x}(t)$. The problems of Laskar's algorithm are discussed on the basis of this comparison.

According to Section 3.2.1 the frequencies $\tilde{\boldsymbol{\omega}}$ are obtained separately from every component of $\boldsymbol{z}(t)$. The components of $\boldsymbol{z}(t)$ correspond to projections of the dynamics to each degree of freedom $(p_i, q_i)_{i=1\ldots N}$. Note that the following arguments are also valid for other projections, e.g., for the single components $p_1(t)$, $p_2(t)$, $q_1(t)$, $q_2(t)$ of the orbit $\boldsymbol{x}(t)$.

According to Section 2.3 every regular orbit $\boldsymbol{x}(t) = (\boldsymbol{p}(t), \boldsymbol{q}(t))$ can be expressed by the action–angle coordinates $\boldsymbol{x}(t) = \boldsymbol{x}(\boldsymbol{I}(t), \boldsymbol{\Theta}(t))$ of the corresponding torus. For perturbed systems these are the action–angle coordinates of a KAM torus. Since the action coordinates are constant on a torus, they are neglected in the following and the complex $\boldsymbol{z}(t)$ can be given by a Fourier series of the angles $\boldsymbol{\Theta}$

$$
\begin{aligned}
\boldsymbol{z}(\boldsymbol{\Theta}(t)) &= \boldsymbol{q}(\boldsymbol{\Theta}(t)) - \mathrm{i}\boldsymbol{p}(\boldsymbol{\Theta}(t)) \\
&= \sum_{\boldsymbol{m} \in \mathbb{Z}^N} \mathrm{e}^{\mathrm{i}\boldsymbol{m}\cdot\boldsymbol{\Theta}(t)} \boldsymbol{a_m}
\end{aligned} \tag{3.8}
$$

with complex amplitudes $\boldsymbol{a_m} \in \mathbb{C}^N$. E.g., for $N = 2$ the amplitudes $\boldsymbol{a_m}$ are given by

$$
\boldsymbol{a_m} = \left(\frac{1}{2\pi}\right)^2 \int\limits_0^{2\pi}\int\limits_0^{2\pi} \mathrm{d}\Theta_1 \, \mathrm{d}\Theta_2 \, \mathrm{e}^{-\mathrm{i}\boldsymbol{m}\cdot\boldsymbol{\Theta}} \boldsymbol{z}(\boldsymbol{\Theta}) \qquad \forall \, \boldsymbol{m} \in \mathbb{Z}^2 \, .
$$

Substituting in Eq. (3.8) the dynamics of the angles $\boldsymbol{\Theta}(t)$ given by Eq. (2.4)

$$
\boldsymbol{\Theta}(t) = (\boldsymbol{\Theta}_0 + \boldsymbol{\omega} t) \mod 2\pi
$$

with the fundamental frequencies $\boldsymbol{\omega}$ of the torus, it is obtained [61]

$$
\boldsymbol{z}(t) = \sum_{\boldsymbol{m} \in \mathbb{Z}^N} \mathrm{e}^{\mathrm{i}\boldsymbol{m}\cdot\boldsymbol{\omega} t} \boldsymbol{a_m} \tag{3.9}
$$

by redefining the amplitudes

$$
\boldsymbol{a_m}\mathrm{e}^{\mathrm{i}\boldsymbol{m}\cdot\boldsymbol{\Theta}_0} \to \boldsymbol{a_m} \, .
$$

Eq. (3.9) relates $\boldsymbol{z}(t)$ to the fundamental frequencies $\boldsymbol{\omega}$ of the regular torus. The frequencies ω_i appear in the exponents of the terms with $\boldsymbol{m} = \boldsymbol{e}_i$. All other frequencies $\boldsymbol{m}\cdot\boldsymbol{\omega}$ with $\boldsymbol{m} \neq \boldsymbol{e}_i$ are harmonics of $\boldsymbol{\omega}$. The amplitudes $\boldsymbol{a_m}$ in Eq. (3.9) result roughly speaking from the arrangement of the invariant torus in phase space, in contrast to $\boldsymbol{\omega}$, which describes the dynamics on the torus. In general, the amplitudes $\boldsymbol{a_m}$ of the harmonics $\boldsymbol{m}\cdot\boldsymbol{\omega}$ are not zero. This is a consequence of the projection to the components

of $\boldsymbol{z}(t)$.

Note that the components of $\boldsymbol{z}(t)$ in Eq. (3.9) have already the quasiperiodic form of Eq. (3.3). In contrast to Eq. (3.3) the different components of $\boldsymbol{z}(t)$ contain all the same information about the dynamics in terms of the frequency vector $\boldsymbol{\omega}$ and differ only in their amplitudes.

In order to obtain $\boldsymbol{\omega}$ from $\boldsymbol{z}(t)$ by means of Laskar's frequency analysis, the maxima of the functions $|\phi_i(\tilde{\omega})|$ defined in Eq. (3.4) have to be evaluated. Considering Eq. (3.9) as a representation of the product $\boldsymbol{z}(t)\chi(t)$, it follows for $\boldsymbol{\phi}(\tilde{\omega})$

$$
\begin{aligned}
\boldsymbol{\phi}(\tilde{\omega}) &\equiv \langle \mathrm{e}^{\mathrm{i}\tilde{\omega}t} | \boldsymbol{z}(t) \rangle_\chi \\
&= \frac{1}{T} \int_0^T \mathrm{d}t\, \mathrm{e}^{-\mathrm{i}\tilde{\omega}t} \boldsymbol{z}(t)\chi(t) \\
&= \sum_{\boldsymbol{m}} \boldsymbol{a_m} \frac{1}{T} \int_0^T \mathrm{d}t\, \mathrm{e}^{\mathrm{i}(\boldsymbol{m}\cdot\boldsymbol{\omega}-\tilde{\omega})t} \\
&= \sum_{\boldsymbol{m}} \boldsymbol{a_m} \begin{cases} 1 & \text{for } \boldsymbol{m}\cdot\boldsymbol{\omega}-\tilde{\omega}=0 \mod 2\pi \\ \frac{\mathrm{e}^{\mathrm{i}(\boldsymbol{m}\cdot\boldsymbol{\omega}-\tilde{\omega})T}-1}{\mathrm{i}(\boldsymbol{m}\cdot\boldsymbol{\omega}-\tilde{\omega})T} & \text{else} \end{cases}
\end{aligned}
\tag{3.10}
$$

The T in (3.10) is the length of the orbit $\boldsymbol{x}(t)$ belonging to $\boldsymbol{z}(t)$. T is either chosen arbitrarily large or at least of the order $T \sim 10^3$. Consequently, $|\phi_i(\tilde{\omega})|$ is suppressed by T, for all frequencies $\tilde{\omega}$ that do not satisfy

$$
\tilde{\omega} = (\boldsymbol{m}\cdot\boldsymbol{\omega}) \mod 2\pi
\tag{3.11}
$$

for any $\boldsymbol{m} \in \mathbb{Z}^N$. All frequencies, which fulfill Eq. (3.11), can form a maximum of $|\phi_i(\tilde{\omega})|$. Only the amplitudes $\boldsymbol{a_m}$ distinguish between these frequencies, that is the dominant frequency depends on the geometry of the torus in phase space.

For weakly coupled maps the $\boldsymbol{a_m}$ are usually such that the dominant frequency of $z_i(t)$ is indeed the fundamental frequency ω_i for all components i. However, for strongly perturbed maps the tori are very deformed. For F_{SC} the numerically obtained frequencies $\tilde{\boldsymbol{\omega}} = (\omega_1, \omega_2)$ of many regular orbits lie on resonances such as $1 : -1 : 0$, $1 : 1 : 1$ or $m : 1 : n$, although resonances are not possible for regular tori in a perturbed system, see Section 2.3. Therefore, the resonant frequencies $\tilde{\boldsymbol{\omega}}$ are not the fundamental frequencies $\boldsymbol{\omega} = (\omega_1, \omega_2)$, but numerical artifacts resulting from Eq. (3.11). For instance, the resonance $1 : -1 : 0$ means that both components of $\boldsymbol{z}(t)$ have the same maximum, e.g., at the first fundamental frequency $\tilde{\omega}_1 = \omega_1$ and $\tilde{\omega}_2 = \omega_1$. Likewise, the resonance $1 : 1 : 1$ means that the frequencies $\tilde{\boldsymbol{\omega}}$ have the same absolute value but a different

sign, e.g., $\tilde{\omega}_1 = \omega_1$ and $\tilde{\omega}_2 = -\omega_1$. Finally, the resonance $m : 1 : n$ suggests a scenario like $\tilde{\omega}_1 = \omega_1$ and $\tilde{\omega}_2 = m\omega_1$ with $m \in \mathbb{Z}$. In reference [2] the ambiguity resulting from Eq. (3.11) is acknowledged by defining an ambiguity index by which the quality of the obtained results is estimated.

However, usually one of the frequencies $\boldsymbol{\omega}$ is obtained correctly. This is the dominant frequency ω_1, whose corresponding angle Θ_1 has the bigger spatial relevance for the torus and therefore bigger affiliated amplitudes in Eq. (3.9). Based on this, the ambiguity for the second frequency ω_2 due to Eq. (3.11) might be solved by considering N_ω orders of frequencies for every component of $\boldsymbol{z}(t)$ according to Eq. (3.7). Within the resulting set of $N \cdot N_\omega$ frequencies several numerically obtained values $\tilde{\omega}$ appear more than once as frequencies might be present in more than just one component according to Eq. (3.9). If the $N \cdot N_\omega$ frequencies are reduced to a unique subset, then this subset can be searched for a nonresonant pair, whose linear combinations give the remaining frequencies of the set in the sense of Eq. (3.11). The importance of the frequencies in terms of the magnitude of the maximum in Eq. (3.6) can be an additional guideline in the determination of the nonresonant pair of frequencies.

This search does not work always due to the limited accuracy of the frequencies. When the spatial relevance of the angle Θ_2 is too small, that is when the 2D torus looks like a thin tube, see e.g. Figure 3.2, it might be impossible to obtain ω_2 numerically.

When the deformation is so strong, that the torus is twisted, the dominant frequency ω_1 can be suppressed compared to its higher harmonics in Eq. (3.9). In this case the right frequency ω_1 might not be obtained in any component or order of $\boldsymbol{z}(t)$. It can only be assumed that the obtained dominant frequency $\tilde{\omega}$ is of the form

$$\tilde{\omega} = (m \cdot \omega_1) \mod 2\pi = m \cdot \omega_1 + 2\pi n \tag{3.12}$$

with $m, n \in \mathbb{Z}$. The parameter m might be guessed from depictions of the orbit $\boldsymbol{x}(t)$ in phase space by means of the methods presented in Sections 3.1.1 and 3.1.2. For instance, when a torus looks like it is twisted three times around the center of the phase space, the division of $\tilde{\omega}$ by three might result in the right frequency ω_1, see Onken [62].

Finally, tori which split up in disjoint parts have to be considered separately. Their dominant frequency describe the dynamics between their parts as it is the case for tori in the vicinity of elliptic–elliptic periodic points. Using only the points belonging to one part the dynamics within the parts can be examined.

In conclusion, not all problems of Laskar's frequency analysis can be solved in general. The main problem is that the frequency analysis is applied to 2D projections of the higher dimensional phase space, which is especially troublesome for strongly deformed

tori. Some information about the dynamics of a regular orbit $\boldsymbol{x}(t)$ is lost in these projections. Thus, it would be better to have a frequency analysis, which can be applied directly to the phase space vector $\boldsymbol{x}(t)$.

3.2.3 Numerical implementation

In this section the numerical setup for the frequency analysis is presented as it is used for the following investigations. The parameters necessary for Laskar's algorithm are introduced. This includes some pragmatic solutions for the problems discussed in Section 3.2.2.

For regular orbits 2^{12} points are used to form the signal $\boldsymbol{z}(t)$, see Eq. (3.2). Chaotic orbits are split into disjoint parts of $\triangle t = 2^{12}$ points and a frequency is calculated for each part, leading to time dependent frequencies $\boldsymbol{\omega}(t)$. For the maximum search, see Eq. (3.6), the method described in reference [63] is used. According to this work, the errors of the frequencies are expected to be less than 10^{-6} for the chosen time span $\triangle t$.

The conceptual issues presented in Section 3.2.2 are avoided in the majority of the cases by the following procedure. Firstly, the $z_1(t)$ component is considered. The dominant frequency ω_1 is determined and all harmonics up to order three, that is $|m| \leq 3$ in Eq. (3.12), are subsequently subtracted from $\boldsymbol{z}_1(t)$, see Eq. (3.7). Then the dominant frequency ω_2 of the modified $z_1(t)$ is determined. If ω_1 and ω_2 are too close to a resonance condition they are discarded and the procedure is run instead for the $z_2(t)$ component. This procedure is discussed in detail for an example in Section 3.3.

The signs of the frequencies are neglected by restricting the frequency space to $[0, \pi)$. All frequencies ω_i with $\omega_i > \pi$ are projected to the restricted frequency space by $\omega_i' = 2\pi - \omega_i$.

3.3 Example: regular tori in phase and frequency space

The method of sections and rotation, introduced in Section 3.1.3, and the frequency analysis, introduced in Section 3.2, are used to study the regular tori in the 4D phase space of the strongly coupled map F_{SC}. Some groups of regular tori are named for reference in the following sections. In this context, also the manual correction and interpretation of the results in frequency space are demonstrated.

In order to obtain regular orbits points on a grid in phase space are iterated and all points, which enter into a region with too high Lyapunov-Exponents [64], are removed.

This algorithm is adopted from Richter and more details can be found in his dissertation [58]. Note that the algorithm sometimes returns orbits, which are not regular but merely trapped for very long times. This is a problem that has not been solved yet, but for the purpose of this thesis a sufficient amount of the orbits seems to be regular. Here 1885 orbits, each with 4000 points in the section $|p_2| < 10^{-5}$, are used to represent the regular tori.

The frequencies of the regular orbits are calculated by projecting the orbits to the (p_1, q_1)-plane, as described in Section 3.2.3. In contrast here no harmonics are neglected, such that the manual correction of the frequencies can be demonstrated. The resulting picture of the regular tori in frequency space is shown in Figure 3.5(a). Every regular orbit appears as a point in frequency space. Some of these points lie on lines representing a certain resonance. According to Section 2.5.1, regular orbits with resonant frequencies are either periodic orbits or fixed lines. Due to their dimensionality it is unlikely that such orbits are found by a grid in phase space. Nevertheless, a lot of orbits in the frequency space of Figure 3.5(a) lie on resonances. Such resonant frequencies can occur as artifacts of the frequency analysis, as discussed in Section 3.2.2. Therefore the frequencies of the orbits, that lie on a resonance in Figure 3.5(a), are checked by calculating them again for the projection to a different plane, namely the (p_2, q_2)-plane. The newly obtained frequencies of the formerly resonant orbits are shown in Figure 3.5(b) highlighted with the same colors as in Figure 3.5(a). In addition, in Figure 3.5(a), all the frequencies that do not lie on a resonance are depicted as red points. These frequencies are assumed to be correct and therefore again shown in Figure 3.5(b).

In Figure 3.5(b), the majority of the non-red colored orbits are not on the resonance lines anymore. Usually they differ in one coordinate from their former position in Figure 3.5(a). For instance the blue points of the resonance $7 : -1 : 2$ appear with a bigger ω_2, such that they are in the vicinity of the red points in the zoom box. In phase space the orbits corresponding to the blue colored frequencies are all close to each other in phase space, as can be seen in Figure 3.9, where the same blue is used. Therefore, these orbits are expected to be close to each other also in frequency space. Consequently the blue colored frequencies, which are still on the resonance $7 : -1 : 2$ in Figure 3.5(b), are wrong. Their correct ω_2 should be such that these points are close to the frequencies in the zoom box in Figure 3.5(b), as are the other blue points.

Note that the corrected frequencies of the blue orbits are located at the edge of the structure indicated by the red points in the zoom box. In the phase-space section the ellipses representing these orbits have a smaller radius than the ellipses of the orbits of the red colored frequencies. In chapter 4, especially Section 4.2.3, this property is found to make the frequency analysis of these orbits problematic. Analog considerations, as
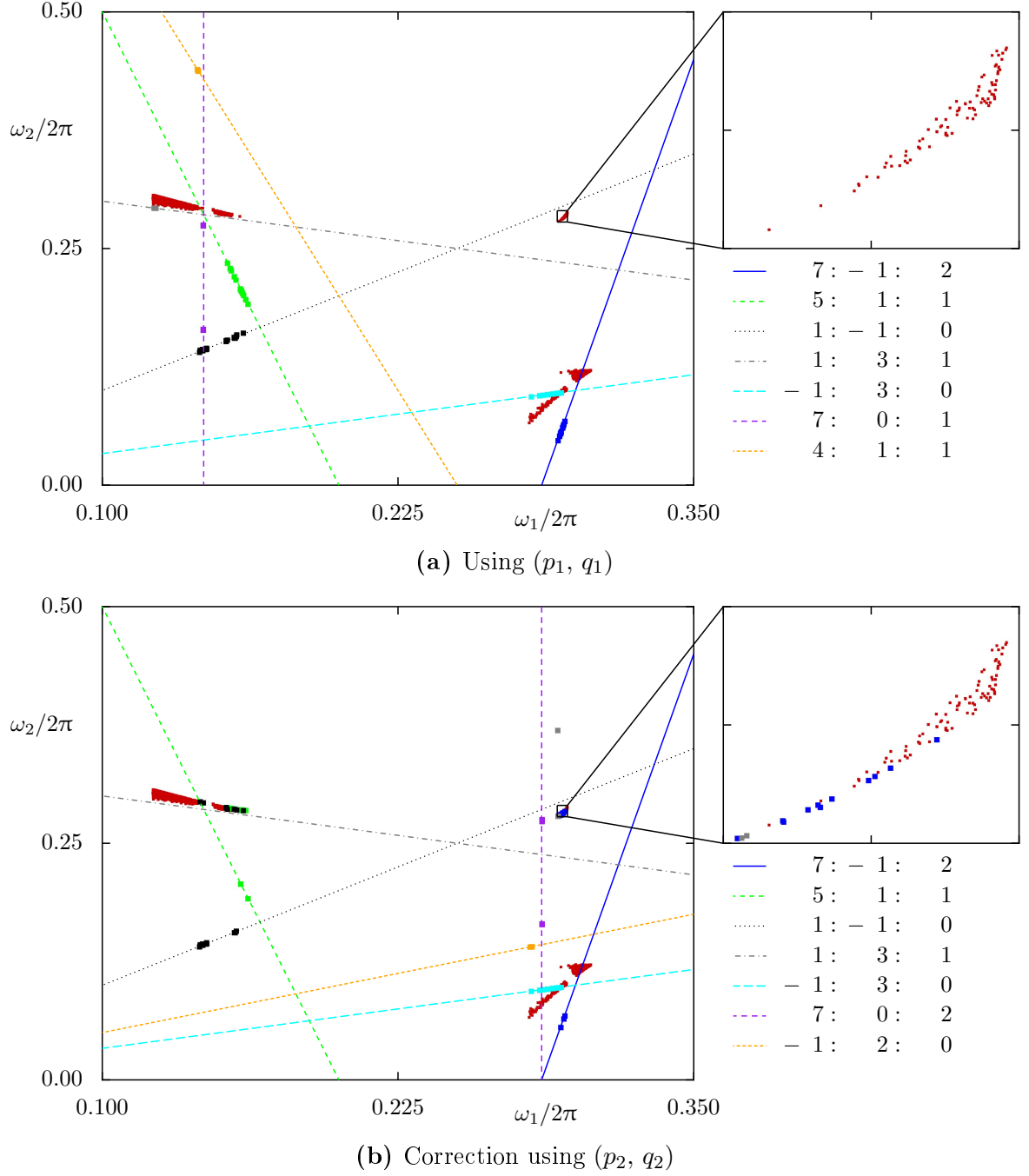
(a) Using (p_1, q_1)

(b) Correction using (p_2, q_2)

Figure 3.5: Manual correction of frequencies of regular tori of the 4D map F_{SC}, see Eq. (2.13). (a) Result for frequencies of the regular orbits (red points), when projecting to the (p_1, q_1) plane. Frequencies that lie on resonances are highlighted in different colors and the according resonance lines are inserted in the same color. The zoom box shows a magnification of a group of regular orbits. (b) Same as (a), except that for the regular orbits, which lie on resonances in (a) (all non-red points), the frequencies are obtained for the projection to the (p_2, q_2) plane. Note that here instead of the resonances $7 : 0 : 1$ and $4 : 1 : 1$, as in (a), the resonances $7 : 0 : 2$ and $-1 : 2 : 0$ are shown.

(a) ω_1 dominant frequency

(b) $\omega_1 > \omega_2$
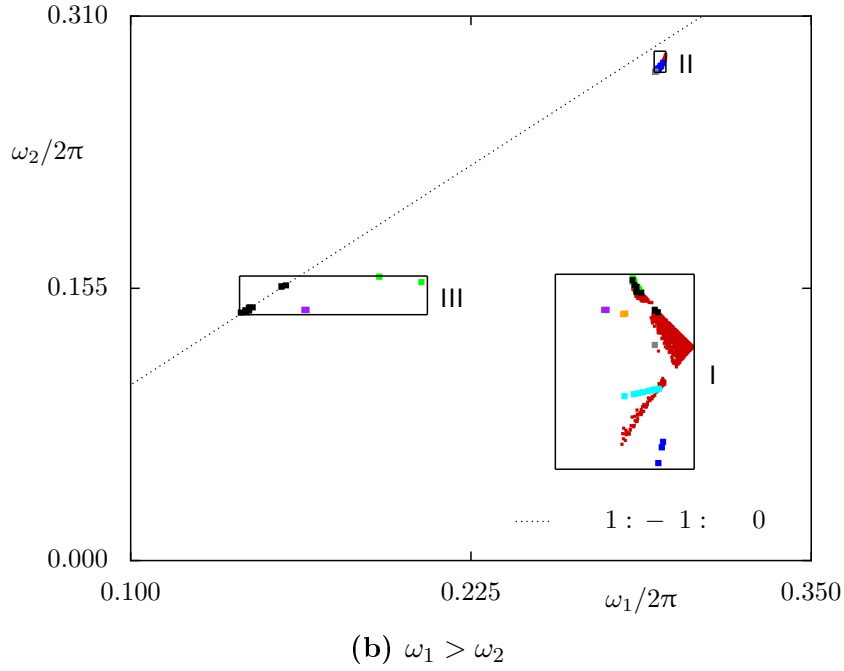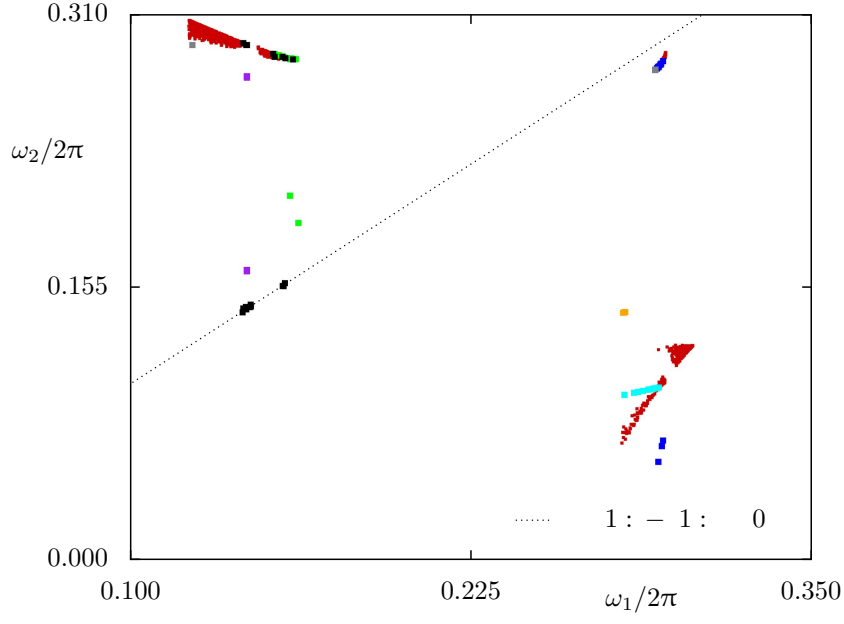
Figure 3.6: Inversion of frequencies, in order to fulfill $\omega_1 > \omega_2$, of the regular orbits considered in Figure 3.5. The frequencies are colored as in Figure 3.5, using a smaller section of frequency space. The dotted line represents the resonance $1 : -1 : 0$. The inversion causes all points above this line to be mirrored with respect to it. The subfigures show (a) the frequency space before the inversion, same as Figure 3.5(b), and (b) after the inversion. In (b) labeled boxes are inserted, demonstrating the sections of frequency space used for the following figures.

outlined for the blue colored frequencies, apply to the frequencies on the resonance $5:1:1$, colored green, on the resonance $1:3:1$, colored gray, and on the resonance $1:-1:0$, colored black. For the resonance $1:-1:0$ some of the problematic orbits turn out to be rather chaotic, as seen in phase space for the blue and green points in Figure 3.10. The most important deviations from these observations are the purple points, which are at first on the resonance $7:0:1$ and then on the resonance $7:0:2$, the orange points, which are at first on the resonance $4:1:1$ and then on the resonance $-1:2:0$, and the bright blue points, which stay for both projections on the resonance $-1:3:0$. This behavior is going to be explained once the frequency space is related to the phase-space section. It is important to emphasize, that Figure 3.5(b) shows a synthetic result, taking into account the frequencies obtained for both projections-planes, (p_1, q_1) and (p_2, q_2). The result for just the (p_2, q_2)-plane has the same problems as Figure 3.5(a), where different orbits have resonant frequencies.

It has to be pointed out, that the assignment of the frequencies ω_1 and ω_2 is exchangeable for every point. The algorithm assigns the most important frequency to ω_1 and the second most to ω_2. Since here all tori should be related to each other in frequency space, the global rule $\omega_1 > \omega_2$ is peferable. This rule causes all points above the diagonal line, the resonance $1:-1:0$, to be mirrored with respect to it, as is demonstrated in Figure 3.6. In the corrected frequency space in Figure 3.6(b) almost all orbits have incommensurable frequencies. Thus, their points are assumed to be uniformly distributed on the corresponding tori. Therefore, these regular orbits are considered to represent the regular tori not only in frequency space but also in the phase space.

Finally in Figure 3.7(a) the manually corrected frequency picture of the regular tori is shown and compared to the tori in a phase-space section in Figure 3.7(b). The regular tori form different clusters in frequency space and accordingly in phase space, which are denoted for future reference as the following: In Figure 3.7 the *central island* is colored in blue, the *outer ring* in green, the *period 7 islands* in purple and the *singled out structure* in orange. The orbits colored in bright blue in Figure 3.7 are further distinguished in Figure 3.9. There, the *horse-shoe* is colored in blue, the *inner end of the horse-shoe* in green, the *3-tower* in bright blue and the *top tower* in black. From these figures and Figure 3.10 also a rough spatial relation between the arrangement of the points in frequency space and their corresponding tori in the phase space section becomes apparent. For instance the gaps in frequency space between the central island and the outer structures, which are probably caused by the resonances $3:1:1$, $0:7:1$, and $-1:2:0$, as shown in Figure 3.7(a), are also found in the phase space section, as shown in Figure 3.7(b). In this sense gaps in the arrangement of the regular tori in the 4D phase space can be related to resonances.
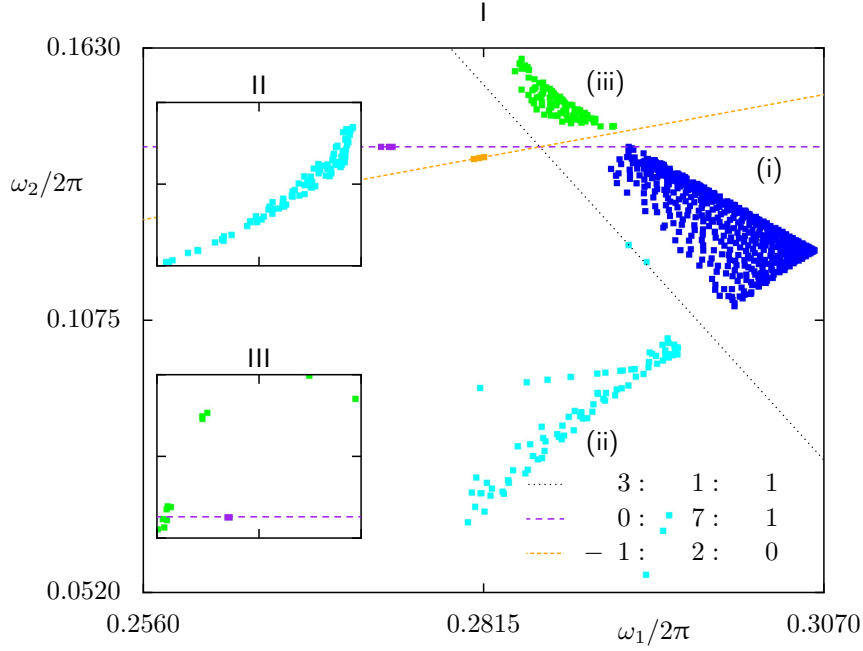
(a) Frequency space
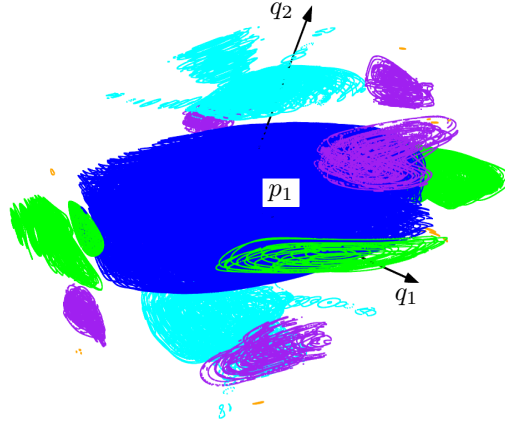
(b) Phase space

Figure 3.7: Comparison of regular orbits in frequency and phase space. The colors highlight different groups of orbits in (a) and (b). (a) The manually corrected frequencies of the regular orbits, same as in Figure 3.6(b). The big frame and the insets correspond to the boxes in Figure 3.6(b) according to their labels. The small letters (i),(ii),(iii) label the main groups of orbits, each considered separately in Figure 3.8. (b) The regular orbits are shown in the phase-space section $|p_2| < \epsilon$ (see Section 3.1.3).

(a) Frequency space

(b) Phase space
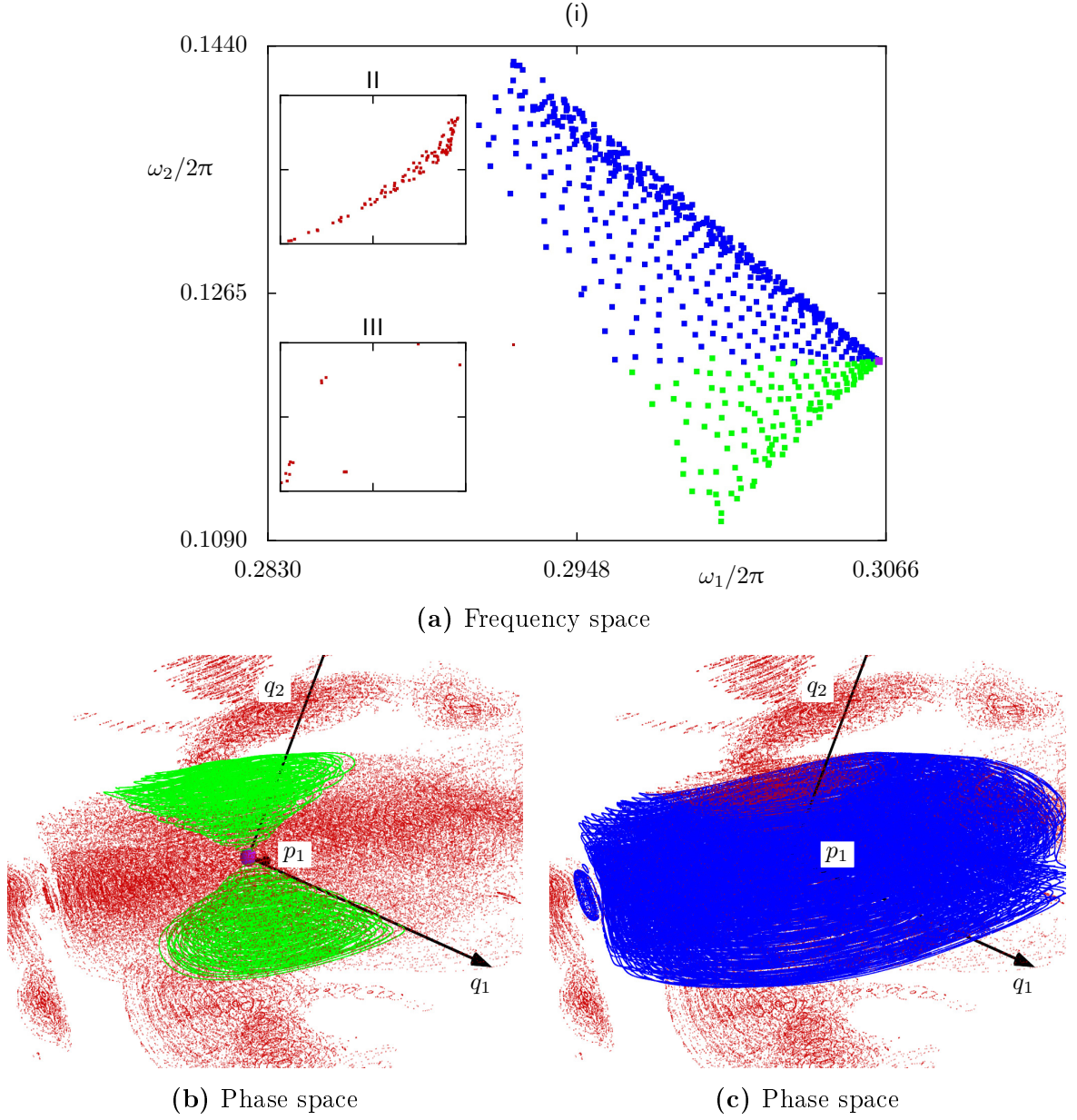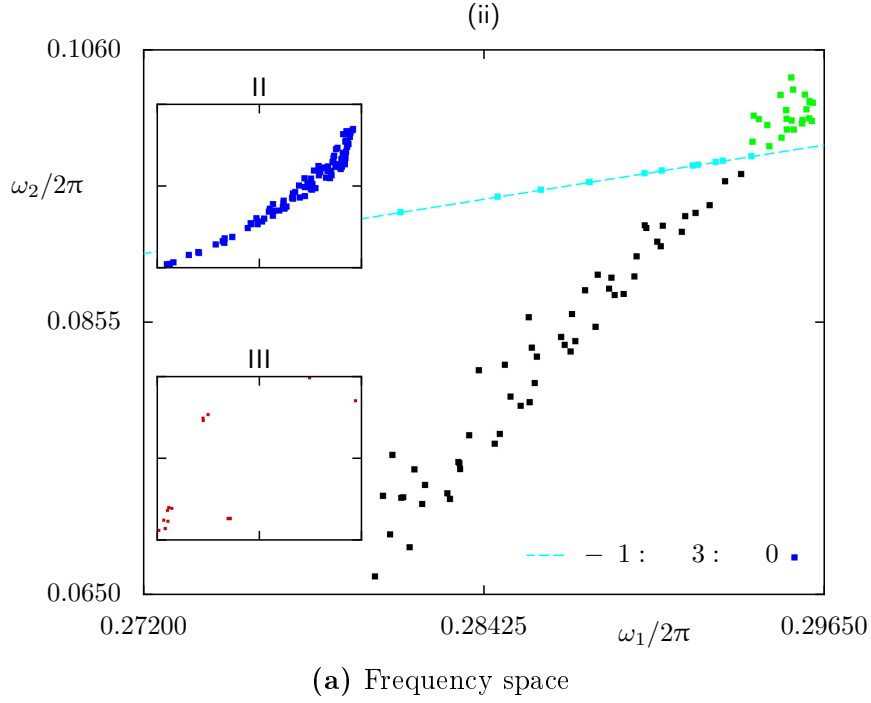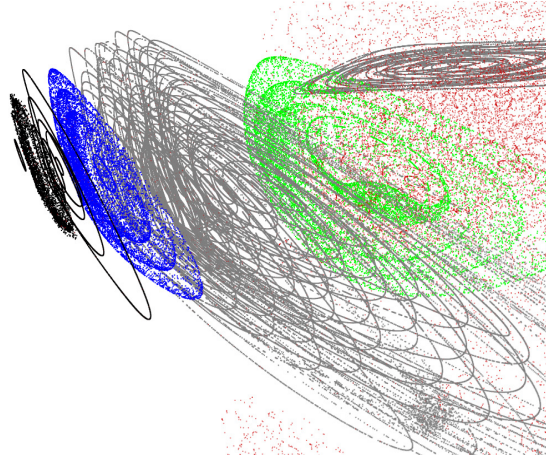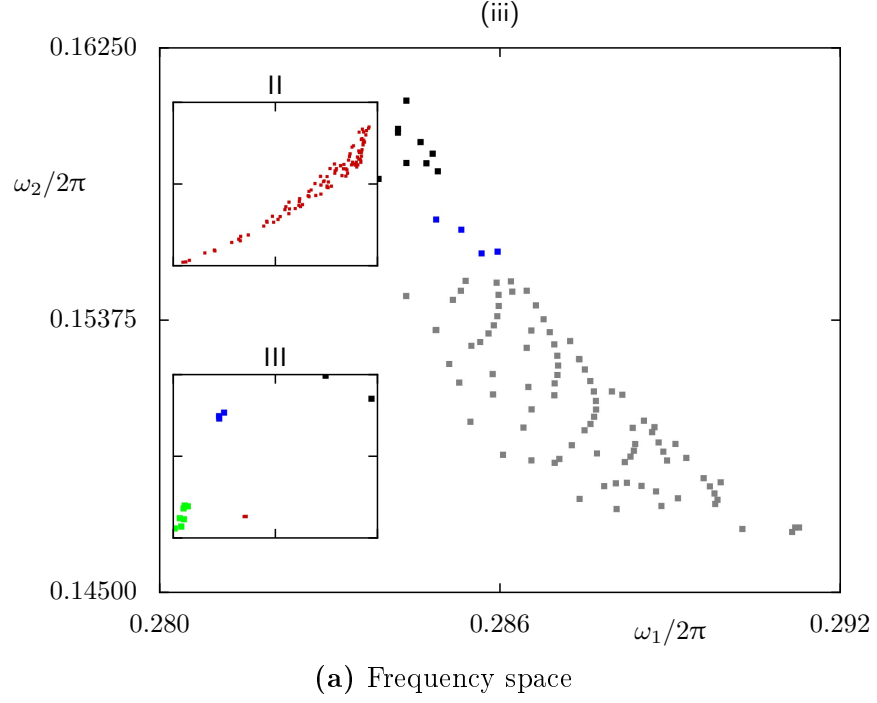

(c) Phase space

Figure 3.8: Comparison of regular orbits located in region (i) in Figure 3.7(a) in (a) frequency and (b, c) phase space. The labeled insets in (a) are the same as in Figure 3.7(a). In (a,b,c) smaller subgroups are highlighted with different colors. For comparision all other orbits (red) are inserted, but for better display of the higlighted structures in (b) and (c) only every 50th point is shown. In (b) and (c) different structures of the blue orbits of Figure 3.7(b) are magnified. In (b) only the green orbits of (a) are shown and in (c) only the blue orbits of (a) are shown. In (a) and (b) the central elliptic–elliptic fixed point, see Section 2.7.2, is indicated (purple point).

(a) Frequency space
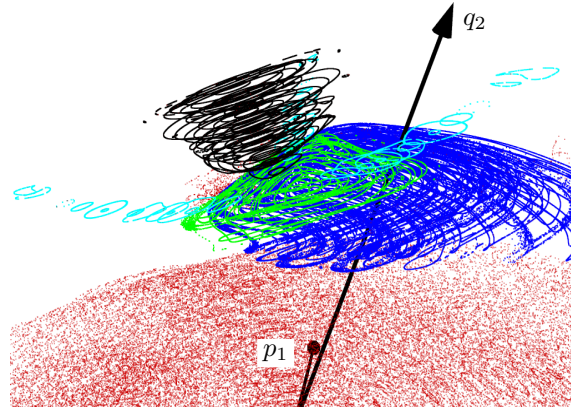
(b) Phase space

Figure 3.9: Comparison of regular orbits located in region (ii) in Figure 3.7(a) in (a) frequency and (b) phase space. The labeled insets in (a) are the same as in Figure 3.7(a). In (a,b) smaller subgroups are highlighted with different colors. For comparision all other orbits (red) are inserted, but for better display of the higlighted structures in (b) only every 50th point is shown. In (b) the bright blue orbits of Figure 3.7(b) are magnified.

(iii)

(a) Frequency space

(b) Phase space

Figure 3.10: Comparison of regular orbits located in region (iii) in Figure 3.7(a) in (a) frequency and (b) phase space. The labeled insets in (a) are the same as in Figure 3.7(a). In (a,b) smaller subgroups are highlighted with different colors. For comparision all other orbits (red) are inserted, but for better display of the higlighted structures in (b) only every 50th point is shown. In (b) the green orbits of Figure 3.7(b) are magnified.

The area-like structures in frequency space seem to have always a sharp edge, which looks like a line-shaped border the frequencies converge to, whereas the density of the points decreases irregularly going away from these borders. This property can be explained by looking at the phase-space section. The deformed ellipses representing the regular orbits in the phase-space section are stacked on top of each other, such that the centers of the ellipses form lines in the section. This is well visible for the top tower, colored in black, and the 3-tower, colored in bright blue, in Figure 3.9(b) and for the part of the outer ring, colored in gray, in Figure 3.10(b). Assuming a set of tori approaching one of these lines, consequently looking like ellipses with decreasing radius in the phase-space section, the frequencies of these tori form some line in frequency space. This line has to end at the innermost torus, which is just an ellipse with radius zero, a point. In the central island two of these borders meet forming an apex which points to the frequencies corresponding to the eigenvalues of the elliptic–elliptic fixed point at the center of the phase space, $\boldsymbol{\omega}/2\pi = (0.306315, 0.121726)$ as calculated in Section 2.7.2. In Figures 3.8(a) and 3.8(b) the fixed point is indicated by a purple point. Summing up all these facts and taking into account, that the line-shaped borders represent 2D manifolds, as noted above, these lines are expected to correspond to the center manifold. It should be emphasized, that the line-shaped borders emanating from the fixed point in frequency space seem to be continued after the resonance gaps, suggesting that in fact these lines majorly govern the structure of the regular tori in frequency space and thus also in phase space. Both of these conjectures are proved in chapter 4, especially by the results in Section 4.3.

Despite the spatial relation between frequency and phase space found above, the horse-shoe deviates in ω_2 from the expected position in frequency space. This is visible in Figure 3.9(a), where the blue points representing the horse-shoe are expected to be close to the green points, representing the inner end of the horse-shoe. Even considering a different set of independent frequencies for the points of the horse-shoe, as discussed in Section 3.2.2, does not restore a meaningful spatial relation. Although choosing $\boldsymbol{\omega} = (\omega_1, -4 \cdot \omega_1 + \omega_2)$ maps the horse-shoe, colored blue, in the frequency area of the inner end of the horse-shoe, colored green, the position of the edge of the horse-shoe still seems to be wrong. Also the frequencies of the singled out structure, colored orange in Figure 3.7(b), have not been understood. On the contrary, the other points on the resonances, such as the period 7 islands with the resonance $0 : 7 : 1$, and the 3-tower with the resonance $-1 : 3 : 0$ can be explained. The resonance $0 : 7 : 1$ forms 2 sets of regular islands around elliptic–elliptic fixed points of period 7, as can be demonstrated by the method of color and rotation, see Section 3.1.2. The frequency ω_1 of points of the period 7 islands, which is not $1/7 \cdot 2\pi$ in Figure 3.7(a), is therefore according to

Section 3.2.2 wrong. The orbits of the 3-tower are probably in the vicinity of an elliptic fixed line with a single-coupled resonance of $-1 : 3 : 0$. Such a fixed line, on which the dominant frequency ω_1 and the other ω_2 have a ratio of $|\omega_1 : \omega_2| = 1 : 3$, intersects a phase-space section at two times three points, where always three points are close to each other. That is, the torus of the fixed line intersects the phase-space section at two spots and the fixed line appears at each spot three times due to its frequency ratio. These three close by intersections are also seen in Figure 3.9(b) for the 3-tower, which has the characteristic structure of three towers.

Apart from the above mentioned exceptions the spatial relation between frequency space and phase space allows for understanding the principle arrangement of the regular tori in phase space by looking at their representation in frequency space. In this sense, the frequency analysis serves as a projection of the 4D phase space to a 2D space conserving the relevant information about the structure of the phase space.

4 Global structure of regular tori in 4D phase space

According to Section 2.4.1, the regular tori of a 2D map form a hierarchical structure of regular islands. On the contrary, much less is known about the structure of the tori of higher dimensional maps. These tori are found to be embedded in spheres, forming regular islands in which the Arnold diffusion is exceedingly slow [10]. But above that a large variety of lower dimensional, invariant manifolds exists in 4D maps.

In this section the global structure of the regular tori in a 4D phase space is revealed. Based on the observations made in Section 3.3 a concept is devised in Section 4.1 by which 2D tori can be assigned to 1D tori. An algorithm for finding these so-called central 1D tori is developed in Section 4.2. Finally, in Section 4.3 the central 1D tori are found to compose global 2D invariant manifolds, which act as a skeleton of the regular structures. The manifolds are identified as center manifolds and remains of families of resonant tori.

4.1 Concept of central 1D tori

The frequency-space representation of regular tori of the strongly coupled 4D map F_{SC} in Figure 3.7(a) and its discussion in Section 3.3 suggest a great importance of the central elliptic–elliptic fixed point and the two line-shaped barriers, which emanate from it, for the global arrangement of the frequency space. As pointed out in Section 3.3 the ellipses representing the 2D regular tori seem to be stacked on top of each other, such that the centers of the ellipses form 1D lines in the section. Therefore, these are denoted as center lines. Metaphorically speaking the ellipses look like they are stringed on a lace. The ellipses that are closer to such an imaginary center line seem to have a smaller radius. This trend can be extrapolated by conceiving regular tori appearing in the section as ellipses with even smaller radius. This conception converges to tori appearing as points on the center line. The corresponding tori in phase space are consequently expected to be 1D fixed lines rather than 2D surfaces. This means that the center lines in the phase-space section represent 2D manifolds consisting of 1D tori. There are only two related

families of objects in phase space, namely the 1D fixed lines, resulting from rank one resonances as described by Todesco [11] and center manifolds, which are invariant 2D manifolds attached to elliptic fixed points. For instance the center lines of the central island intersect at the central elliptic–elliptic fixed point, thus are suspected to be two center manifolds of this fixed point. However, such a relation to some periodic orbit is not possible for all center lines, e.g., no fixed point is found on the center line of the outer ring.

In order to clarify the raised questions about the origin of the 1D fixed lines the concept of the central 1D tori is devised. The mentioned thought experiment takes place in a phase-space section. From examining the regular tori in different sections and projections the following idea emerges, which is the equivalent of the thought experiment in the complete phase space. The idea is, that every 2D torus *contains* other tori. Of course the 2D torus can not surround a part of the 4D phase space in the conventional sense. In this context *containing* refers to a 3D projection of the phase space, where the torus looks like a closed tube. In this sense, another torus with almost the same shape but slightly less size is contained in the first one. The same applies to this smaller torus. This idea is for example illustrated in Figure 4.1. Thus, in the 3D projection every tori can be thought of a tube containing infinitely many smaller tubes. The relation of containment holds for every chosen 3D projection of the 4D phase space. Conversely, most 2D tori are in this sense contained in another torus of slightly bigger size, supposedly up to some final torus, which is just surrounded by chaos. The explicit character of this transition is neglected here, since the focus lies rather on the innermost tori. The innermost tori are consequently lines, denoted here as central 1D tori. Considering a family of such central 1D lines, each line being surrounded by layers of 2D tori, the combination of all such families results in the complete set of the regular tori. Thus the global structure of the regular tori is based on central 1D tori and their relation to each other.

The central 1D tori have to be acquired numerically, in order to manifest their existence and importance as well as their relation to each other. Such tori are unlikely to be found by a grid-based search algorithm, due to the low dimensionality, which explains their absence in the presented figures of the phase-space sections. At the same time, as it is discussed in the previous sections about frequency analysis, such tori can not be mapped numerically to the frequency space since they have only one measurable frequency. As tori get closer to the central 1D torus the evaluation of the second frequency, belonging to the mapping in the direction that vanishes for the central 1D torus, becomes harder and finally impossible. However, both frequencies should converge, when approaching a central 1D torus. Therefore, it is suggested in Section 3.3

that the barriers in frequency space correspond to the position of the central 1D tori.

4.2 Finding central 1D tori

Based on the geometry of the tori conjectured in Section 4.1 an algorithm for finding some of the central 1D tori in a phase space is developed. The algorithm uses an orbit on a 2D torus to find an orbit on a 2D torus, which is contained by the first one. This procedure converges to the corresponding central 1D torus. Thus, applying the algorithm to different sets of 2D tori, e.g., obtained from a grid-based search algorithm, results in arbitrary many central 1D tori for every desired region of phase space.

4.2.1 Inverse action–angle mapping

Consider a torus of an integrable system whose frequencies $\boldsymbol{\omega}$ were obtained by frequency analysis of an orbit $\boldsymbol{x}(t)$ on the torus as described in Section 3.2.3. The initial point $\boldsymbol{x}_0$ of the orbit can be expressed in action–angle coordinates as $(\boldsymbol{I}_0, \boldsymbol{\Theta}_0)$, see, e.g., Section 2.3. Accordingly, the orbit $\boldsymbol{x}(t)$ resulting from mapping the initial point $\boldsymbol{x}_0$ can be expressed in terms of the action–angle coordinates $(\boldsymbol{I}(t), \boldsymbol{\Theta}(t))$, see Eq. (2.4),

$$\boldsymbol{I}(t) = \boldsymbol{I}_0 \,,$$
$$\boldsymbol{\Theta}(t) = \boldsymbol{\Theta}_0 + \boldsymbol{\omega}t \,,$$

which, ignoring the action, leads to a relative angle $\triangle\boldsymbol{\Theta}$

$$\triangle\boldsymbol{\Theta}(t) \equiv \boldsymbol{\Theta}(t) - \boldsymbol{\Theta}_0 = \boldsymbol{\omega}t \tag{4.1}$$

that stands for a coordinate on the torus relative to the initial point $\boldsymbol{x}_0$. Eq. (4.1) formulates $\triangle\boldsymbol{\Theta}$ as a function of time t. However, this relation can be reversed in the following sense.

In the generic case, meaning incommensurable frequencies $\boldsymbol{\omega}$, the vector $\triangle\boldsymbol{\Theta}$ gets arbitrarily close to every point on the 2D torus $\mathbb{T}^2$, see Section 2.3. Explicitly, $\forall \boldsymbol{\theta} \in \mathbb{T}^2$, $\epsilon > 0$, $\exists t \in \mathbb{Z}$:

$$||\boldsymbol{\theta} - \triangle\boldsymbol{\Theta}(t)|| \stackrel{\mathrm{Eq.\ (4.1)}}{=} ||\boldsymbol{\theta} - \boldsymbol{\omega}t|| < \epsilon \tag{4.2}$$

with $||\cdot||$ denoting the Euclidean norm on $\mathbb{T}^2$ and keeping in mind that all quantities are defined only on the torus $\mathbb{T}^2$, that is, e.g., $(\boldsymbol{\omega}t)$ actually reads $(\boldsymbol{\omega}t \mod 2\pi)$. Consequently a function $t_M(\boldsymbol{\theta})$, which numerically approximates the inverse map of Eq. (4.1),

can be defined on the domain $\mathbb{T}^2$ with a parameter $M \in \mathbb{N}$ by

$$D_M \equiv \mathbb{Z} \cap (-M, M)$$
$$t_M(\boldsymbol{\theta}) \equiv \min\{t \in D_M \colon ||\boldsymbol{\theta} - \boldsymbol{\omega}t|| = \min_{t' \in D_M} ||\boldsymbol{\theta} - \boldsymbol{\omega}t'||\}\,. \tag{4.3}$$

The inverse map of Eq. (4.1), formally denoted by $t(\boldsymbol{\theta})$, is then numerically approximated by

$$t_M(\boldsymbol{\theta}) \xrightarrow{M \gg 1} t(\boldsymbol{\theta})\,. \tag{4.4}$$

Note that the outermost minimum in Eq. (4.3) is merely introduced to ensure the right-uniqueness of the inverse map. Furthermore, *numerically* refers to the fact that concerning the numerics, the resulting $\boldsymbol{\omega} \cdot t_M(\boldsymbol{\theta})$ gets sufficiently close to $\boldsymbol{\theta} = \boldsymbol{\omega} \cdot t(\boldsymbol{\theta})$, whereas the existence of the mathematical limit of Eq. (4.4) is not guaranteed. Unless $\boldsymbol{\theta}$ is an element of the set $\{\boldsymbol{\omega} \cdot t\}_{t \in \mathbb{Z}}$, the value of $t_M(\boldsymbol{\theta})$ in Eq. (4.4) goes to infinity for $M \to \infty$, due to the the fact, that this set is dense on the torus $\mathbb{T}^2$, provided $\boldsymbol{\omega}$ is incommensurable.Nevertheless, since only a finite accuracy $\epsilon_{\min} > 0$ is needed for the numerics, a finite $t < \infty$ can be found fulfilling Eq. (4.2) for this $\epsilon_{\min}$.

Given an initial point $\boldsymbol{x}_0$ on a torus and angles $\boldsymbol{\theta}$, the above algorithm allows for calculating a point $\boldsymbol{x}_0'$ in phase space, which lies on the same torus as $\boldsymbol{x}_0$ but is located at angles differing by $\boldsymbol{\theta}$ from the angles of $\boldsymbol{x}_0$. The most important aspect of this algorithm is that the knowledge of the action–angle coordinates is not needed. Instead of determining the transformation to action–angle coordinates, just a natural number $t(\boldsymbol{\theta})$ is obtained by the numerical implementation of Eq. (4.3) and Eq. (4.4), the initial point $\boldsymbol{x}_0$ is mapped $t(\boldsymbol{\theta})$ times and the resulting point in phase space is in some vicinity of the desired $\boldsymbol{x}_0'$.

Some applications are imaginable for the numerical inverse $t(\boldsymbol{\theta})$ described above. For instance the local base vectors $\{\boldsymbol{e}_{\Theta_i}(\boldsymbol{\Theta}_0, \boldsymbol{I}_0)\}_{i=1\ldots N}$ of the angles and consequently the dual vector space of the local base vectors $\{\boldsymbol{e}_{I_i}(\boldsymbol{\Theta}_0, \boldsymbol{I}_0)\}_{i=1\ldots N}$ of the actions could be approximated using $\boldsymbol{\theta}^{(i)} \equiv \epsilon \cdot \boldsymbol{e}_{\Theta_i}$ with some small $\epsilon > 0$. From the initial point $\boldsymbol{x}_0$ mapped $t(\boldsymbol{\theta}^{(i)})$ times, leading to the picture $\boldsymbol{x}_0^{(i)}$, it follows then

$$\boldsymbol{e}_{\Theta_i}(\boldsymbol{\Theta}_0, \boldsymbol{I}_0) = \frac{\boldsymbol{x}_0^{(i)} - \boldsymbol{x}_0}{\epsilon}\,.$$

Concerning the problems discussed in Section 3.2.2, $t(\boldsymbol{\theta})$ may be also used to check the results of the frequency analysis for an orbit on a torus. As is explained in Section 3.2.2, in some cases the numerical analysis of the fundamental frequencies returns a finite set

of $M > N$ possible frequencies $\{\omega_i\}_{i=1\ldots M}$ of which N are the correct fundamental frequencies, where N is the number of degrees of freedom. When applying the inverse action–angle mapping with the setting $\boldsymbol{\theta} = \mathbf{0}$ and $t(\boldsymbol{\theta}) \neq 0$ for the correct N frequencies the accordingly mapped point $\boldsymbol{x}_0'$ is in the vicinity of the initial point $\boldsymbol{x}_0$, whereas for any other subset of frequencies the point $\boldsymbol{x}_0'$ should differ much from $\boldsymbol{x}_0$. Therefore, considering all possible N-tuple of the frequencies $\{\omega_i\}_{i=1\ldots M}$, looking for the smallest deviation of $\boldsymbol{x}_0'$ from $\boldsymbol{x}_0$, should lead to the wanted fundamental frequencies.

The numerical difficulties and effectiveness of such applications are not particularly discussed here, but may be inferred from the outline of the method designed to find the central 1D torus in Section 4.2.2 and especially Section 4.2.3.

4.2.2 Algorithm

Consider a given initial point $\boldsymbol{x}_0$ on a 2D torus, whose frequencies $\boldsymbol{\omega}$ are obtained by frequency analysis. Such a torus is presented in Figure 4.1(a) by a 3D projection, see Section 3.1.2, where $\boldsymbol{x}_0$ is indicated by a red point. The torus looks like the deformed version of a long, thin ring torus with radii $R_{\Theta_1} > R_{\Theta_2}$. Consequently, the change of Θ_1, due to the mapping, e.g., as formulated in Eq. (4.1), is spatially more relevant than the change of Θ_2 and therefore the dominant frequency ω_1 belongs to the mapping of Θ_1, whereas the other frequency ω_2 belongs to Θ_2. Hence using the numerical inverse $t(\boldsymbol{\theta})$ developed in Section 4.2.1 with $\theta_1 = 0$ and $\theta_2 = \pi$ for the initial point $\boldsymbol{x}_0$ a point $\boldsymbol{x}_0'$ is computed, that lies geometrically on the opposite site of the torus with respect to Θ_2, but at the same Θ_1. In the close-ups on the example torus in Figures 4.1(b) and 4.1(c) this is well visible, where $\boldsymbol{x}_0$ and $\boldsymbol{x}_0'$ are indicated by the red point and the blue point on the outermost torus. The line from $\boldsymbol{x}_0$ to $\boldsymbol{x}_0'$ is completely contained by the torus in every 3D projection of the system and is depicted in Figures 4.1(b) and 4.1(c) as the black line between the red point and the blue point. The point $\boldsymbol{x}_1$ half way between the opposing points

$$\boldsymbol{x}_1 \equiv \frac{\boldsymbol{x}_0' - \boldsymbol{x}_0}{2} + \boldsymbol{x}_0$$

lies on a torus, that is closer to the central 1D torus, according to Section 4.1. Such a $\boldsymbol{x}_1$ is indicated by another red point in the middle of the mentioned black line in Figures 4.1(b) and 4.1(c). Also the torus $\boldsymbol{x}_1$ lies on is shown there, looking like a tube within the outer torus. The described procedure can be applied again to this new initial point $\boldsymbol{x}_1$, as it is demonstrated in Figure 4.1(d). Thus the central 1D torus is approached iteratively. This is well illustrated for the example torus in the plots

of Figure 4.1. In this case the central 1D torus is approximated very well in a few iterations. The convergence is confirmed by the fact, that the last red and blue points lie almost on one line in Figure 4.1(d).

The outlined algorithm works at least for tori fulfilling the above criterion $R_{\Theta_1} > R_{\Theta_2}$. In these cases the dominant frequency ω_1 undoubtedly belongs to Θ_1. The algorithm should also work for the case that the radii R_{Θ_1} and R_{Θ_2} get close to each other, e.g., for spindle tori, although the correspondence between the angles $\boldsymbol{\Theta}$ and the frequencies $\boldsymbol{\omega}$ is not expected to work as simple as assumed above. Additionally, the principle of the method may work for tori with other dimensionality. For instance in a 2D Hamiltonian system the algorithm would converge from a 1D torus of a regular island to the corresponding elliptic fixed point.

4.2.3 Discussion of pitfalls

There are some numerical obstacles for both methods, the mere numerical inverse $t(\boldsymbol{\theta})$ developed in Section 4.2.1, and the algorithm for finding the central 1D tori. Nevertheless, the results obtained by using them, e.g., as presented in Section 4.3, prove their usefulness. It also has to be emphasized that the methods deal with a geometric structure within a 4D space without requiring its visualization. The 3D projections are just used here for visualizing the concept.

First of all the methods inherit the issues of the frequency analysis, which were already discussed in Section 3.2.2. Problematic are tori of the single-uncoupled case and the double resonant case, which split up into several disjoint parts. Regular orbits of their elliptic surrounding might not converge to the wanted central 1D torus. This can be overcome by using only points belonging to one of the disjoint components instead of the whole orbit.

Likewise problematic are tori T_P that remain from the perturbation of a torus T_0 with a single-coupled resonance. Such a torus T_P is a fixed line around the central 1D torus $T_{1\mathrm{D}}$ of the unperturbed torus T_0. Thus, the algorithm converges as expected for this torus T_P to the central 1D torus $T_{1\mathrm{D}}$. On the contrary, the central 1D torus of a regular orbit from the elliptic surrounding of the fixed line T_P is T_P, according to the definition of the central 1D torus in Section 4.2. However, for such an orbit the frequencies of the torus T_P are obtained because these frequencies are spatially more relevant than the frequencies of the orbit. Hence, the orbit converges to $T_{1\mathrm{D}}$ rather than to T_P.

But even if the correct frequencies of a torus are calculated, they are only known with a certain accuracy, thus limiting the interval $[-M, M]$ for the iterations t as denoted in Section 4.2.1 in which the numerical inverse $t_M(\boldsymbol{\theta})$ is sufficiently accurate. Influences
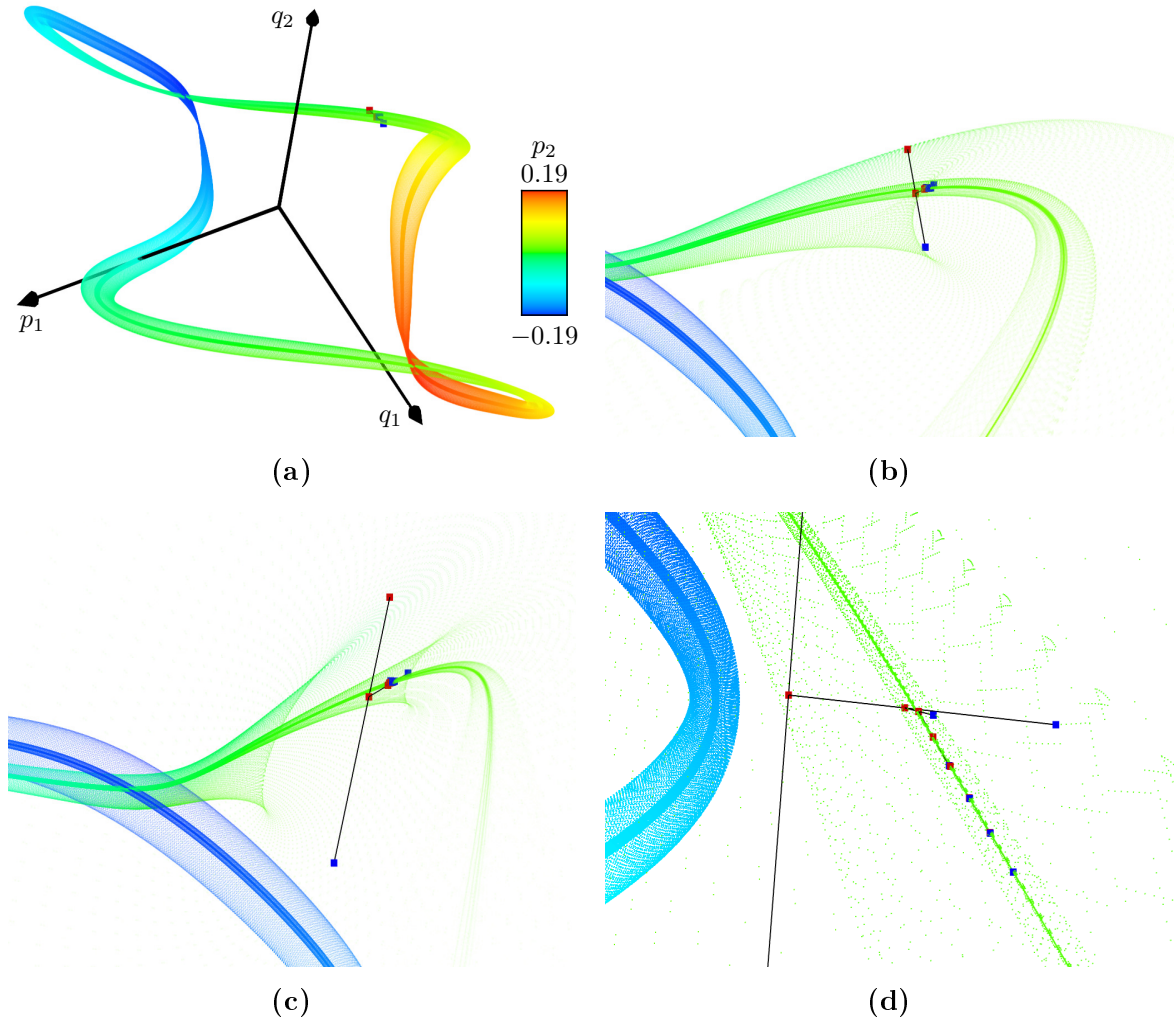
Figure 4.1: Example for the convergence to the central 1D torus from a torus of the horse-shoe as described in the text. The tori are projected to the (p_1, q_1, q_2)-space (see Section 3.1.2) and shown for different zooms and perspectives. The initial points $\boldsymbol{x}_0$ (red points) and the opposing points $\boldsymbol{x}'_0$ (blue points) on every tori as well as $(\boldsymbol{x}'_0 - \boldsymbol{x}_0)$ (black lines) for all iterations steps of the algorithm are shown. The innermost points in (d) lie almost on one line, demonstrating the convergence of the algorithm.

of other numerical errors, e.g., rounding errors due to the mapping, can be neglected compared to the error of the frequency analysis as mentioned in Section 3.2.3. Additionally, the evaluation of the second frequency ω_2 becomes harder as the obtained tori approach the central 1D torus, since the second radius R_{Θ_2} vanishes. Based on the assumed convergence of the frequencies mentioned in Section 4.1, the frequency ω_2 is kept constant from some iteration on and used for all following tori. Therefore, only the dominant frequency ω_1 is updated.

In order to guarantee numerical convergence towards the desired central 1D torus, it is sufficient that the initial point $\boldsymbol{x}_1$ for the next iteration is contained in the previous torus by means of 3D projections. Therefore, it is more important to get a point with the right $\triangle\Theta_1 = 0$ than with the right $\triangle\Theta_2 = \pi$, keeping in mind that the corresponding radii fulfill typically $R_{\Theta_1} > R_{\Theta_2}$. If $\triangle\Theta_1$ is off, the vector $(\boldsymbol{x}_0' - \boldsymbol{x}_0)$ might not be completely within the torus. In contrast to that, a wrong $\triangle\Theta_2$ leads to a slow convergence at most. Thus the norm used in the term $||\boldsymbol{\theta} - \boldsymbol{\omega}t||$ in Eq. (4.3) has to weight the angles accordingly. Taking into account this inconvenient weighting and poor convergence of the second most important frequency ω_2, a slight variation of the method can be reasonable. Instead of finding the opposite point $\boldsymbol{x}_0'$, several points at the same dominant angle $\triangle\Theta_1 = 0$ can be found, regardless of the second angle $\triangle\Theta_2$. The next initial point $\boldsymbol{x}_1$ can be defined as their mean, based on the fact that a point x_1 only has to lie within the previous torus by means of 3D projections. This variation is already successfully used by Onken [62].

4.3 Center manifolds

The method described in Section 4.2 is applied to the tori, which are shown in Section 3.3. For each torus the procedure is run 15 times, with the errors of the angles weighted $|\omega_1 \cdot t(0, \pi)| : |\omega_2 \cdot t(0, \pi) - \pi| = 1 : 10$. Not converged tori are manually sorted out. Figure 4.2 shows the resulting 1D tori. They are visualized by means of a phase-space section in Figure 4.2(a) together with regular orbits known from Section 3.3. In Figure 4.2(b) the 1D tori are shown by a projection. The latter plot also contains the points of the 1D tori that are visible in the phase-space section in Figure 4.2(a), as well as four periodic orbits.

The intersection points of the central 1D tori in Figure 4.2(a) indicate the expected central lines, forming a coarse skeleton for the regular tori shown in red. Some center lines are missing, e.g., for the 3-tower. This is due to the problems of the frequency analysis, mentioned in Section 4.2.3. In Onken [62] the center lines for the 3-tower are found by dividing the obtained dominant frequency by three, as is suggested by the

(a) Phase space section, $|p_2| < \epsilon$

p_2
0.24

-0.24
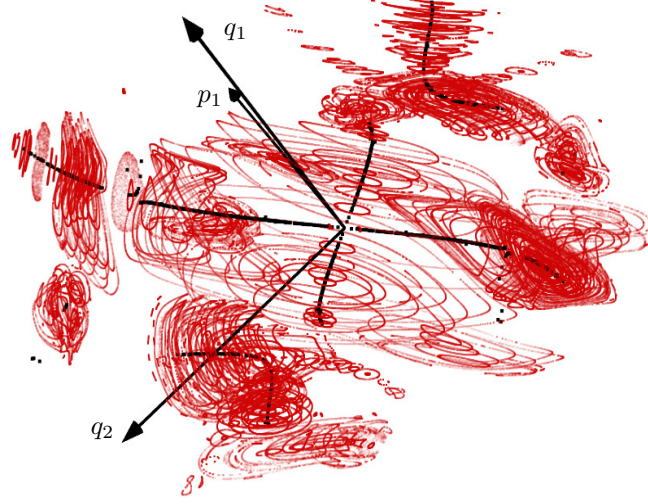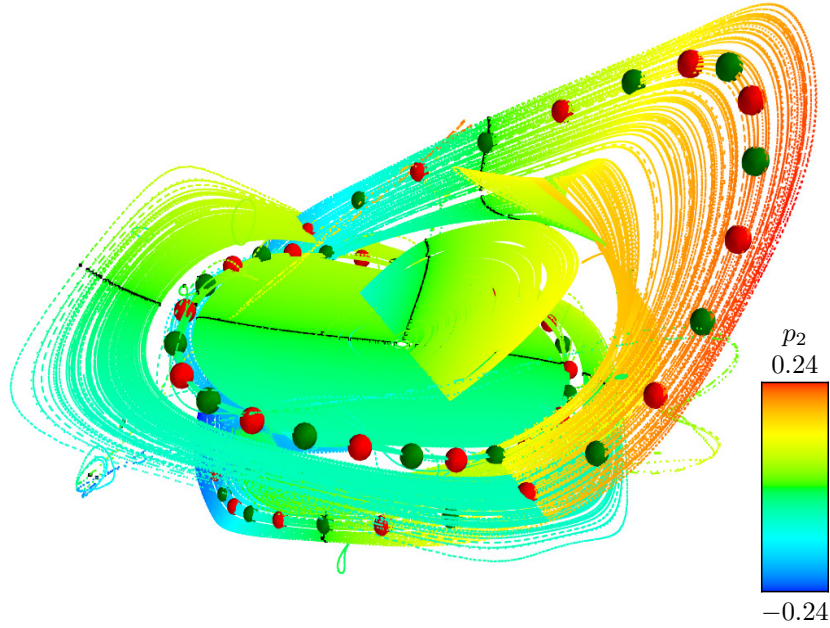
(b) Projection

Figure 4.2: Central 1D tori in the phase-space section $|p_2| < \epsilon$ (see Section 3.1.3) and projected to the (p_1, q_1, q_2)-space (see Section 3.1.2). (a) The phase-space section shows the central 1D tori (black points) and regular tori (red). (b) For comparison in the projection the intersection points (black) of the central 1D tori with the phase-space section are depicted. The red and green spheres indicate elliptic–elliptic and elliptic–hyperbolic periodic orbits of period seven. They are obtained by a Newton-Raphson method based search for fixed points. They form a chain of 14 elliptic-elliptic and elliptic-hyperbolic points on each center manifold.

discussion in Section 3.2.2. The central lines within the central island intersect at the central elliptic–elliptic fixed point. It has to be pointed out, that these central lines can even be continued across resonances. This is visible above and below the central island. These gaps correspond exactly to the gaps in frequency space discussed in Section 3.3. At the resonances disrupting the center manifold the center lines look like a function having a pole of odd order. This behavior is observable at all major resonances. This continuation of the center lines across resonances is also visible in the frequency space in Figure 3.7(a). There the line-shaped edges also extent beyond resonance gaps.

The 3D projection of the central 1D tori in Figure 4.2(b) indicates the expected 2D manifolds. The two large manifolds in the vicinity of the central elliptic–elliptic fixed point are tangential to the elliptic eigenspaces of this fixed point (not shown in Figure 4.2(b)). This suggests that these manifolds, each consisting of a family of central 1D tori, are actually the center manifolds of this fixed point. Therefore, the algorithm for finding the central 1D tori can be used as a method for computing the center manifolds of purely elliptic fixed points of a system. This is even possible without knowing the fixed points.

Furthermore, the extension of the manifolds across resonances suggests that the center manifolds also exist beyond the resonance gaps. At resonances they break up in a way, that looks like a 2D version of a pole with odd order. This means that all tori of the structures denoted in Section 3.3 as central island, the horse-shoe, the inner end of the horse-shoe, the top tower and the outer ring are directly related to the center manifolds of the elliptic–elliptic fixed point in a way that is comparable to the relation between tori of a regular island and its elliptic fixed point in a 2D system.

There are features disturbing the center manifolds. One are the period 7 islands, which are the result of a double resonance. Another one are the center lines of the 3-tower as a family of elliptic fixed lines remaining from all tori with the same single-coupled resonance, probably some $3:1$ resonance. Apart from these two cases only the singled out structure is left in the understanding of the global structure of the regular tori. Further studies on the global structure of phase space and the central 1D tori are done by Onken [62].

Note that the method presented here is an alternative to the otherwise used algebraic approximation of the center manifolds, as mentioned in Section 2.5.2. The disadvantage of such an algebraic approach is that it only works up to a major resonance, where the pole like behavior prevents further convergence beyond the resonance.

In Figure 4.2(b) also four periodic orbits are shown. They seem to form lines of elliptic–hyperbolic and elliptic–elliptic periodic orbits on the center manifolds. This indicates that the 4D map acts on the 2D invariant manifolds like a 2D symplectic map.

This is expected for the center manifolds as is mentioned in Section 2.5.2, but is not clear for the here considered disturbed center manifolds broken by resonances.

In conclusion, the global arrangement of the regular tori in 4D phase space is majorly determined by families of central 1D tori, representing either center manifolds or families of elliptic fixed lines remaining from tori with the same single-coupled resonance. All other tori form layers around these central 1D tori, as explained in Section 4.1 and demonstrated in Figure 4.1 up to some outer tori. The character of the transition from the outer tori to the chaotic sea is not studied in this thesis, but further investigations about the structure can be found in Onken [62]. The phase-space structure is confirmed in frequency space, as described in Section 3.3 and shown in Figure 3.7. There the families of central 1D tori are indicated by line-shaped barriers, with clouds of regular tori on just one side. Greater distance of a torus from its central 1D tori corresponds to greater distance from the corresponding barrier in frequency space. Based on this insight, the position of trapped orbits as investigated in chapter 5, especially in Section 5.2, can be understood.

5 Trapping in generic 4D maps

In this chapter the trapping in generic 4D symplectic maps is investigated. As mentioned in Section 2.7.2 the focus lies on the strongly coupled map F_{SC}. However, the results for the weakly coupled system F_{WC} can be found in appendix A.2.

First the statistics of Poincaré recurrences $P(t)$ are discussed in Section 5.1. Then, trapped orbits with large Poincaré recurrences t are examined in phase space in Section 5.2. Based on these trapped orbits a sticky region can be identified in frequency space in Section 5.3. Finally, the transport within the sticky region is analyzed in Section 5.4.

5.1 Poincaré recurrence statistics

In order to investigate the trapping in 4D maps, first of all the Poincaré recurrence statistics, see Section 2.2, are determined for the given systems F_{SC} and F_{2D}, see Eqs. (2.13) and (2.11) respectively.

The region of initial points Γ needed for the Poincaré recurrence statistics should fulfill two prerequisites. On the one hand Γ should lie far away from the regular region. This ensures that all orbits are clearly started outside of a sticky region enveloping the regular tori, which governs the trapping mechanism. On the other hand Γ should be a large subset of phase space, since this reduces the average time needed by untrapped orbits to return to Γ. As these orbits are of no interest to this investigation but their consideration is numerically costly [20], this makes the calculations more efficient. Also in case of a large region Γ, trapped orbits that have left the sticky region have a smaller chance to be trapped again. So it can be assumed that the observed effects result merely from the properties of the sticky region and not from repeated trapping in the sticky region.

Therefore Γ is chosen consistently for all considered maps to be

$$\Gamma \equiv \left\{ \boldsymbol{x} \in U : x_{N+1} < 0.1 \right\}, \tag{5.1}$$

that is all points of the phase space, whose first position variable is smaller than 0.1.

This means $q_1 < 0.1$ for the 4D map F_{SC} and $q < 0.1$ for the 2D F_{2D} map. The condition that Γ lies completely in the chaotic sea is checked via visualizations of the phase space. For F_{SC} the visualization methods introduced in Section 3.1 are used. For both maps Γ covers 10% of phase space.

About 10^{11} initial points distributed on a uniform grid on Γ are used for the 4D maps[1] and the 2D map F_{2D}[2]. Each initial point is iterated until its first return to Γ.

Figures 5.1(a) and 5.1(b) show the distributions of the Poincaré recurrences $P(t)$ for the strongly coupled 4D map F_{SC} and the 2D map F_{2D} respectively. In both cases a power-law behavior $P(t) \sim t^{-\gamma}$ with similar exponent γ is observed for large times t. According to the literature, see Section 2.2, γ is expected to be smaller for the 4D map than for the 2D map. However, Shepelyansky observes an increase of γ for increasing perturbation of a system [32]. In this context, the large value of γ might be due to the strong perturbation of F_{SC}.

For F_{2D} oscillations of $P(t)$ in logarithmic scale are visible. This deviation from the power-law in the 2D case is accounted for in Section 2.4.2. Shepelyansky observes such oscillations also in higher dimensional systems, but points out that their amplitude is significantly smaller than in the 2D case [32]. Unlike there, such oscillations are completely absent for F_{SC}. This might be due to the strong perturbation of F_{SC}.

Finally, despite the fact that the regular region in the 4D case takes up a smaller percentage of phase space than in the 2D case, see Section 2.7, the number of orbits, which are trapped for very large times, is of the same magnitude.

Thus, it can be concluded, that the used 4D map F_{SC} exhibits the expected power-law behavior, which results from orbits with very large return times, i.e., trapped orbits.

---

[1] $(501 \cdot 1001)^2$ initial points

[2] For every point of a coarse grid of 102×1001 points in the (p_2, q_2)-plane a finer grid of 1001×1001 points on the $(p_1, (q_1 < 0.1))$-plane is set up. According to Eq. (5.1) this is a grid on Γ.
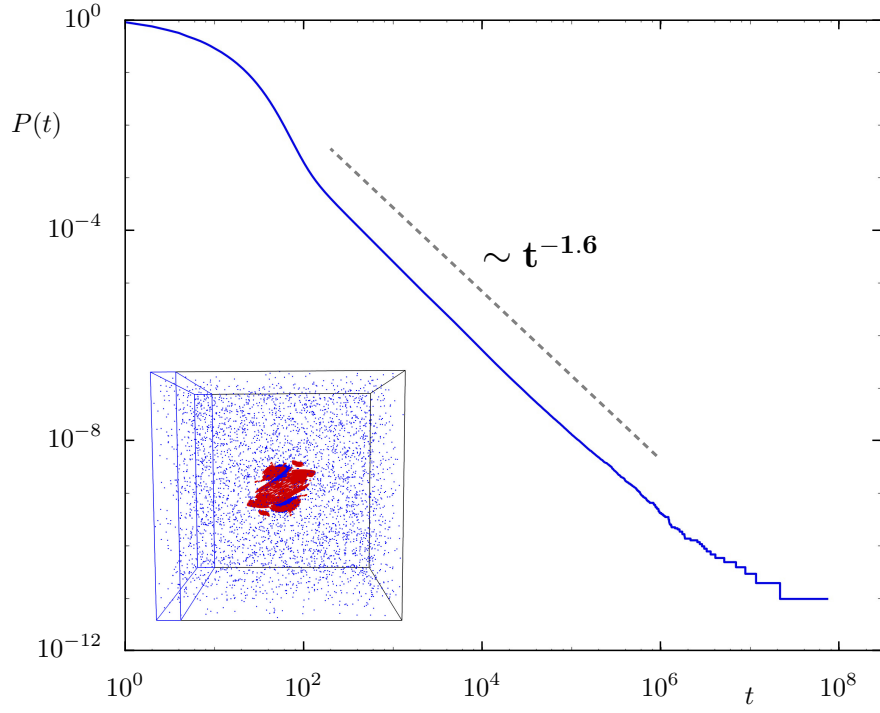
(a) 4D map F_{SC}, $\gamma_{fit} = 1.62$
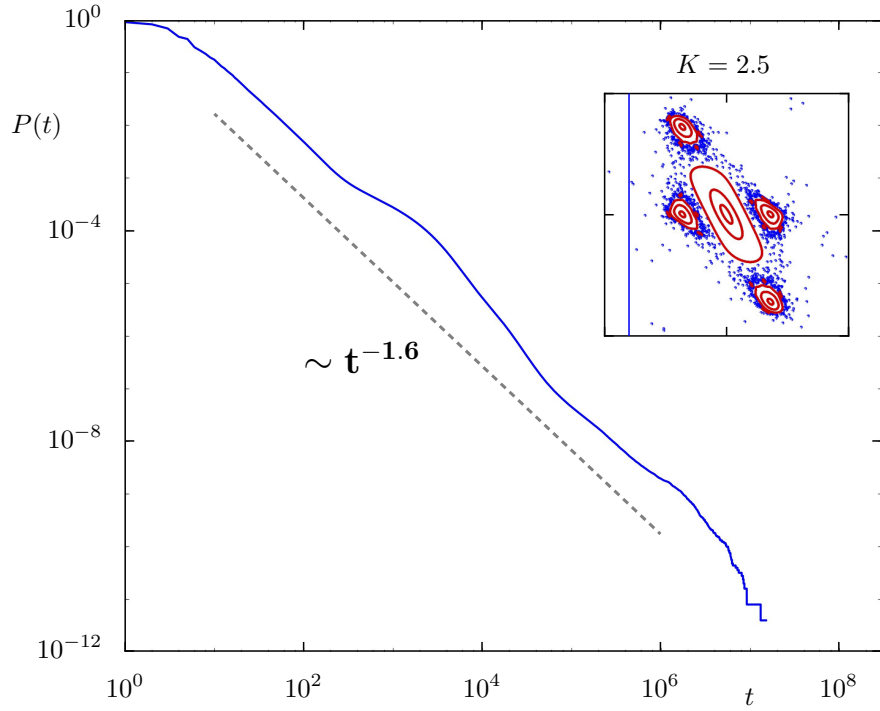
(b) 2D map F_{2D}, $\gamma_{fit} = 1.57$

Figure 5.1: Dependence of statistics of Poincaré recurrences $P(t)$ on time t for (a) the 4D map F_{SC}, see Eq. (2.13), and (b) the 2D map F_{2D}, see Eq. (2.11). For comparison the gray dashed lines represent a power-law $P(t) \sim t^{-\gamma}$, with γ as labeled. The captions of (a) and (b) contain the exponent γ_{fit} obtained by fitting. The insets sketch the position of the initial region Γ (blue box) with regular tori (red) and a trapped orbit (blue). The insets show (a) a phase-space section $|p_2| < 10^{-5}$, see Section 3.1 and (b) the 2D phase space.

5.2 Observations of trapping in phase space

In order to reveal the mechanism of trapping in the 4D case further investigations are required. Therefore more trapped orbits are computed in the same manner as described in Section 5.1 using higher grid resolutions. For the strongly coupled map F_{SC} about $1.9 \cdot 10^{12}$ initial points are iterated until their first return. About 10^3 of these initial points lead to orbits with return times $T > 10^6$. The following results are based on this collection of trapped orbits.

In this section first of all the trapped orbits are depicted in phase space, using phase-space sections as described in Section 3.1.3. These images serve as a visual illustration of the trapping.

5.2.1 Gallery of trapped orbits

The collection of trapped orbits, can be classified into distinct groups according to the regular tori at which the orbits are trapped. For this observation the trapped orbits are depicted in 3D phase-space sections $|p_2| < \epsilon$ with $\epsilon = 10^{-4}$, see the blue points in Figures 5.2 and 5.3. Additionally, the regular orbits presented in Section 3.3 are shown with $\epsilon = 10^{-5}$.

According to these plots the orbits get only trapped in few regions close to the groups of regular tori discussed in Section 3.3. The orbits are trapped outside of the regular islands formed by these groups of regular tori. Consequently, the orbits are trapped far away from the 2D manifolds identified in Section 4.3. Furthermore, there is no indication for chaotic points penetrating the regular islands. This is consistent with the observations of reference [10] for weakly coupled standard maps. There the authors conclude that although chaotic orbits can actually access every region of the phase space via the Arnold web, the Arnold diffusion within a regular island is nonexistent or exceedingly slow. Finally, in Figures 5.2 and 5.3 the regions occupied by the chaotic orbits mimic roughly the shape of the regular orbits close to them.

5.2.2 Close up on gallery

The general observations of Section 5.2.1 for the different classes of trapped orbits are now completed by a detailed look on one generic representative, namely the orbit shown in Figure 5.2(d). This orbit is trapped around the structure of the horse-shoe.

In order to discuss the spatial relation between the trapped orbit and the regular tori as visible in the phase-space section, locally defined directions have to be introduced. These directions are sketched in Figure 5.4, where four tori are shown as red ellipses with
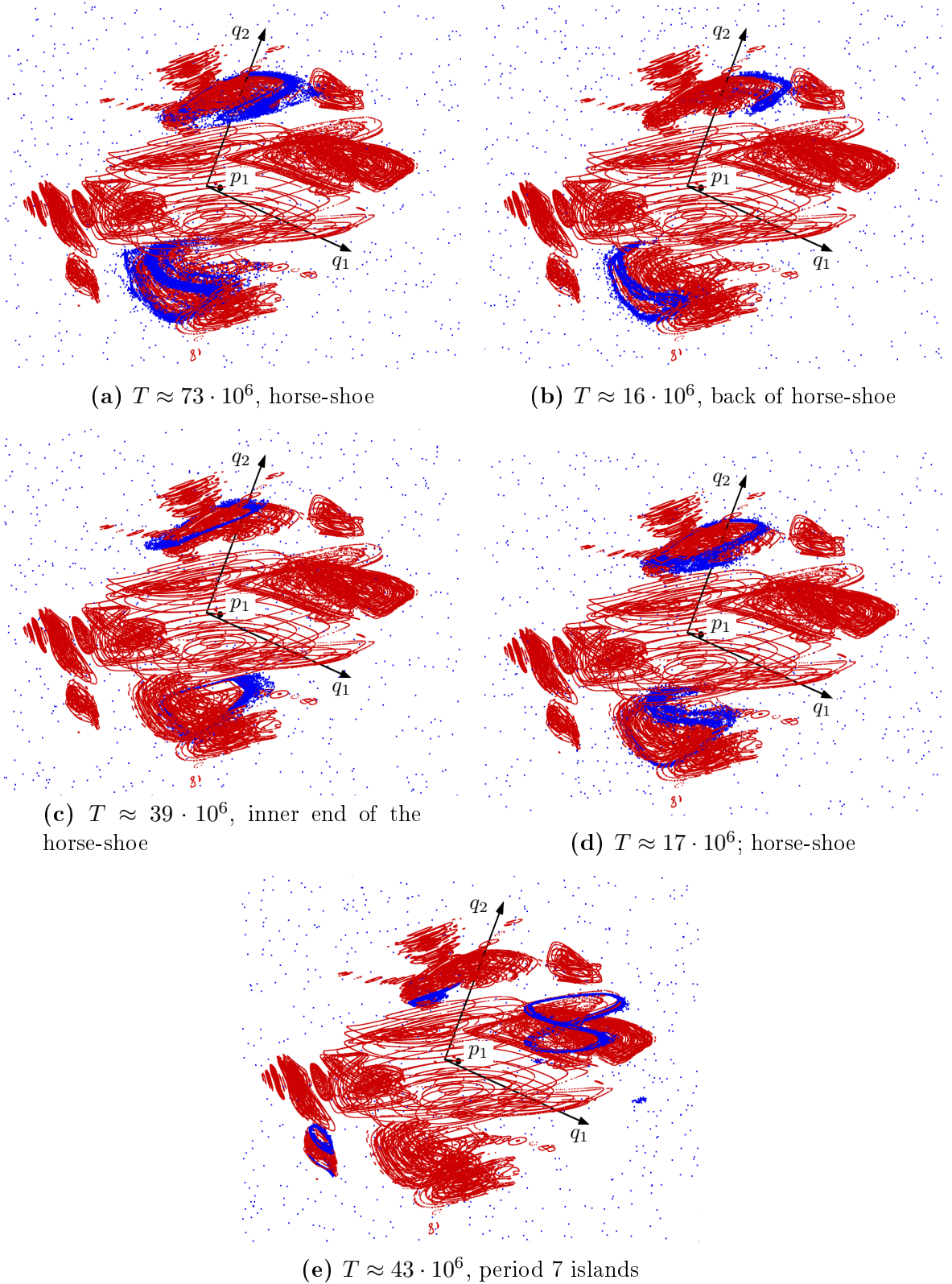
(a) $T \approx 73 \cdot 10^6$, horse-shoe

(b) $T \approx 16 \cdot 10^6$, back of horse-shoe

(c) $T \approx 39 \cdot 10^6$, inner end of the horse-shoe

(d) $T \approx 17 \cdot 10^6$; horse-shoe

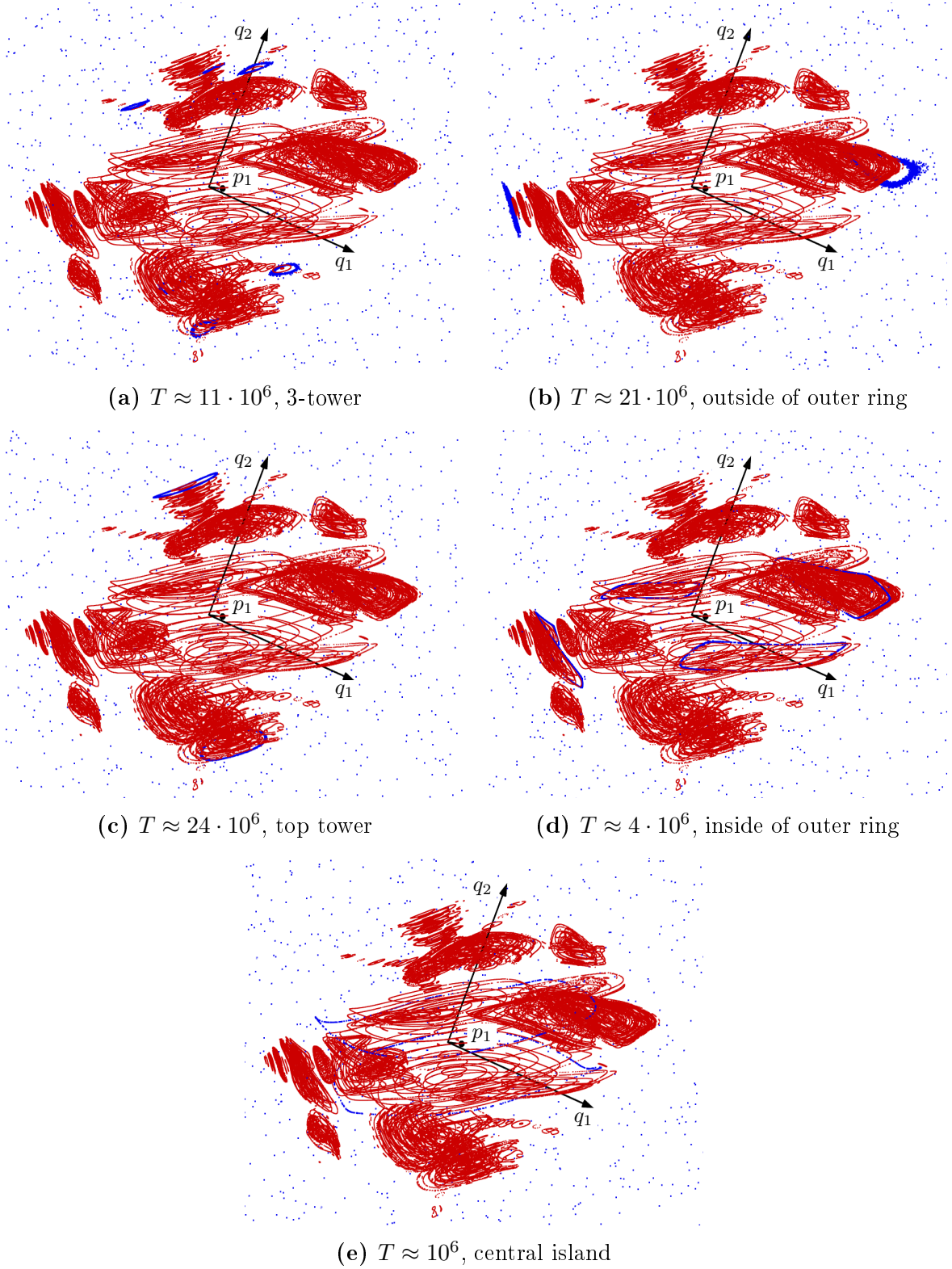(e) $T \approx 43 \cdot 10^6$, period 7 islands

Figure 5.2: Examples for trapped orbits of the 4D map F_{SC}, see Eq. (2.13). Shown is the section $|p_2| < \epsilon$, with regular tori (red, $\epsilon = 10^{-5}$) and an example of a trapped orbit (blue, $\epsilon = 10^{-4}$), that was additionally mapped $2 \cdot 10^7$ iterations backward to illustrate of the chaotic sea. The captions contain the time T till the first return and the structure at which the orbit is trapped, according to the notation introduced in Section 3.3. (see also Figure 5.3)

(a) $T \approx 11 \cdot 10^6$, 3-tower

(b) $T \approx 21 \cdot 10^6$, outside of outer ring

(c) $T \approx 24 \cdot 10^6$, top tower

(d) $T \approx 4 \cdot 10^6$, inside of outer ring

(e) $T \approx 10^6$, central island

Figure 5.3: Examples for trapped orbits of the 4D map F_{SC}, see Eq. (2.13). Shown is the section $|p_2| < \epsilon$, with regular tori (red, $\epsilon = 10^{-5}$) and an example of a trapped orbit (blue, $\epsilon = 10^{-4}$), that was additionally mapped $2 \cdot 10^7$ iterations backward to illustrate of the chaotic sea. The captions contain the time T till the first return and the structure at which the orbit is trapped, according to the notation introduced in Section 3.3. (see also Figure 5.2)
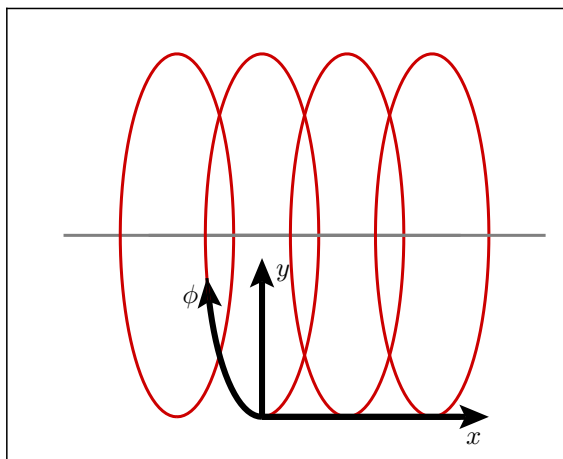
Figure 5.4: Definition of local directions in phase-space section. Four regular tori (red ellipses) with their center line (gray line), see Section 4.1, are schematically shown in the phase-space section. At one torus the directions along the tori (x arrow), perpendicular to the tori (y arrow), and around the tori (ϕ arrow) are indicated.

their gray center line. Firstly, there is the direction ϕ *around the tori*, following the red lines representing the regular tori. Secondly, there is the direction x *along the tori*, which is perpendicular to the lines of the tori, pointing from one torus to its next neighbor. Finally, there is the direction y *perpendicular to the tori*, pointing away or towards the center line and being perpendicular to the other two directions. Considering a particular torus and its action–angle coordinates, the direction around the tori corresponds to the local base vectors of the angles $\{e_{\Theta_i}(\boldsymbol{\Theta}, \boldsymbol{I})\}_{i=1,2}$ on the torus, that is $\phi = \phi(\Theta_1, \Theta_2)$. Note that these two directions appear as one in the phase-space section, as seen in Figure 3.3. Consequently, the other two directions are linear combinations of the local base vectors $\{e_{I_i}(\boldsymbol{\Theta}, \boldsymbol{I})\}_{i=1,2}$ of the actions, that is $x = x(I_1, I_2)$ and $y = y(I_1, I_2)$. The following discussions always refer to the introduced directions.

Figure 5.5(a) shows a close-up of the upper horse-shoe with the chosen trapped orbit. The trapped orbit is located in a thin layer wrapping around the horse-shoe. *Thin* refers to the extension in the direction perpendicular to the tori, whereas the extension along the tori is much bigger. In fact the trapped orbit is confined to such a thin layer, that it looks like a 2D object in the section. According to the discussion of dimensions in the phase-space section, see Section 3.1.3, the orbit is expected to be confined to a 3D region of the 4D phase space. The other examples in Figures 5.2 and 5.3 share this property, some of them even looking like a 1D object in the section of the phase space, see e.g., Figure 5.3(d)), which would result from a 2D object in the phase space. This is surprising, since in a 2D phase space chaotic orbits are trapped in 2D areas between partial barriers, see e.g., Figure 5.5(c), so the dimension of the trapped orbits
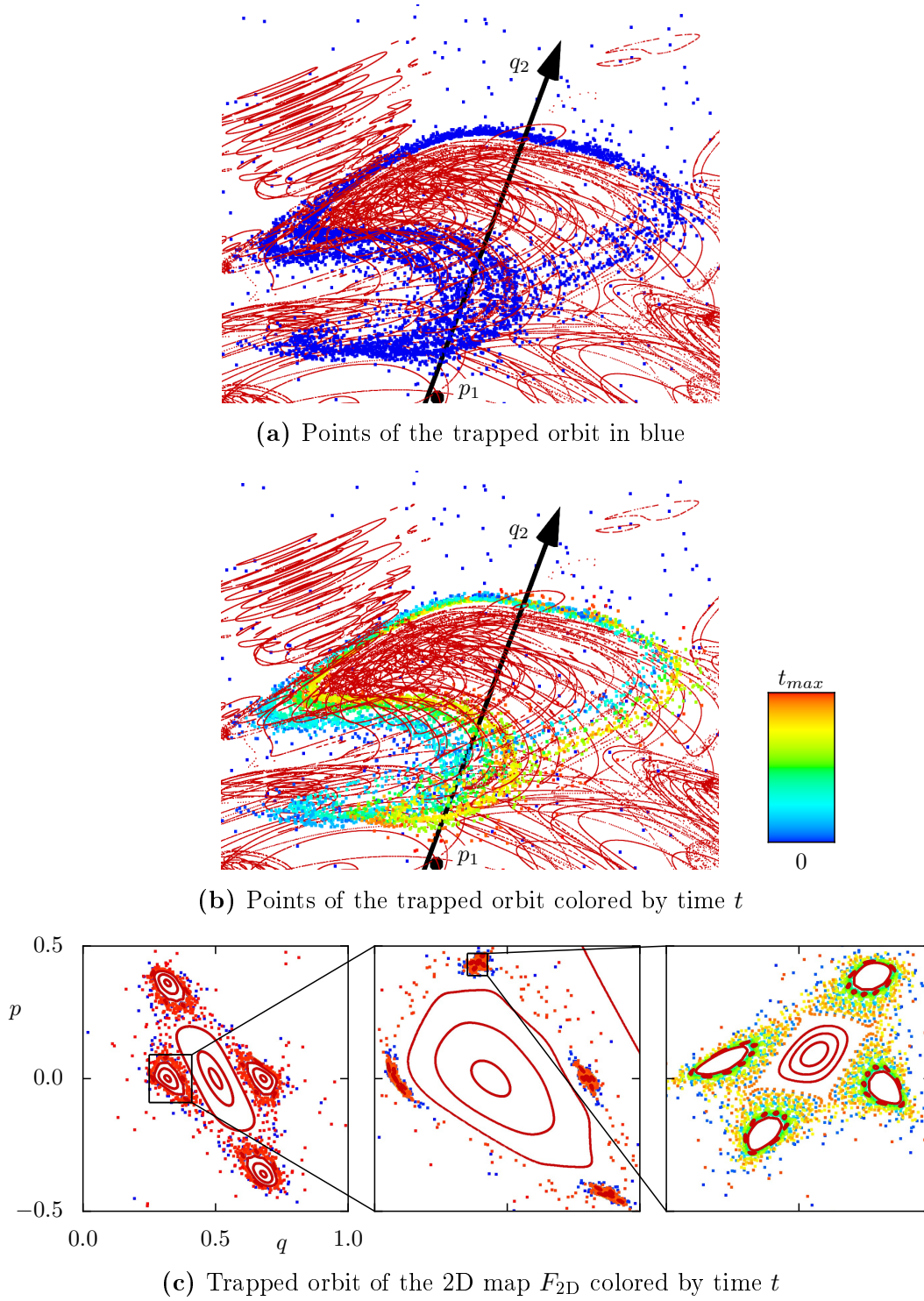
(a) Points of the trapped orbit in blue

(b) Points of the trapped orbit colored by time t

(c) Trapped orbit of the 2D map F_{2D} colored by time t

Figure 5.5: Close-up on the trapped orbit shown in Figure 5.2(d). (a) and (b) show a phase space section with parameters as in Figure 5.2, regular tori (red) and the trapped orbit (blue in (a) and colored according to the time t of the points in (b)). For comparison the trapped orbit from Figure 2.1 of the 2D map F_{2D}, colored in the same manner, is opposed in (c)

is expected to match the dimension of phase space. In order to quantify this observation an analysis of the fractal dimensions of the orbits is presented in appendix A.1, which concludes that the trapped orbits are at least very confined in one dimension.

For the next step of the qualitative analysis the points of the trapped orbit shown in Figure 5.5(a) are colored according to their time t, as mentioned in Section 3.1.3. The result is depicted in Figure 5.5(b). The different colors form fairly separated bands in the thin layer in which the trapped orbit is located. Note that if the orbit was mapped randomly within the thin layer all colors would appear to be mixed. The bands are aligned around the horse-shoe and match roughly the shape of the red lines of the regular tori. Also considering the proximity to the regular tori, this suggests that the mapping of the orbit around the tori mimics the mapping on the regular tori closest to the orbit. The fact that the colors of the bands are separated along the tori means that the trapped orbit propagates slower in that direction than around the tori. Accordingly, the above mentioned confinement of the layer perpendicular to the tori can be reinterpreted as the consequence of an even slower propagation in that direction. Additionally, adjacent colors in phase space are also adjacent in the colormap representing the time t. This indicates that the orbit propagates along the tori continuously. The described arrangement of the colors of the trapped orbit in Figure 5.5(b) completely differs from the structure of a trapped orbit in a hierarchy of the 2D map F_{2D}, as illustrated in Figure 5.5(c). There the points are distributed around several unconnected regular islands and in each part of this hierarchy two colors are present, indicating that the orbit visits every area twice, namely when it propagates into the hierarchy and on its way out.

In conclusion, the different character of the trapping in the 4D phase space compared to the one in the 2D phase space suggests a different trapping mechanism, which is not based on a hierarchical structure. Instead, the trapping of orbits manifests by a slow propagation along the tori and an even slower perpendicular to them. In order to investigate these propagations, first of all the introduced directions have to be justified or rather stated more precisely. Only then the character of the propagation can be quantified regarding features like diffusion or drift. It is quite complicated to access information about the propagation of the trapped orbit in phase space due to both the high dimensionality of the phase space and the choice of locally defined directions. Hence, the preferred space for these investigations is not the phase space but the frequency space, as introduced in Section 3.2. The reason is that in the 2D frequency space every torus is represented by a point. That is, the "fast" motion around the tori, corresponding to the angle coordinates (Θ_1, Θ_2) on each torus, is no longer visualized. Thus, only the directions along and perpendicular to the tori, which are of interest here,

remain.

5.3 Sticky region in frequency space

In this section the sticky region of the 4D phase space is examined in frequency space. As discussed in Sections 2.4 and 2.6, the sticky region in which orbits are trapped corresponds to a vicinity of the boundary of the regular islands. The properties of the sticky region and its origin is important for the understanding of the trapping mechanism. For example the propagation of an orbit within the sticky region or how it enters or exits the region is of interest.

Firstly, the observations of trapping in phase and frequency space are compared in Section 5.3.1. The frequency space is found suitable for the investigation of trapped orbits. Hence, the sticky region is presented in frequency space and its properties are discussed in Section 5.3.2.

5.3.1 Trapped orbit in frequency space

First of all the trapping is observed in frequency space completing the examinations in phase space in Section 5.2.2. For this purpose the orbit from Figure 5.5(b) is displayed in frequency space. Additionally to this trapped orbit 1400 regular orbits in the horse-shoe are calculated to relate the position of the trapped orbit to the regular tori. The mapping to frequency space is done according to Section 3.2.3.

The results in frequency space are depicted in Figure 5.6, which nicely illustrate the relation between phase and frequency space. The regular tori, which appear as lines in the phase-space section, are projected to points in frequency space. Consequently the direction around the tori, as discussed in Section 5.2.2, is no longer visible. On the contrary, the arrangement of the colors of the trapped orbit in phase and frequency space demonstrates that the directions along and perpendicular to the tori are still present in the frequency space. E.g., the sequence of colors from blue to yellow along the tori in phase space corresponds to the sequence in frequency space going approximately from the top right to the lower left. As asserted in Section 5.2.2 on a torus these directions are linear combinations of the local base vectors $\{\boldsymbol{e}_{I_i}(\boldsymbol{\Theta}, \boldsymbol{I})\}_{i=1,2}$ of the action. On a torus the relation between these directions in phase and frequency space is even available in form of a numerical mapping between the actions $\boldsymbol{I}$ and frequencies $\boldsymbol{\omega}$, as presented in reference [61]. Here it is sufficient to acknowledge the occurrence of the directions along and perpendicular to the tori in frequency space as indicated by the x and y direction in Figure 5.6(b). The correspondence of the x and y directions in phase space and

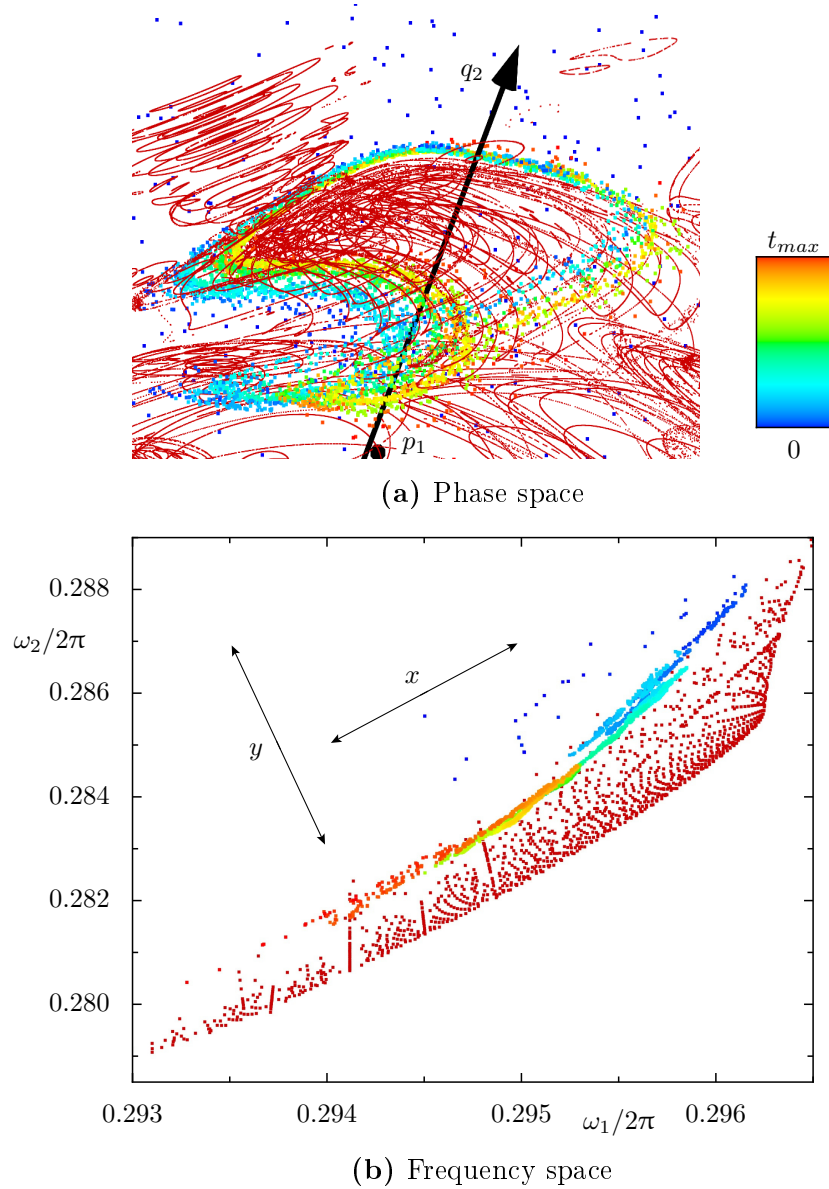**(a)** Phase space

(b) Frequency space

Figure 5.6: Trapped orbit of Figure 5.5(b), trapped around the horse-shoe, (a) in phase space as shown in Figure 5.5(b) and (b) in frequency space. Shown are regular tori (red) and the trapped orbit (colored according to the time t of the points). (b) The arrow labeled x indicates the direction along the tori and the arrow labeled y the direction perpendicular to the tori. Note that according to Sections 3.3 and 4.3 the lower edge of the regular tori in frequency space corresponds to a center manifold.

frequency space allows for relating the transport in frequency space to the transport in phase space.

In Figure 5.6(b), the colors of the function $\boldsymbol{\omega}(t)$ representing the trapped orbit form bands. They are extended much more along the tori than perpendicular to them, thus reproducing the discussion of Figure 5.5(b). In contrast, in frequency space even a propagation of the orbit perpendicular to the regular tori is observable. This is indicated, e.g., by the blue or green colored bands at the right, that are clearly located at different distances from the tori. These observations confirm that the frequency space is adequate to examine the propagation of trapped orbits, as is suspected in Section 5.2.2.

5.3.2 Initial points in sticky region

In this section the sticky region is discussed in frequency space. This region can be visualized by orbits, which are trapped in it. Thus, in order to investigate the sticky region it is necessary to obtain many of such trapped orbits. For this the coordinates of orbits, which are trapped around the horse-shoe, are slightly varied. By these initial points are found that lie within the sticky region. These initial points are iterated backwards and forwards in time until they either visit the region Γ defined in Section 5.1 or the time t exceeds a threshold of $T = 5 \cdot 10^7$. The region Γ serves as an exit condition ensuring, that the orbit escaped the sticky region.

In Figure 5.7 the results for 400 initial points, which are within the sticky region and close to each other, is depicted. The backward and forward iteration of each initial point are concatenated to one orbit. For each orbit the same color map indicating the time t with respect to the total length of the orbit is used. For comparison also the same regular tori as in Figure 5.6(b) are depicted.

In Figure 5.7 the colored points of the trapped orbits demonstrate the extension of the sticky region. This is due to the fact that the frequency analysis only works for chaotic orbits close to regular tori. When a chaotic orbit exits the sticky region the frequencies obtained for it change rapidly and become random. Besides this, the colors of the orbits allow no statement about the average position of an orbit after a certain time, since all the orbits shown in Figure 5.7 have different lengths. Instead, the colors demonstrate the propagation within the sticky region. Close to the regular tori the orbits form thin, colored bands, that are stacked on top of each other. This observation confirms that the propagation speed along the regular tori is larger than perpendicular to them, as already concluded in Sections 5.2.2 and 5.3.1. In contrast to these sections, here the conclusion is based on the propagation of many trapped orbits in a large part of the sticky region. In addition, the character of the propagation seems to alter at a
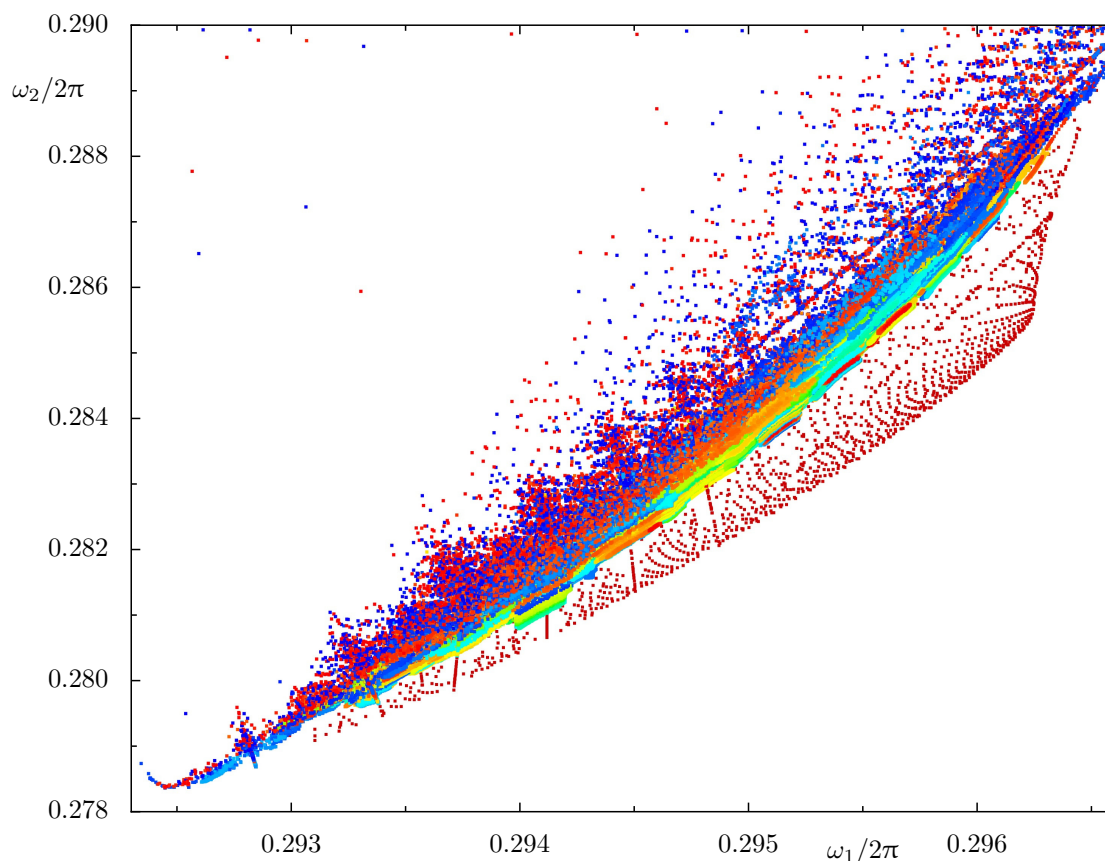
Figure 5.7: Trapped orbits around the horse-shoe in frequency space. Each of 400 initial points, located within the sticky region and close to each other, is iterated backward and forward in time t and then concatenated to one trapped orbit. The trapped orbits are shown (all colored according to the time t of the points, as shown for one orbit in Figure 5.6(b)) and for comparison the regular tori (red) shown in Figure 5.6.

certain distance from the regular tori, where the shape of the bands rapidly changes to an area with apparently isotropically distributed colors. Furthermore, the colors in this area are majorly blue or red, indicating that for both the backward and forward iteration the orbit escapes the sticky region through this area.

Also visible in Figure 5.7 are line-shaped disturbances, that cross the thin colored bands, indicating the influence of resonances. In order to illustrate this the trapped orbits and a selection of resonance lines are shown in Figure 5.8. Almost all relevant resonances emanate from one of the three points with $\omega_1 = \omega_2 = 7/24$, $5/17$, $13/44$ such that their intersections form a periodic pattern, which is visible in the zoom box of Figure 5.8. Such a pattern is also observed by Richter [58]. The different resonances seem to differ in their effect on the orbits. Some are even visible in the regular region, whereas others are hardly seen in the much better resolved sticky region. Most resonances attract points close to them, some bend the colored bands locally. Nevertheless,
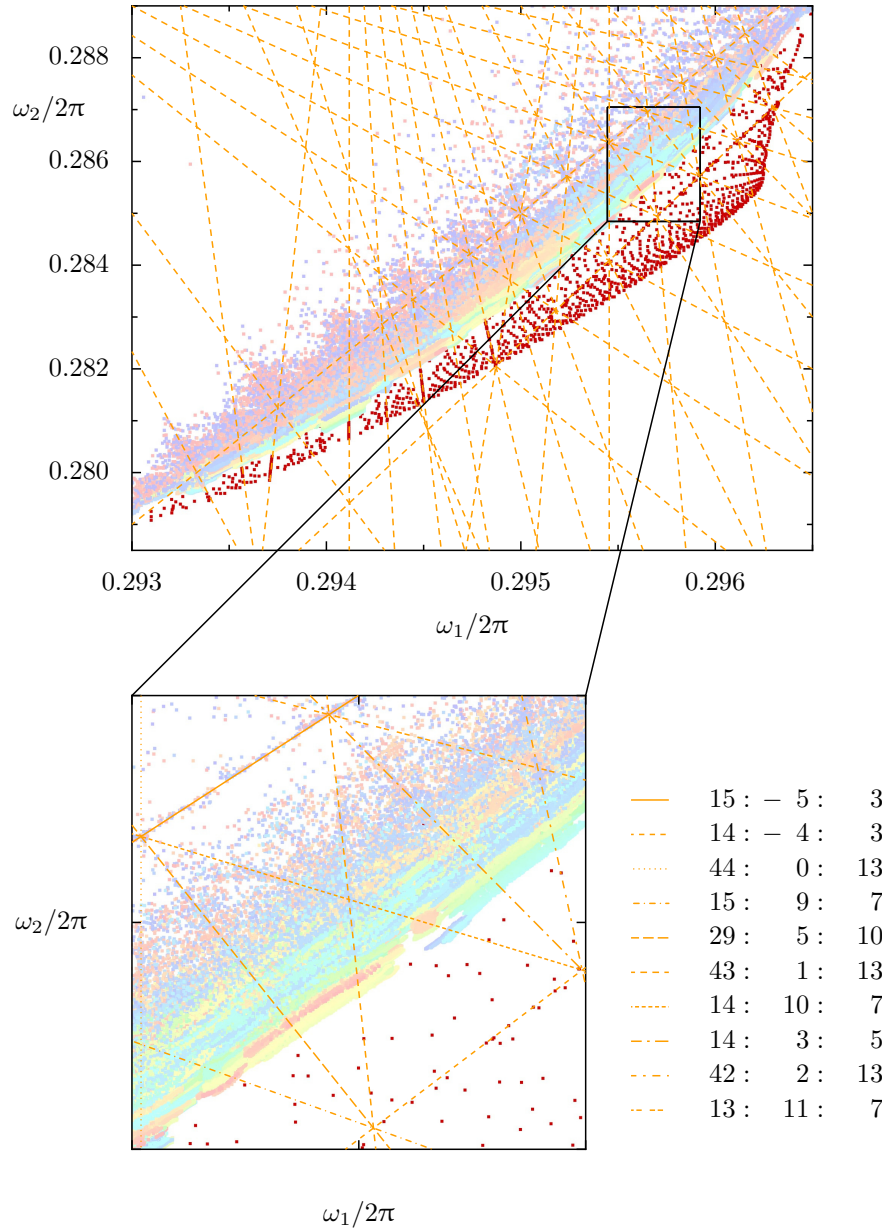
Figure 5.8: Resonance lines as visible by the distortions of the trapped orbits in frequency space. The resonances (orange lines) are shown and for comparison the regular tori (red) and the trapped orbits (bright colors), also shown in Figure 5.7. The zoom box shows a part of the characteristic pattern of the resonances with the according coefficients, another zoom is depicted, e.g., in the first picture of Figure 5.16. Note that almost all found resonances intersect on the resonance $1 : -1 : 0$, where $\omega_1 = \omega_2$, in one of the three points $7/24$, $5/17$, $13/44$.

the bands exist beyond the resonance lines, thus orbits propagate across them. This influence of the resonances agrees with the statements about transport in resonance zones, see Section 2.6.2. In these terms the situation can be viewed as the following. The many resonance zones overlap such that the chaotic orbits can propagate fast perpendicular to the resonances and slowly via Arnold diffusion along them. However, the trapping processes suggested in Section 2.6.2 are based on irrational tori surrounding the resonance zones and intersections of resonances. But the sticky region seen in Figure 5.8 is only confined in one direction by regular tori and is still present relatively far away from these tori. Likewise, the sticky region contains only a few intersections of resonances. Therefore, it is unlikely that the conjectured trapping mechanisms can explain the observed sticky region.

As observed in the phase-space section, see Section 5.2.1, the regular tori and trapped orbits occupy different regions in frequency space, although the trapped orbits get very close to the regular tori. The few regular points that violate this statement turn out to be rather chaotic, when viewed in phase space. Some of the trapped orbits that get very close to the tori appear to be trapped for very large times in very confined regions. The regions are of the size $\triangle\omega_{1,2}/2\pi \sim 10^{-5}\ldots 10^{-7}$ and sometimes on resonance lines, but far away from intersections of resonance lines. The orbits are trapped for times $t > 10^7$, that is after they entered the region they do not leave before the threshold time $T = 5 \cdot 10^7$. This behavior reminds of trapping in 2D systems, where chaotic orbits are trapped for long times in the vicinity of islands chains, hence possess the frequency of the island chain. However, here this behavior is observed very rarely and might result from generalized partial barriers, see Section 2.6.1.

5.4 Investigation of trapping in frequency space

The sticky region and the transport within it are qualitatively discussed in Section 5.3.2. Some of the properties of the sticky region are examined closer in this section. Therefore, Gaussian ensembles of initial conditions are started within the sticky region and different statistics for the resulting orbits are considered. The setup of the Gaussian ensembles is explained in Section 5.4.1. Then, in Section 5.4.2 the survival times of the orbits are presented and in Section 5.4.3 the time dependence of variance and mean of the Gaussian ensembles. Motivated by these statistics the general diffusion character within the sticky region is evaluated in Section 5.4.4.

At present not all aspects of the statistics can be put in context with an underlying trapping mechanisms. Rather the results are presented such that they can form the basis of future studies of trapping in 4D systems. Also some properties of the sticky

region remain to be examined such as the exit and entry to the sticky region.

5.4.1 Gaussian ensembles in sticky region

In order to obtain evidence for the observations made in Section 5.2.2 and Section 5.3 statistical investigations are conducted, that is the propagation of sets of initial points within the sticky region is measured. These initial points are defined in this section.

Firstly, two points in the frequency space are chosen, both within the sticky region at roughly the same position along the regular tori, but one frequency $\boldsymbol{\omega}_{\mathrm{in}}$ close to the regular tori and one $\boldsymbol{\omega}_{\mathrm{out}}$ further away. Secondly, two points in phase space $\boldsymbol{x}_{\mathrm{in}}$, $\boldsymbol{x}_{\mathrm{out}}$ are found, whose initial frequencies match approximately the chosen ones. This is accomplished by a manual search in the (q_1, q_2)-plane, for which $p_1 = p_2 = 0$ and which intersects the horse-shoe. Thirdly, it is assumed that initial points along the vector between $\boldsymbol{x}_{\mathrm{in}}$ and $\boldsymbol{x}_{\mathrm{out}}$ lead to frequencies along the vector between $\boldsymbol{\omega}_{\mathrm{in}}$ and $\boldsymbol{\omega}_{\mathrm{out}}$. Based on this, M rectangles $\diamond_i$ in the (q_1, q_2)-plane can be defined by

$$l_{q_j} \equiv \boldsymbol{e}_{q_j} \cdot (\boldsymbol{x}_{\mathrm{out}} - \boldsymbol{x}_{\mathrm{in}})/M \cdot 0.05$$

$$\mu_{i,q_j} \equiv \boldsymbol{e}_{q_j} \cdot \left(\boldsymbol{x}_{\mathrm{in}} + (\boldsymbol{x}_{\mathrm{out}} - \boldsymbol{x}_{\mathrm{in}}) \cdot \frac{i}{M} \right)$$

$$\diamond_i \equiv \{\boldsymbol{x} \in U : \boldsymbol{e}_{p_j} \cdot \boldsymbol{x} = 0, \boldsymbol{e}_{q_j} \cdot \boldsymbol{x} \in [\mu_{i,q_j} - 0.5 \cdot l_{q_j},\ \mu_{i,q_j} + 0.5 \cdot l_{q_j}]\}$$

with $j \in \{1, 2\}$ and $i \in \mathbb{N}$, $i \in [0, M-1]$. Initial points are defined within these rectangles in phase space. For the following results the initial points are chosen in form of a 2D Gaussian distribution, with mean μ_{i,q_j} and standard deviation σ_{q_j} such that two standard deviations lie within the rectangle, that is $\sigma_{q_j} \equiv l_{q_j} \cdot 0.25$. Note that the investigations are also conducted with initial points distributed on a grid on $\diamond_i$. However, no major difference to the results for the Gaussian distribution can be detected, except for the grid being partially visible in the distribution of the initial frequencies.

The parameters are chosen

$$\boldsymbol{x}_{\mathrm{in}} = (0, 0, 0.5098608, 0.6085289) \qquad \boldsymbol{\omega}_{\mathrm{in}} = (0.294967, 0.283408)$$

$$\boldsymbol{x}_{\mathrm{out}} = (0, 0, 0.5106008, 0.61115498) \qquad \boldsymbol{\omega}_{\mathrm{out}} = (0.294922, 0.283762)$$

and $M = 10$ ensembles with 400 initial points per ensemble except for the evaluation of the survival times, see Section 5.4.2, where $M = 15$ ensembles with 10^4 initial points per ensemble, are used. Note that for this choice of $\boldsymbol{x}_{\mathrm{in}}$ and $\boldsymbol{x}_{\mathrm{out}}$ the resulting rectangles $\diamond_i$ in the (q_1, q_2)-plane have an aspect ratio of roughly $1 : 4$.
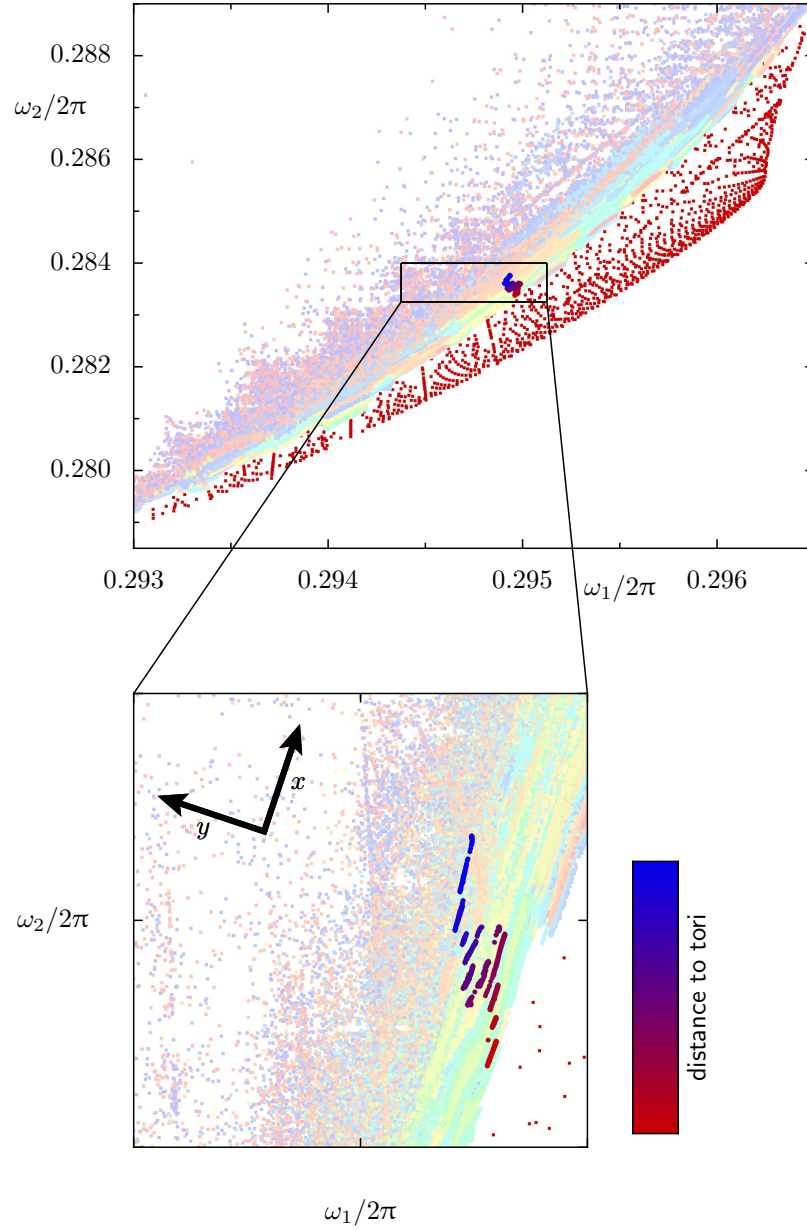
Figure 5.9: Position of Gaussian ensembles of initial points around the horse-shoe in frequency space. The Gaussian ensembles (groups of points in the zoom box colored accordingly to their distance to the regular tori, with red indicating the closest ensemble and blue the most distant) are shown and for comparison the regular tori (red) and the trapped orbits (bright colors), also shown in Figure 5.7. The zoom box indicates the position and arrangement of the ensembles. The new coordinates (x, y) are indicated by black arrows, that is the point of origin is shifted along the direction x to be visible in the zoom box.

(a) $M = 10$, $m = 400$ **(b)** $M = 15$, $m = 10^4$
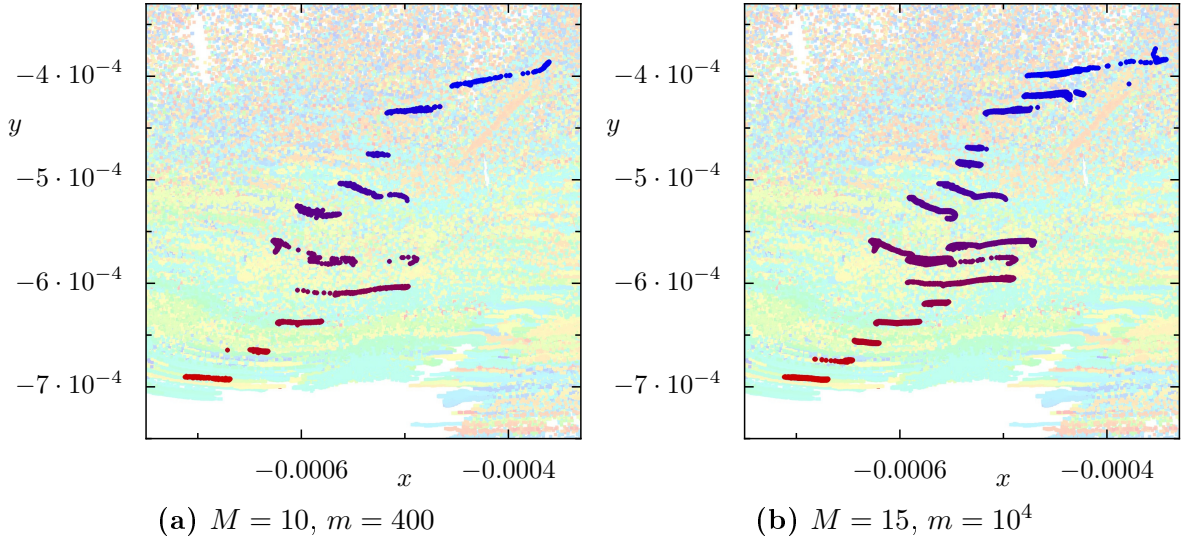
Figure 5.10: Gaussian ensembles of initial points around the horse-shoe expressed in new coordinates (x, y) as indicated in Figure 5.9. The Gaussian ensembles (groups of points in the zoom box colored accordingly to their distance to the regular tori, with red indicating the closest ensemble and blue the most distant) are shown and for comparison the trapped orbits (bright colors), also shown in Figure 5.7. (a) and (b) represent the two considered sets of ensembles with different numbers of ensembles M and initial points per ensemble m.

The initial points are iterated as in Section 5.3.2, that is backward and forward in time until a point is either mapped to the initial region Γ also used for the Poincaré recurrence statistics in Section 5.1 or the number of iterations exceeds a threshold of $5 \cdot 10^7$. For the evaluation of the survival times this threshold is raised to $15 \cdot 10^7$ and the points are only mapped forward in time.

The chaotic orbits are then transformed to frequency space, as described in Section 3.2.3. In order to transfer the results in terms of the local directions *along* and *perpendicular to the tori*, used in Section 5.2.2 and Section 5.3, a different set of coordinates (x, y) in frequency space is chosen, which represents the two directions at least in the vicinity of the started Gaussian ensembles. The $15 : -5 : 3$ resonance is used for this purpose as the x direction, along the tori, and its orthogonal vector is used as the y direction, perpendicular to the tori. As point of origin $(28/95, 27/95)$ is chosen, which is the intersection between the $15 : -5 : 3$ and the $17 : 7 : 7$ resonance. The transformation to (x, y) corresponds to a rotation and shift of the original frequency space coordinates (ω_1, ω_2), thus all scales are conserved. But for simplicity the new coordinates are rescaled by 2π, which corresponds to a normalization of the frequencies $\boldsymbol{\omega}$ to the interval $[0, 1)$. The coordinate axes and the position of the initial ensembles in frequency space are sketched in Figure 5.9. The distance of the Gaussian ensembles

is indicated by a red to blue color map, where the closest ensemble is red and the most distant blue. The initial ensembles are also depicted in the new coordinate system in Figure 5.10(a) and Figure 5.10(b). Note that the ensembles are much more extended along the tori in the frequency space than perpendicular to them.

Different aspects of the propagation of the ensembles of this setup in frequency space are presented in the following sections. The Gaussian ensembles depicted in Figure 5.10(a) are used in Section 5.4.3 and Section 5.4.4, the ones depicted in Figure 5.10(b) are used in Section 5.4.2.

5.4.2 Survival time statistics

First the setup described in Section 5.4.1 is used to examine the statistics of survival times, see Section 2.2, for the sticky region around the horse-shoe. Therefore, the initial points of the fifteen Gaussian ensembles, visualized in frequency space in Figure 5.10(b), are mapped forward until a point is either mapped to the region Γ also used for the Poincaré recurrence statistics in Section 5.1 or the number of iterations exceeds a threshold of $5 \cdot 10^7$. The time t at which an orbit firstly enters the region Γ represents here the survival time in the sticky region, see Section 2.2. The resulting statistics $S(t)$ of these survival times t is depicted in Figure 5.11 for all the used Gaussian ensembles. The colors indicate the distance of the initial Gaussian ensemble to the tori, as seen in Figure 5.9.

According to Figure 5.11 the survival time statistics $S(t)$ for a certain t are larger the closer the corresponding Gaussian ensemble is located to the regular tori. For each ensemble $S(t)$ exhibits a power-law behavior, $S(t) \sim t^{-\gamma}$, with roughly the same exponent $\gamma = 1.2$, starting at some time $t_{\min}$ and being present for all considered times $t > t_{\min}$. The time $t_{\min}$ for a certain statistics $S(t)$ is larger the closer the corresponding Gaussian ensemble is located to the regular tori. This implies that the power-law becomes relevant at later times for points that are closer to the regular tori.

Note that the setup for the survival times $S(t)$ here differs from the typical setup found in the literature. There the initial region for the statistics $S(t)$ is usually the complement of the initial region Γ used for the Poincaré recurrences $P(t)$. In this case, the exponent γ for the power-law of $S(t)$ is by one smaller than the exponent for $P(t)$ [7].

5.4.3 Variances and means

The setup described in Section 5.4.1 is used to examine the time dependencies of the variances (σ_x^2, σ_y^2) and means $(\bar{x}, \bar{y})$ of the Gaussian ensembles in frequency space with respect to the coordinates (x, y) defined in that section. Therefore, the variances and
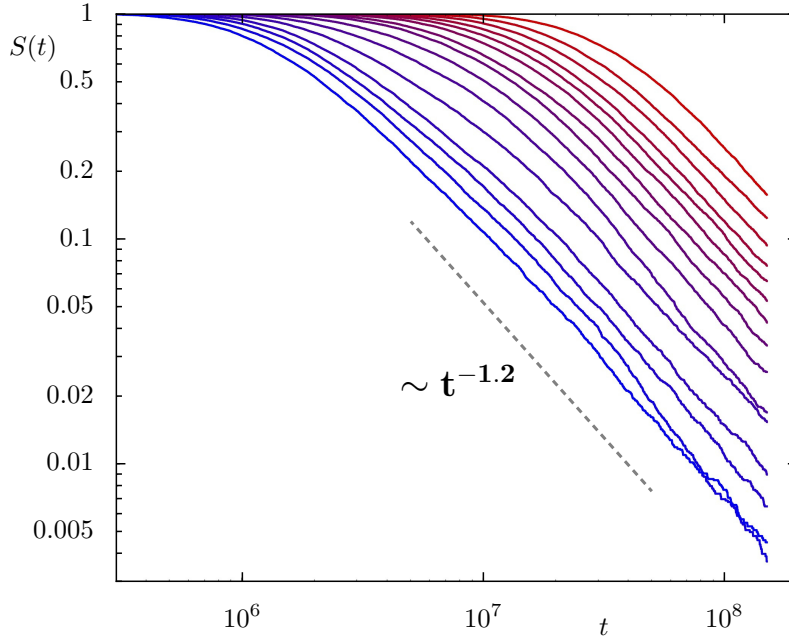
Figure 5.11: Dependence of statistics of survival times $S(t)$ on time t for Gaussian ensembles of initial points around the horse-shoe as described in Section 5.4.1 and shown in Figure 5.10(b). The graphs are colored accordingly to the distance of the corresponding ensemble to the regular tori (red - closest, blue - most distant), as shown in Figure 5.9. For comparison the gray dashed line represents a power-law $S(t) \sim t^{-\gamma}$ with $\gamma = 1.2$.

means of each ensemble are calculated for all times until the first point of the ensemble escapes to Γ.

The time dependencies are shown for the variances in Figure 5.12 and for the means in Figure 5.13. The colors indicate the distance of the initial Gaussian ensemble to the tori, as seen in Figure 5.9. The results for the iteration backwards in time are shown with bright colors.

In Figure 5.12 the variances in both coordinates appear to be very similar for the backward and forward iteration. However, the variance $\sigma_x^2(t)$ in the x direction, that is along the tori, is about hundred times larger than the variance $\sigma_y^2(t)$ in the y direction, that is perpendicular to the tori,

$$\frac{\sigma_x(t)}{\sigma_y(t)} \approx 100 \quad \forall t \in [-5 \cdot 10^7, 5 \cdot 10^7].$$

This means that the expansion of the Gaussian ensembles is much larger along the tori than perpendicular to them in the frequency space. Note that according to Section 5.4.1 the original variances in the (q_1, q_2)-plane in phase space only have a ratio of at most $1:4$. The variances of the different Gaussian ensembles for one direction are at larger
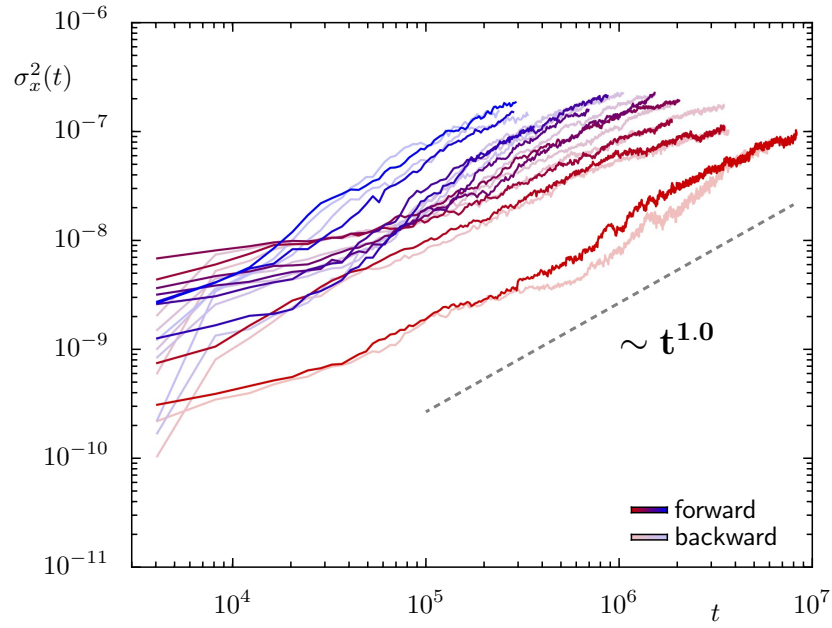
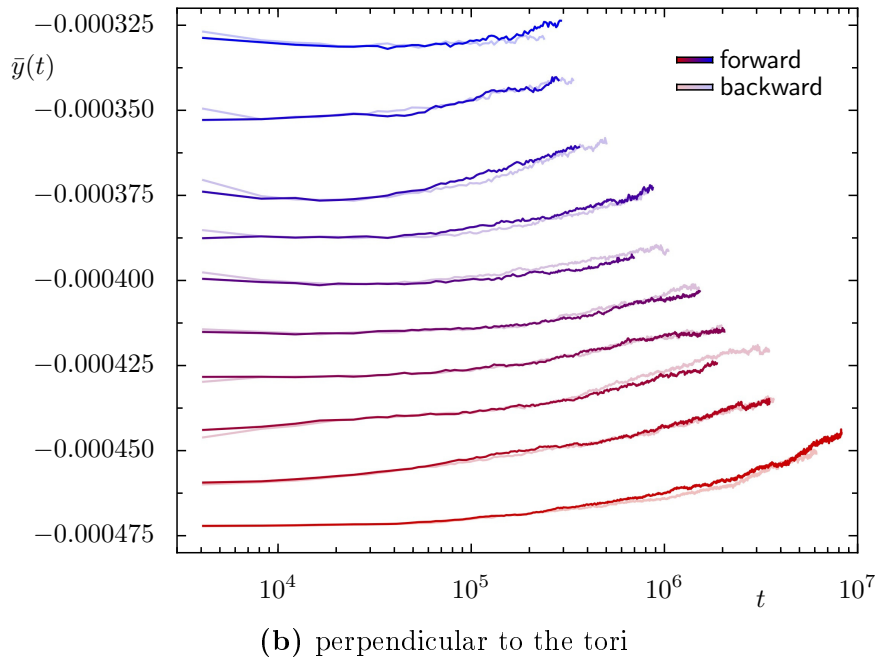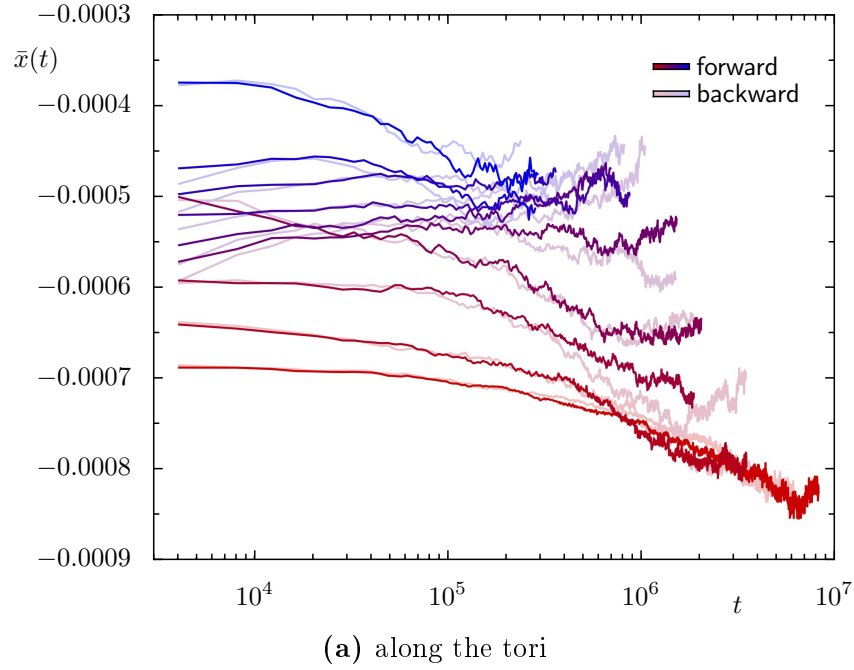**(a)** along the tori
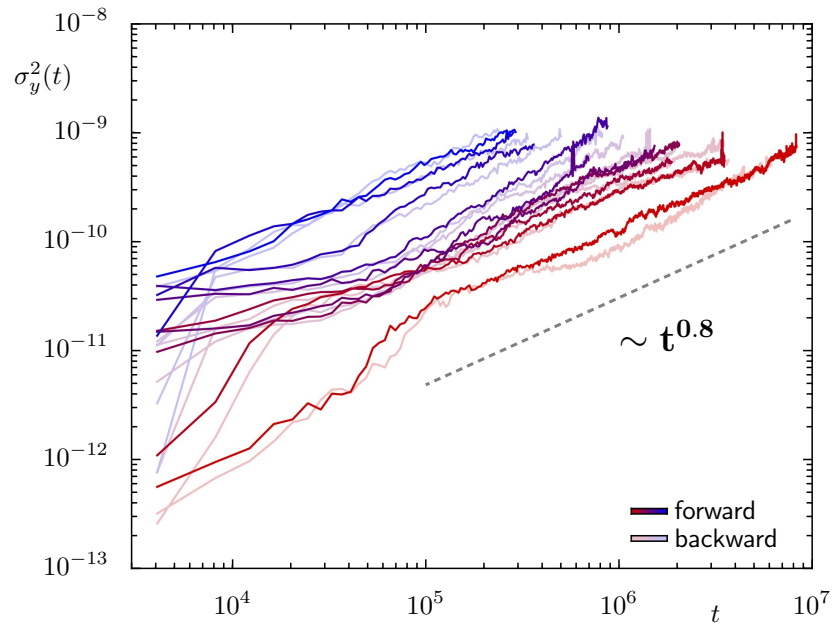
(b) perpendicular to the tori

Figure 5.12: Dependence of the variances $\sigma_i^2(t)$ on time t of Gaussian ensembles of initial points around the horse-shoe as described in Section 5.4.1 and shown in Figure 5.10(a). The graphs are colored accordingly to the distance of the corresponding ensemble to the regular tori (red - closest, blue - most distant, dark - forward mapping $t > 0$), as shown in Figure 5.9). The results for both for- and backward mapping are inserted (bright - backward mapping $t < 0$ projected to absolute value $|t|$). The gray dashed lines represent the power law $\sigma_i^2(t) \sim t^{-\gamma_i}$ with (a) $\gamma_x = 1.0$ and (b) $\gamma_y = 0.8$ and are included for comparison.

(a) along the tori

(b) perpendicular to the tori

Figure 5.13: Dependence of the means $(\bar{x}(t), \bar{y}(t))$ on time t of Gaussian ensembles of initial points around the horse-shoeas described in Section 5.4.1 and shown in Figure 5.10(a). The graphs are colored accordingly to the distance of the corresponding ensemble to the regular tori (red - closest, blue - most distant, dark - forward mapping $t > 0$), as shown in Figure 5.9). The results for both for- and backward mapping are inserted (bright - backward mapping $t < 0$ projected to absolute value $|t|$).

times roughly ordered by the distance of the ensembles to the regular tori, with closer ensembles having smaller variances. The closest and most distant ensembles presented here differ in the magnitude of their variances by a factor of roughly ten for both directions. This implies that the spreading of a Gaussian ensemble is the slower the closer it is to the tori. Furthermore, in both directions the variances exhibit a power-law behavior $\sigma_i^2(t) \sim t^{-\gamma_i}$ with roughly the same exponent γ_i for all Gaussian ensembles. The exponent γ_x is one, meaning diffusion along the tori, whereas the exponent γ_y is about 0.8, meaning subdiffusion perpendicular to the tori.

In Figure 5.12 the means in both coordinates appear to be even more alike for the backward and forward iteration, than they are for the variances. Apart from that, small changes of the means for all Gaussian ensembles are visible in both coordinates. More precisely there is a drift away from the tori, indicated by an increase of $\bar{y}$ over time, and a drift to the pointy end of the horse-shoe in frequency space, indicated by a decrease of $\bar{x}$ over time. The drift velocity $\mathrm{d}\bar{x}(t)/\mathrm{d}t$ of the latter is found to be on average roughly ten times larger than the drift velocity $\mathrm{d}\bar{y}(t)/\mathrm{d}t$ of the former. The drift in the x direction seems to be not present for some of the outer Gaussian ensembles for which $\bar{x}(t)$ is rather slightly oscillating. This behavior could be related to the vicinity of these ensembles to the resonance junction $\boldsymbol{\omega} = (105/356, 101/356)$ of the resonances $17:7:7$, $63:5:20$ and $46:-2:13$, see, e.g., the first picture of Figure 5.16. The influence of resonance junctions is discussed in Section 2.6.2. However, the relevance of the observed drifts must not be overestimated. Due to the small number of points per ensemble and the confined time considered here, the drift to smaller values of x could result from a temporal behavior of some particular orbits. Since the coordinates (x, y) only locally approximate the directions along and perpendicular to the regular tori in frequency space, the slight change of $\bar{y}(t)$ could also be caused by such particular orbits, propagating fast to the left point end of the horse-shoe, rather than by a drift away from the regular tori.

5.4.4 Details on transport in the sticky region

The results for the variance and the mean of the Gaussian ensembles presented in Section 5.4.3 suggest two distinct types of transport within the sticky region in frequency space. On the one hand, the Gaussian ensembles exhibit rapid diffusion along the tori with a small drift. On the other hand, a slower subdiffusion perpendicular to the tori is observed. This behavior is independent of the distance to the regular tori. In this section these general statements are complemented with more detailed aspects of the transport in the sticky region. Firstly, the distribution of the trapped orbits in the

sticky region is evaluated. Then, the spreading of the Gaussian ensembles is observed directly in the frequency space.

In the following the distribution $p((x, y), t)$ of a ensemble at different times t is considered. These distributions allow a more detailed investigation of the spreading process than the time dependence of the variance, which is considered in Section 5.4.3. For instance deviations from the Gaussian distribution can be detected. Unfortunately, the 400 points, which are available per ensemble here, see Section 5.4.1, are not enough to form a reasonable distribution in frequency space. Therefore, the integrated distributions $P(x)$ and $P(y)$ are considered here instead, which are defined by

$$P(x) \equiv \int\limits_{y_1}^{y_2} \mathrm{d}y \int\limits_{-T}^{T} \mathrm{d}t\, p((x, y), t)$$

$$P(y) \equiv \int\limits_{x_1}^{x_2} \mathrm{d}x \int\limits_{-T}^{T} \mathrm{d}t\, p((x, y), t)$$

with $T = 5 \cdot 10^7$, $[x_1, x_2] = [-0.001, 0.001]$ and $[y_1, y_2] = [-0.001, 0]$. E.g., $P(y)$ represents the probability that an orbit of the corresponding ensemble is at position y perpendicular to the tori at any time $t \in [-5 \cdot 10^7, 5 \cdot 10^7]$. Only points with coordinates $(x, y) \in [x_1, x_2] \times [y_1, y_2]$ are considered, because in this domain the directions x and y correspond to the local directions along and perpendicular to the tori. Note that the domain restricts the sticky region only along the tori, but not perpendicular to them.

Due to the rapid spreading of the ensembles along the tori, $P(x)$ is distributed almost uniformly apart from small noise-like oscillations and some small peaks at resonance lines. These peaks confirm the accumulation of trapped orbits at resonances as discussed Section 5.3. Hence, the focus here lies on $P(y)$, which is shown for all the Gaussian ensembles in Figures 5.14 and 5.15. The colors indicate the distance of the initial Gaussian ensemble to the tori, as seen in Figure 5.9. The distributions are also ordered by this distance, that is the first row of pictures in Figure 5.14 belongs to the closest ensemble and the last row in Figure 5.15 to the most distant ensemble. Note that smaller values of y mean smaller distance to the tori. The initial region of a ensemble is indicated by the gray box and the mean of $P(y)$ by the black dotted line in the left pictures. Consequently, for ensembles with greater distance to the tori the gray box is located at higher y values. The same is observed for the mean in the figures. However, the shifts of the mean are smaller than the shifts of the initial region. Therefore, for close ensembles the initial region is closer to the tori than the distribution $P(t)$ on average. This situation is reversed for distant ensembles. The fact that both initial region and
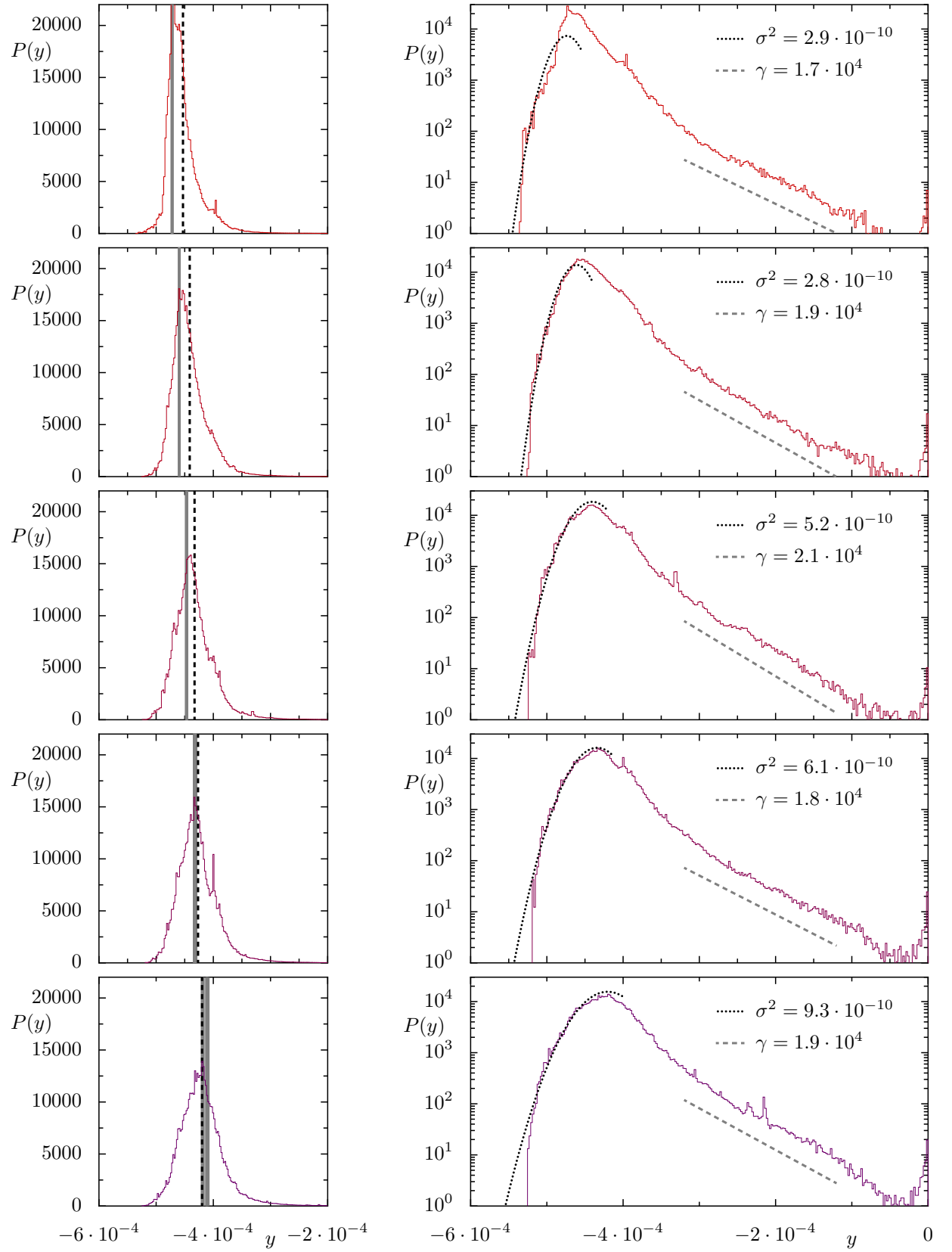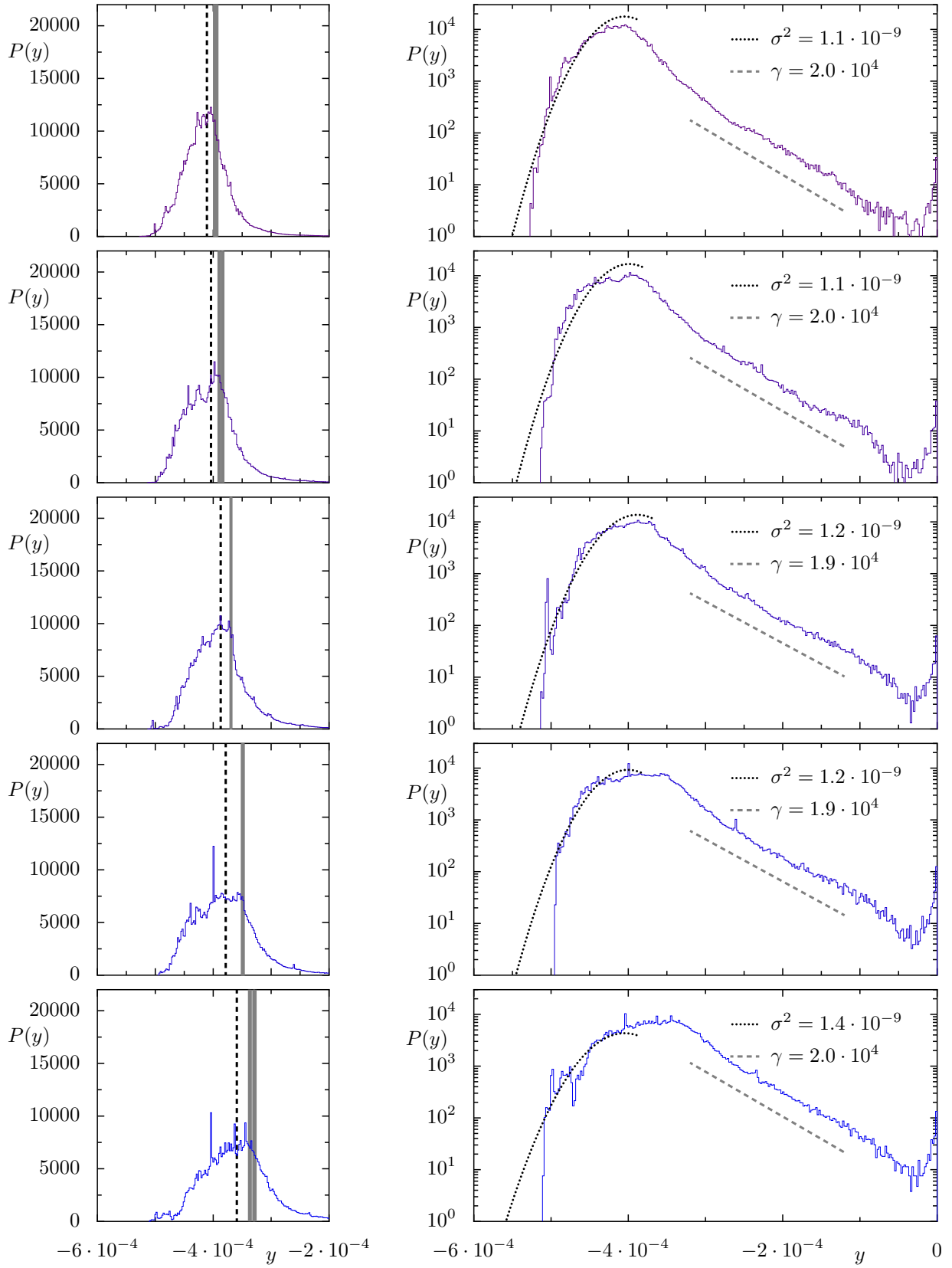
Figure 5.14: Distribution $P(y)$ of points perpendicular to the tori for Gaussian ensembles. The order top-to-bottom row corresponds to the distance small-to-big of the Gaussian ensembles to the tori with colors according to Figure 5.9. $P(y)$ is normed such that the area under the graph is 1. Left column: $P(y)$ with initial region (gray box) and mean $\bar{P}(y)$ (black dotted line); Right column: Same $P(y)$ on log scale with fit $P(y) \sim \exp\left(-(\bar{y}-y)^2/(2\sigma^2)\right)$ (gray dotted line) and fit $P(y) \sim \exp\left(-\gamma y\right)$ (gray dashed line). Figure continues in Figure 5.15

Figure 5.15: Distribution $P(y)$ of points perpendicular to the tori for Gaussian ensembles. The order top-to-bottom row corresponds to the distance small-to-big of the Gaussian ensembles to the tori with colors according to Figure 5.9. $P(y)$ is normed such that the area under the graph is 1. Left column: $P(y)$ with initial region (gray box) and mean $\bar{P}(y)$ (black dotted line); Right column: Same $P(y)$ on log scale with fit $P(y) \sim \exp\left(-(\bar{y} - y)^2/(2\sigma^2)\right)$ (gray dotted line) and fit $P(y) \sim \exp\left(-\gamma y\right)$ (gray dashed line). Figure started in Figure 5.14

mean are not at a similar position means that the spreading of the Gaussian ensembles is anisotropic. Indeed, $P(y)$ is extended much less towards the tori than away from them. Moreover, $P(y)$ looks to the left of its peak like a Gaussian distribution, but decreases more rapidly to the right, see the right column where $P(y)$ is shown with log scale. The dotted and dashed lines represent fits of a Gaussian distribution $P(y) \sim \mathrm{e}^{-\frac{(\bar{y}-y)^2}{2\sigma^2}}$ and an exponential decay $P(y) \sim \mathrm{e}^{-\gamma y}$ respectively.

The exponential decay to the right of the peak is present for all Gaussian ensembles with $\gamma \approx 1.9 \cdot 10^4$. The exponential decay might result from the exit and entry part of the sticky region, which is far away from the tori, as described in Section 5.3.2. Since the sticky region ends there, this part might act as an absorbing boundary.

The Gaussian fit approximates well for the ensembles close to the tori, see Figure 5.14, but less well for the more distant ensembles, see Figure 5.15. The variance σ^2 of the fitted Gaussian distribution is increasing with increasing distance to the tori. This increase is of the same order as the increase of the variance $\sigma_y^2(t)$ of the Gaussian ensembles in Figure 5.12(b) at large times $t \sim 10^6$.

Taking both fits into account, the shape of the distribution $P(y)$ might be the result of a diffusion process with one absorbing boundary far away from the tori. By comparing $P(y)$ with different diffusive systems, a model describing the dynamics within the sticky region might be found. Details of this model can be inferred from the variances $\sigma_y^2(t)$ obtained in Section 5.4.3.

The spreading of the Gaussian ensembles can also be observed directly in frequency space by looking at the positions of the trapped orbits at different times t, see Figure 5.16. Note that each plot represents a time span $\triangle t = 2^{12}$, see Section 3.2.3. Each ensemble has an individual color, i.e. starting with the closest ensemble the colors are black, bright red, dark green, purple, bright blue, dark red, bright gray, dark blue, dark gray, and bright green. For comparison also frequency lines are shown as obtained in Section 5.3.2. The spreading of the ensembles is very rapid in the first time step $T = 0 \ldots 1$ compared to the following time steps. As discussed in Section 5.4.3 the spreading along the tori is much faster than perpendicular to them and becomes faster the further away the ensembles are from the tori. Although the spreading perpendicular to the tori is visible at all positions along the tori, it is partially enhanced by the resonances. This can be seen, e.g., at $T = 2$ at the downside of the bright blue and dark red ensemble, where small bucklings following the resonances $17 : 7 : 7$ and $46 : -2 : 13$ are visible. These bucklings suggest that the points close to the resonance propagate faster towards the tori. This can be explained by Arnold diffusion, see Section 2.6.2. Besides, the ensembles intersect the resonance lines *perpendicular*. Perpendicular refers to the fact that the ensembles look at small times like thin bands, thus can be thought of as
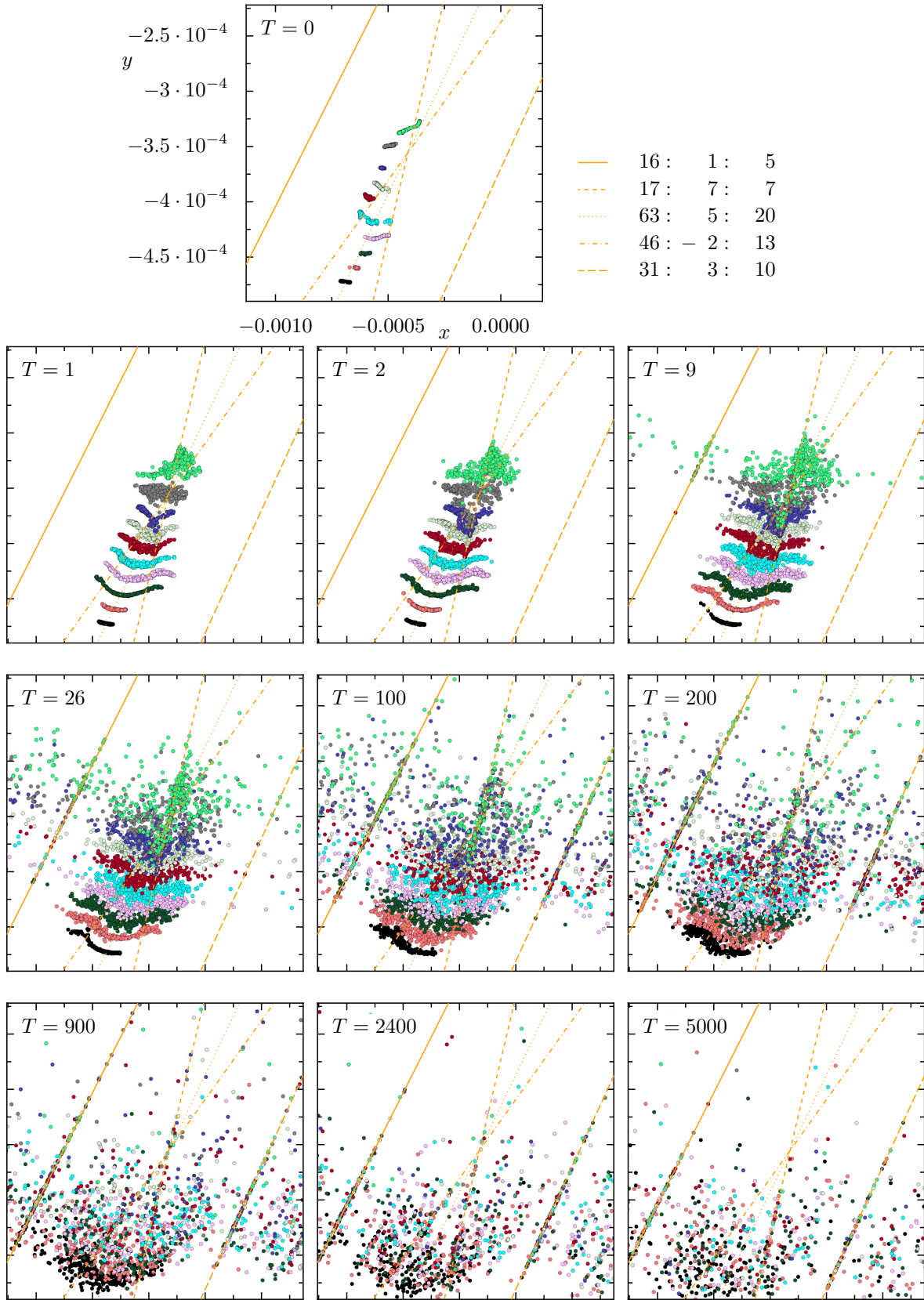
Figure 5.16: Spreading of Gaussian ensembles in frequency space. All plots show the same section of the (x, y) space (see Figure 5.9). Shown are trapped orbits (points, different color for each ensemble) at different time spans $T = t/2^{12}$ (see top left of plots) and resonances (indicated by orange lines)

lines. E.g., at $T = 2$ the dark green ensemble intersects in this sense the resonances $17 : 7 : 7$, $63 : 5 : 20$ and $46 : -2 : 13$ perpendicular. In between the intersections the ensemble is bend such that it looks like a smooth line. This corresponds to transport across overlapping resonance zones, see Section 2.6.2. The orbits can move rapidly perpendicular to the resonances and also from resonance to resonance in case the resonance zones overlap. The resonance zones $16 : 1 : 5$ and $31 : 3 : 10$ are very broad, since also ensembles far away from them bend perpendicular to them. This is visible, e.g., at $T = 9$ for the bright red ensemble which bends directly at the left of the resonance $46 : -2 : 13$ perpendicular to the resonance $16 : 1 : 5$. Also at larger times $T \geq 26$ the major resonances $16 : 1 : 5$ and $31 : 3 : 10$ to have a band-shaped region around them, which contain less points than the regions next to them. These bands indicate probably the width of the resonance zones of the major resonances. In contrast to the bands surrounding them the major resonances accumulate a lot of orbits, as seen for larger times $T \geq 26$. It is not clear at the moment if the behavior at these major resonances is a physical phenomenon or a numerical artifact. Recall that always $\triangle t = 2^{12}$ iterations of a chaotic orbit give one frequency, see Section 3.2.3. Thus, in frequency space a point of a chaotic orbit represents a time average of the orbit. Consequently, for chaotic orbit oscillating very rapidly around a resonance the computed frequencies will always lie on the resonance, because these frequencies correspond to its average behavior in phase space.

Besides, only some dynamics seen in the sticky region in Figure 5.16 can be explained with the transport in resonance zones, see Section 2.6.2. E.g., at $T = 9$ the bright green orbits also propagate in an area, which cannot be assigned to one of the major resonance zones $16 : 1 : 5$ or $17 : 7 : 7$. As seen in Figure 5.8, there are not enough relevant resonances to cover the whole sticky region. Nevertheless, trapped orbits are found in almost every part of the sticky region and the spreading of the Gaussian ensembles looks similar in regions inside and outside of resonance zones. Furthermore, as mentioned in the discussion of Figure 5.8 the resonances in the sticky region are not confined by KAM tori as it is typically the case for resonances of the Arnold web. The remaining KAM tori are far away, thus it is not clear why these resonances influence the propagation of the trapped orbits at all.

6 Summary and outlook

In this thesis the trapping of chaotic orbits in 4D symplectic maps is investigated. The global structure of the regular tori is explained and sticky regions are found close to the boundary of these structures. The transport properties of the sticky region are quantified in frequency space and related to known diffusion phenomena associated with resonances. In this context, a combination of phase-space visualizations and frequency analysis proves to be effective for the study of systems with two degrees of freedom. Moreover, conceptual issues of Laskar's frequency analysis are discussed and resolved for some cases. The results are used to apply the frequency analysis to strongly perturbed systems.

The global structure of the regular tori is found to be based on one parameter families of central 1D tori. Each central 1D torus is surrounded by layers of 2D tori. An algorithm is devised which approximates for any 2D torus the corresponding central 1D torus. The resulting families of 1D tori turn out to be either the remains of resonant tori or center manifolds. These center manifolds exist beyond major resonance gaps. While the usual algebraic approximations of center manifolds fail at these resonance gaps, the developed algorithm represents a more effective method to numerically obtain center manifolds of a system.

Chaotic orbits are observed to be trapped close to the boundary of the regular structures. By a systematic search for trapped orbits a thin layer around the regular structures is identified as a sticky region. The transport within the sticky region is analyzed by examining the spreading of Gaussian ensembles in frequency space. The transport is classified into two directions. The transport along the regular tori is diffusive and the transport perpendicular to them is subdiffusive. An ensemble of resonance zones influences the dynamics via Arnold diffusion and resonance overlap. These observations in phase space and in frequency space suggest that the trapping is not caused by a hierarchical structure as in 2D. Instead, a possible interpretation is that the ensemble of resonance zones combines into a large sticky region.

Future studies in higher dimensional systems should determine the relevance of the resonance zones for the trapping. The role of Arnold diffusion is still unclear for strongly perturbed systems as there the resonance zones are not enclosed by regular tori. Con-

sequently, the mechanism by which these resonance zones influence the dynamics has to be understood. Finally, the entry and exit to the sticky region has to be investigated in order to completely reveal the trapping mechanism in higher dimensional systems. Future investigations can use the promising approach of ensembles of trapped orbits in frequency space to answer these questions.

A Appendix

A.1 Analysis of fractal dimensions

In Section 5.2.2 the dimension of the trapped orbits is qualitatively observed to be about three, which is less than the dimension of the 4D phase space. This speculation has to be quantified. For this purpose the *box-counting dimension* D_{Box} of the computed trapped orbits is determined [19].

The following procedure is conducted for every trapped orbit. A natural number $M \in \mathbb{N}$ is chosen, which defines

$$\epsilon \equiv \frac{1}{M}$$

with $0 < \epsilon \le 1$. Then each coordinate p_1, p_2, q_1, and q_w is uniformly decomposed into M intervals of length ϵ such that the 4D phase space, which is here $[0,1)^4$, is uniformly decomposed into M^4 4D cubes, denoted as boxes. For each ϵ the number of boxes $N(\epsilon)$, that contain a point of the trapped orbit, is counted. Examples for the shape of $N(\epsilon)$ are portrayed in Figure A.1. With decreasing ϵ the number of boxes $N(\epsilon)$ increases exhibiting a power-law behavior,

$$N(\epsilon) \sim \left(\frac{1}{\epsilon}\right)^{D_{\mathrm{Box}}}, \tag{A.1}$$

for some part of the domain. For even smaller ϵ it turns into a asymptotic curve, approaching the number of points belonging to the trapped orbit. The box-counting dimension D_{Box} is defined as the exponent of the power-law Eq. (A.1) within the corresponding interval of $1/\epsilon$. For objects of dimension $D \in \mathbb{N}$ the box-counting dimension D_{Box} matches this dimension, $D_{\mathrm{Box}} = D$.

As only the trapping process is of interest, the analysis is restricted to the middle third of each orbit such that the entry and exit segments are ignored. After experimenting with some orbits, the calculation is automated with the following parameters, denoting the length of the orbit by T and the shortest used interval length by ϵ_{Min} :

30 values for $1/\epsilon$ are used, which are uniformly distributed on a logarithmic scale with

$$1/\epsilon \in \left[3, \sqrt[4]{T/3} \cdot 10^3\right].$$

In order to ensure that the domain of $1/\epsilon$ contains the power-law all orbits for which

$$\frac{N(\epsilon_{\text{Min}}) - T/3}{T/3} > 0.1\%, \tag{A.2}$$

are sorted out. The condition of Eq. (A.2) is based on the fact, that for a sufficient big $1/\epsilon_{\text{Min}}$ the number of boxes $N(\epsilon_{\text{Min}})$ approximates the length of the orbit. The interval of $1/\epsilon$, in which the power-law is fitted, is such that the corresponding $N(\epsilon)$

$$N(\epsilon) \in \left[100, N(\epsilon_{\text{Min}})/10\right].$$

In order to ensure that this fit interval leads to reasonable results all orbits are sorted out for which the interval covers less than two magnitudes of $1/\epsilon$ or contains less than ten calculated points $N(\epsilon)$. Furthermore, all orbits are sorted out for which the points $N(\epsilon)$ in the fit interval deviate to much from a power-law. This deviation is evaluated by comparing the linear fit $f(\log 1/\epsilon)$ and the points $\log N(\epsilon)$, i.e., all points are sorted out for which

$$\sqrt{1/L \cdot \sum_{i=1}^{L} \left(f\left(\log \frac{1}{\epsilon_i}\right) - \log N\left(\epsilon_i\right)\right)^2} \; > \; 0.06,$$

where L is the number of fitted points.

The procedure is applied to the trapped orbits of the 2D standard map in the same manner, except for the interval of $1/\epsilon$, which is in this case

$$1/\epsilon \in \left[3, \sqrt{T/3} \cdot 10^4\right],$$

in order to use Eq. (A.2) accordingly.

Examples for the results of the automated process are depicted in Figure A.1. The resulting $N(\epsilon)$ are depicted as blue points and the automated fit is shown as gray line on the fitting interval. Most results look like Figures A.1(a) and A.1(b). In most of the 4D cases the automated fit works well, as seen in Figure A.1(a), whereas in some cases the fit is slightly off, as seen in Figure A.1(b). In the 2D cases $N(\epsilon)$ sometimes exhibits the power-law behavior on a small interval, as well as several different power laws, as seen in Figure A.1(c). Thus, the numerical setup as described allows only a rough estimate

(a) Fit optimal

(b) Fit not optimal

(c) Several D_{Box}
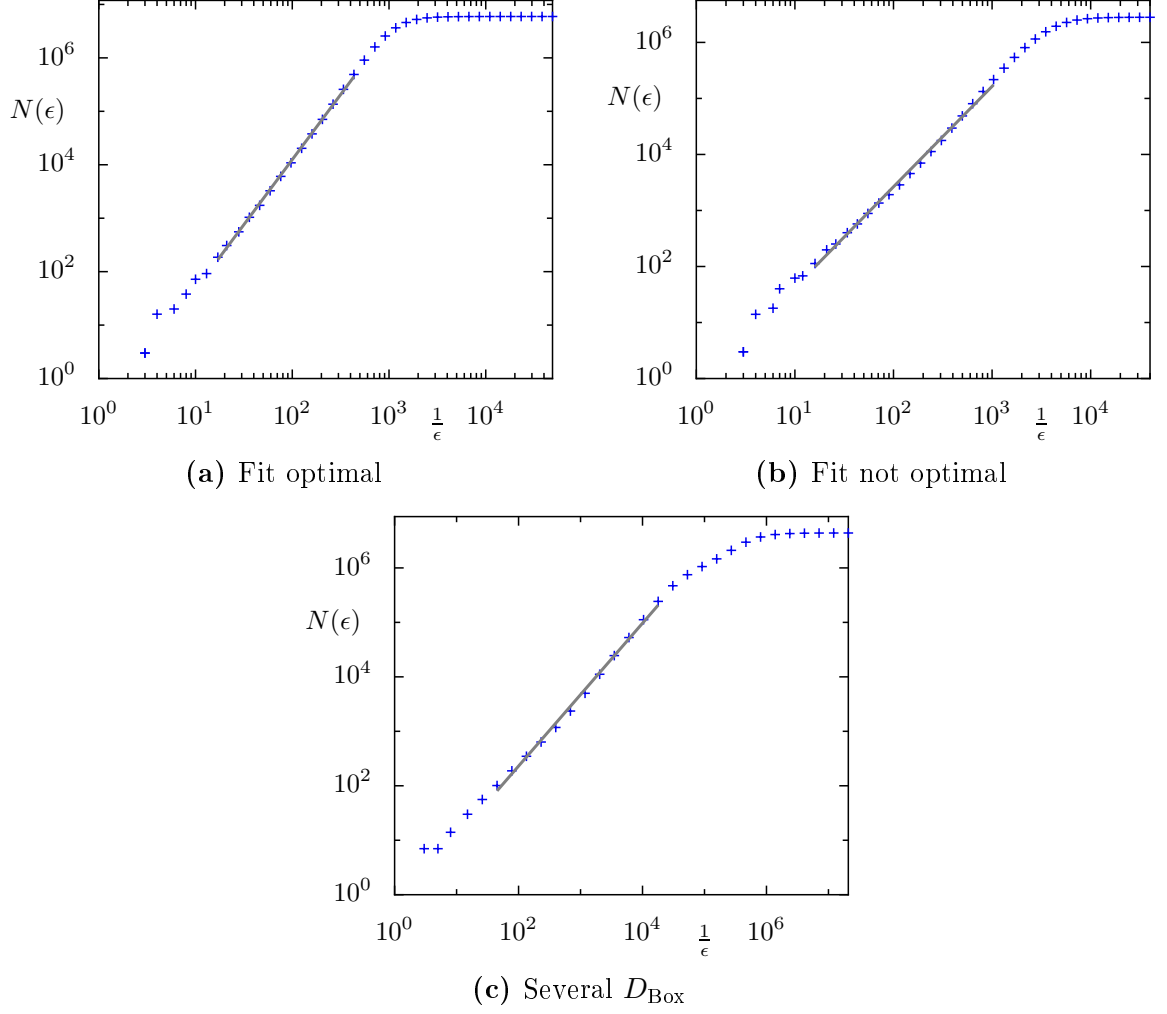
Figure A.1: Examples for automated box-counting dimension D_{Box} evaluation for (a, b) the 4D map F_{SC} and (c) the 2D map F_{2D}. The obtained $N(\epsilon)$ (blue crosses) and the fitted power-law (gray line) within the used fit interval are shown. (a) shows an example of an optimal fit, (b) shows an example of a fit, whose fit interval starts and ends at to small values of $1/\epsilon$, and (c) shows an example of calculated points, which exhibit two different power laws at different scale, thus not allow a correct fit.

of the box-counting dimension D_{Box}. Nevertheless, in all spot tests the deviation from a D_{Box}, whose fit interval is chosen by hand, is smaller than 0.05. Therefore, the statistics of the box-counting dimensions D_{Box} of the trapped orbits only deal with dimensions rounded to a tenth. However, this accuracy is sufficient for the purpose of determining, whether the orbits are on average trapped in a four, three or less dimensional region.

The statistics of the trapped orbits of F_{SC} and F_{2D} considered in Section 5.2 are presented in Figure A.2. The statistics for D_{Box} for the 4D map F_{SC} in Figure A.2(a) approximates a Gaussian distribution with a peak around $D_{\text{Box}} = 2.3$. The calculated dimensions range from 1.6 to 2.6. This suggests that the dimension of the trapped orbits tends to be less than four or even less than three in some cases. On the contrary the statistics in the 2D map F_{2D} in Figure A.2(b) has a sharp peak around $D_{\text{Box}} = 1.2$ with dimensions ranging from 0.9 to 1.3. This is also much less than the expected dimension two, which is the dimension of the available phase space. Moreover the ranges and the mean are about half of the values for the 4D case. In both cases the region, the orbits are trapped in, seem to have a fractal dimension much smaller than the dimension of the phase space. It should be pointed out, that the application of the box-counting method here has numerical limitations due to the limited number of available points within the trapped region. These limitations have not been taken into account. For example many of the orbits with $D_{\text{Box}} \leq 2$ that are examined more closely, turn out to be trapped in a region consisting of several very small disjoint subregions, which look rather like 2D objects in the phase-space section. In these cases the presented box-counting algorithm mainly resolves the dimension resulting from several point-like subregions ignoring the dimension of these subregions. This is because the power-law resulting from the dimension of the subregions is only visible at much larger values of $1/\epsilon$. The number of points in these subregions is insufficient to resolve $N(\epsilon)$. Besides in some cases, primarily for the 2D map F_{2D}, more than one power-law behavior each with a different exponent D_{Box} is found, see, e.g., Figure A.1(c).

To summarize, the analysis of the fractal dimension of trapped orbits in the 4D map F_{SC} shows that the trapped orbits are heavily confined at least in one dimension. This statement is supported by the results presented in Sections 5.3 and 5.4.
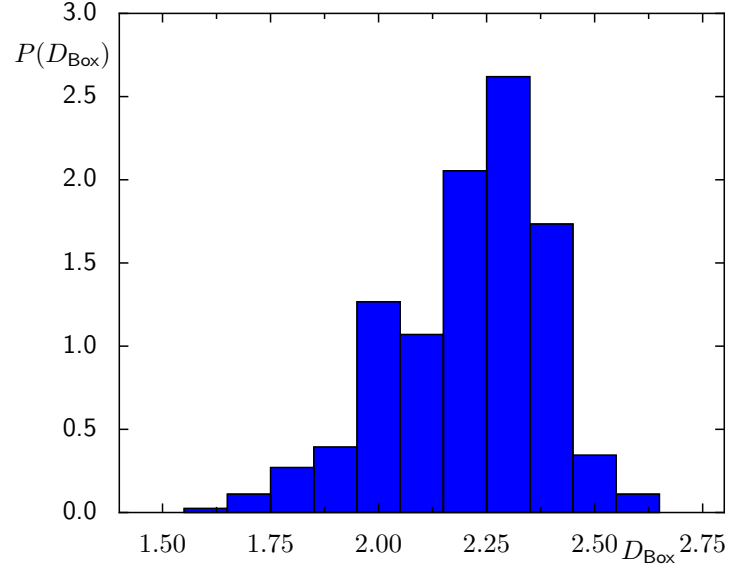
(a) 4D map, F_{SC}: D_{Box} for 813 trapped orbits
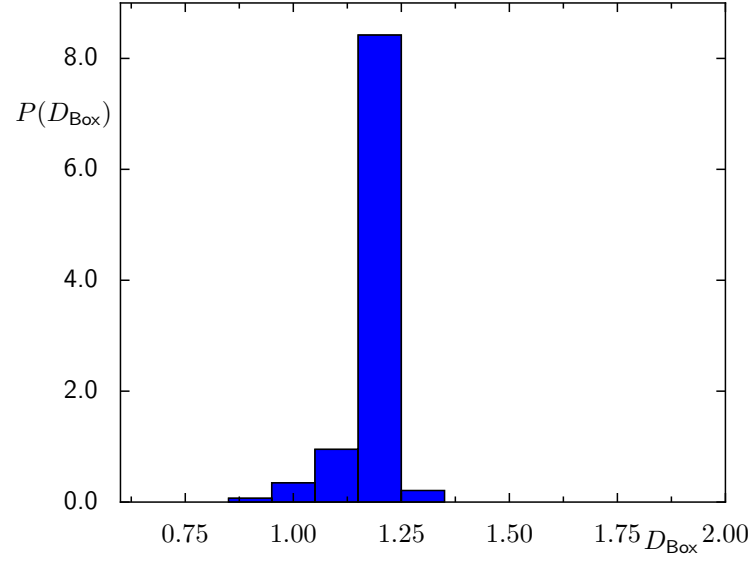
(b) 2D map $F_{2\mathrm{D}}$: D_{Box} for 431 trapped orbits

Figure A.2: Statistics $P(D_{\mathrm{Box}})$ of the box-counting dimension D_{Box} of the middle third of trapped orbits. The evaluated D_{Box} is rounded to a tenth, $P(D_{\mathrm{Box}})$ is normed such that the area under the graph is 1.

A.2 Results for weakly coupled standard map F_{WC}

In this section the results for the weakly coupled standard map F_{WC} are briefly presented. The results are obtained accordingly to the results of the strongly coupled standard map F_{SC} presented in the previous chapters. For further details and discussion it is referred to the corresponding sections in these chapters.

In Figure A.3 the Poincaré recurrence statistics $P(t)$ for F_{WC} are shown according to Section 5.1.

In Figure A.4 a gallery of trapped orbits for F_{WC} is shown according to Section 5.2.1.

In Figure A.5 the central 1D tori for F_{WC} are shown according to Section 4.3. Much more invariant manifolds are visible than for F_{SC}. Also one of the center manifolds of the central elliptic–elliptic fixed point is located almost completely within the (p_1, q_1)-plane, which is indicated by the 2D area of black intersection points in Figure A.5(a). This is due to the small perturbation of the system. The manifolds of the period 4 island chain are missing accordingly to the discussion of disjoint islands in Section 4.2.3.

In Figure A.6 the statistics of the box-counting dimension D_{Box} of trapped orbits for F_{WC} are shown according to appendix A.1. The peak at $D_{\mathrm{Box}} = 2.7$ is absent for F_{SC}. All orbits belonging to this peak that are visualized in phase space turn out to be of the type shown in Figure A.4(a).
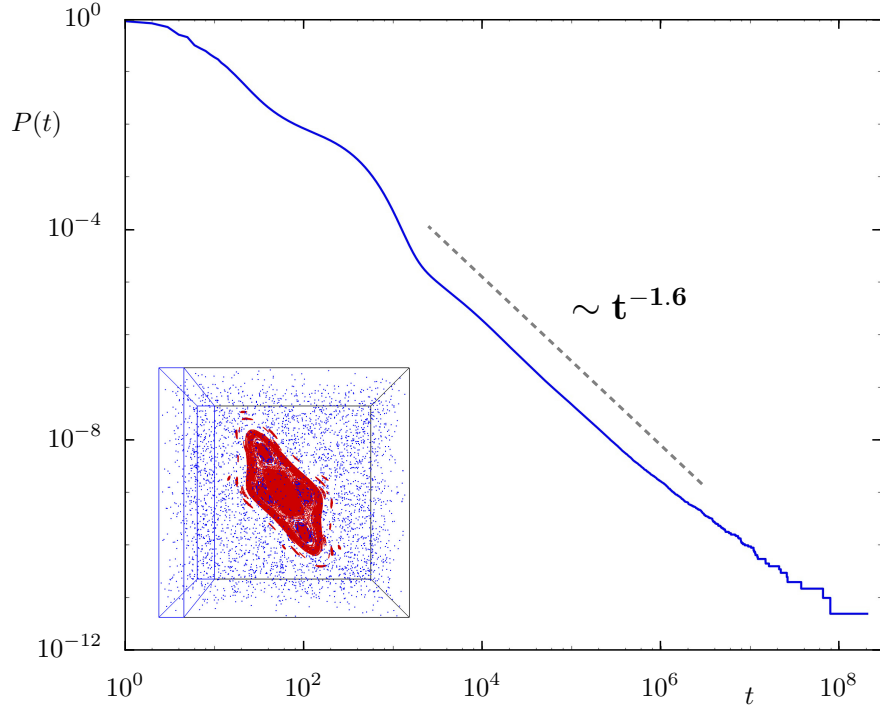
Figure A.3: Dependence of statistics of Poincaré recurrences $P(t)$ on time t for the 4D map F_{WC}, see Eq. (2.13). For comparison the gray dashed line represents a power-law $P(t) \sim t^{-\gamma}$, with $\gamma = 1.6$. The exponent obtained by fitting is $\gamma_{\mathrm{fit}} = 1.57$. The inset sketches the position of the initial region Γ (blue box) in form of a phase space section $|p_2| < 10^{-5}$, see Section 3.1, with regular tori (red) and a trapped orbit (blue).

(a) $T \approx 13 \cdot 10^6$

(b) $T \approx 18 \cdot 10^6$

(c) $T \approx 360 \cdot 10^6$

(d) $T \approx 94 \cdot 10^6$

(e) $T \approx 15 \cdot 10^6$
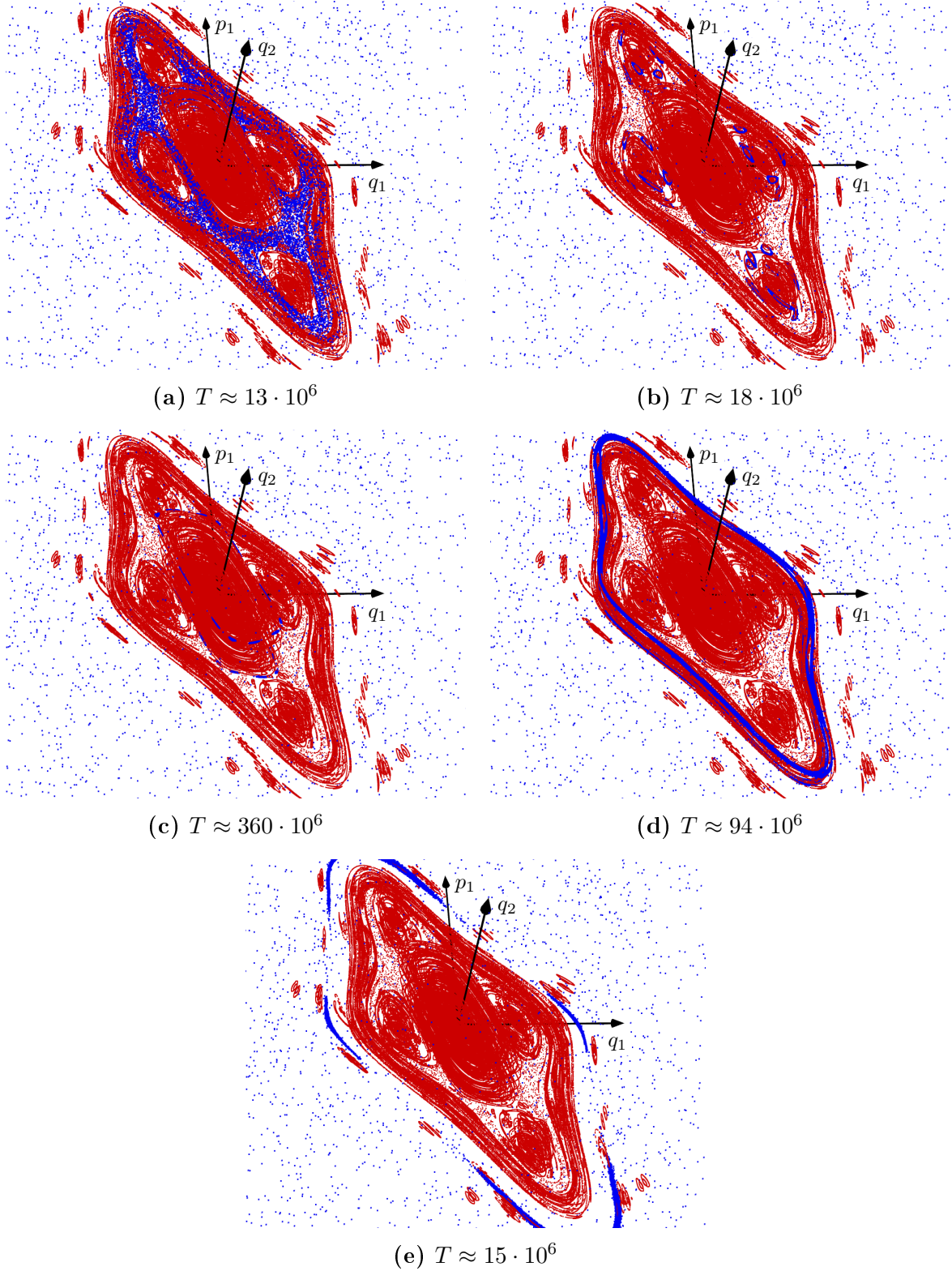
Figure A.4: Examples for trapped orbits of the 4D map F_{WC}, see Eq. (2.13). Shown is the section $|p_2| < \epsilon$, with regular tori (red, $\epsilon = 10^{-5}$) and example of a trapped orbit (blue, $\epsilon = 10^{-4}$). The captions contain the time T till the first return
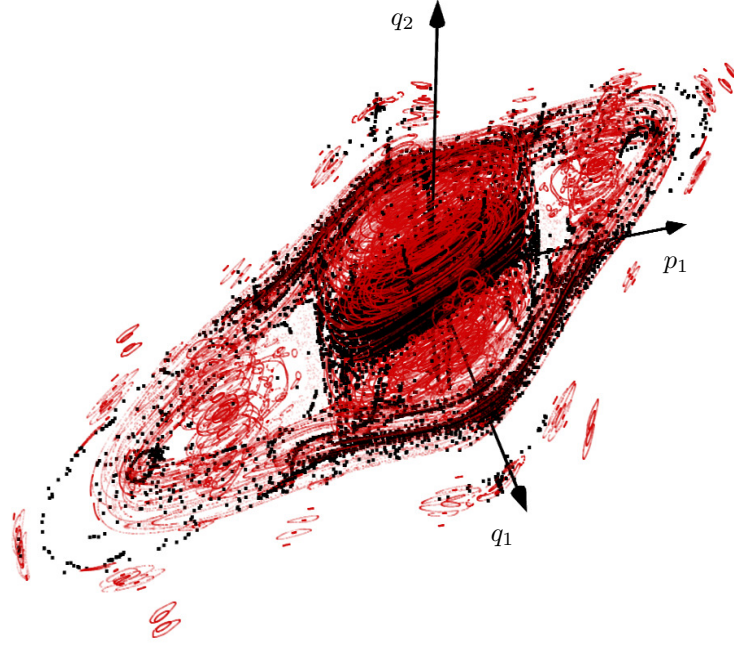
(a) Phase space section, $|p_2| < \epsilon$
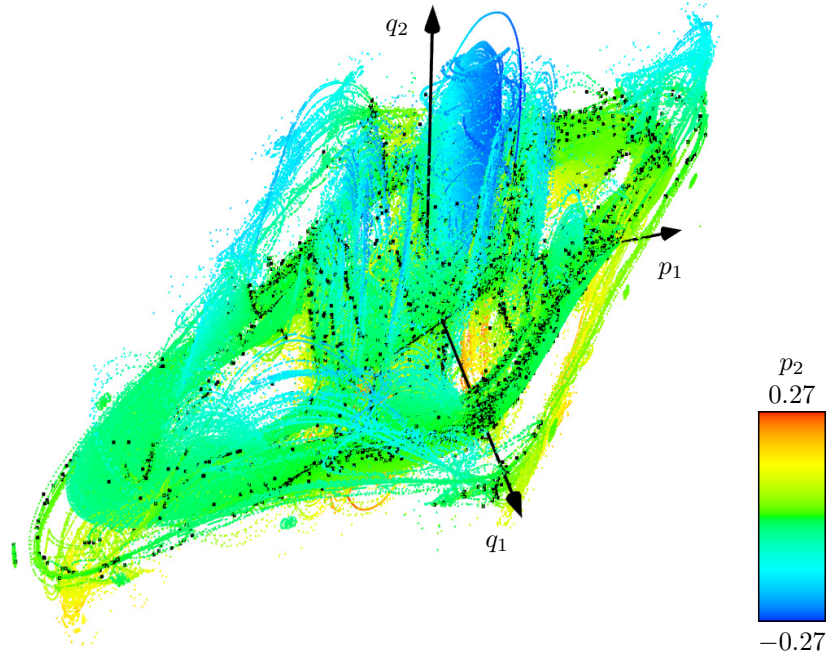
(b) Projection

Figure A.5: Central 1D tori of F_{WC} in the phase-space section $|p_2| < \epsilon$ (see Section 3.1.3) and projected to the (p_1, q_1, q_2)-space (see Section 3.1.2). (a) The phase-space section shows the central 1D tori (black points) and regular tori (red). (b) For comparison in the projection the intersection points (black) of the central 1D tori with the phase-space section are depicted.
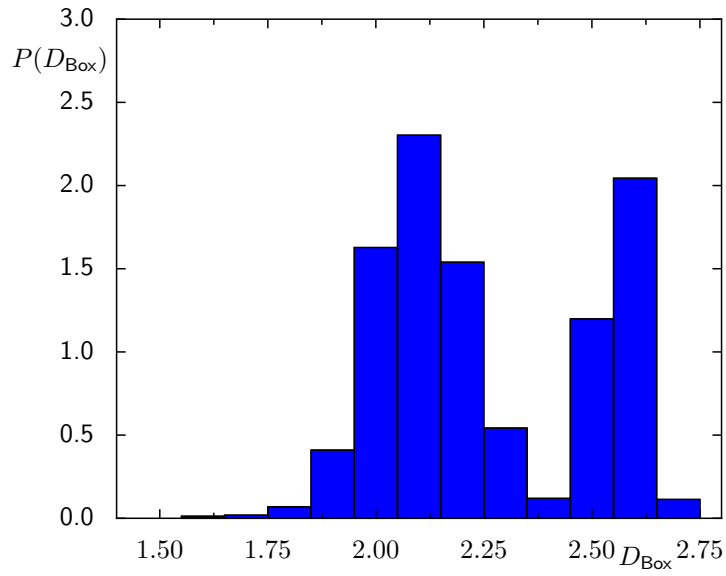
Figure A.6: Statistics $P(D_{\mathrm{Box}})$ of the box-counting dimension D_{Box} of the middle third of 1585 trapped orbitsof the 4D map F_{2D}. The evaluated D_{Box} is rounded to a tenth, $P(D_{\mathrm{Box}})$ is normed such that the area under the graph is 1.

List of Figures

Bibliography

[1] E. N. Lorenz: *Deterministic nonperiodic flow*, J. Atm. Sci. **20** (1963), 130–141.

[2] C. Martens, M. Davis, and G. Ezra: *Pathways for Energy Redistribution and Phase Space Bottlenecks in Many–Dimensional Systems*, unpublished, see `http://www.chem.cornell.edu/gse1/ocs_2.pdf`.

[3] R. W. Easton, J. D. Meiss, and S. Carver: *Exit times and transport for symplectic twist maps*, Chaos **3** (1993), 153–165.

[4] K. Kaneko and R. J. Bagley: *Arnold Diffusion, Ergodicity, and Intermittency in Coupled Standard Mapping*, Phys. Lett. **110A** (1985), 435–440.

[5] H.-t. Kook and J. D. Meiss: *Diffusion in symplectic maps*, Phys. Rev. A **41** (1990), 4143–4150.

[6] H. Poincaré: *Sur le problème des trois corps et les équations de la dynamique*, Acta Math. **13** (1890).

[7] J. D. Meiss: *Average exit time for volume-preserving maps*, Chaos **7** (1997), 139–147.

[8] B. V. Chirikov and D. L. Shepelyansky: *Statistics of Poincaré Recurrences and the Structure of the Stochastic Layer of a Nonlinear Resonance*, Tech. Rep. PPPL–TRANS–133, Princeton Univ., (1983).

[9] R. S. MacKay, J. D. Meiss, and I. C. Percival: *Transport in Hamiltonian systems*, Physica D **13** (1984), 55–81.

[10] G. Györgyi, F. H. Ling, and G. Schmidt: *Torus structure in higher-dimensional Hamiltonian systems*, Phys. Rev. A **40** (1989), 5311–5318.

[11] E. Todesco: *Analysis of resonant structures of four-dimensional symplectic mappings, using normal forms*, Phys. Rev. E **50** (1994), R4298–R4301.

[12] V. I. Arnold: *Instability of dynamical systems with several degrees of freedom*, Sov. Math. Dokl. **6** (1964), 581–585.

[13] B. V. Chirikov: *A universal instability of many-dimensional oscillator systems*, Phys. Rep. **52** (1979), 263–379.

[14] J. Laskar: *Frequency analysis for multi-dimensional systems: global dynamics and diffusion*, Physica D **67** (1993), 257–281.

[15] S. Wiggins: *On the geometry of transport in phase space I. Transport in k-degree-of-freedom Hamiltonian systems, $2 \leq k < \infty$*, Physica D **44** (1990), 471 – 501.

[16] C. Martens, M. Davis, and G. Ezra: *Local frequency analysis of chaotic motion in multidimensional systems: energy transport and bottlenecks in planar OCS*, Chem. Phys. Lett. **142** (1987), 519–528.

[17] S. Kim and S. Ostlund: *Simultaneous rational approximations in the study of dynamical systems*, Phys. Rev. A **34** (1985), 3426–3434.

[18] L. Markus and K. R. Meyer: *Generic Hamiltonian Dynamical Systems are neither Integrable nor Ergodic*, no. 144 in Mem. Amer. Math. Soc., (American Mathematical Society, Providence, Rhode Island), (1974).

[19] E. Ott: *Chaos in Dynamical Systems*, (Cambrige University Press, The Pitt Building, Trumpington Street, Cambrige, United Kingdom), 2nd edn., (2002).

[20] M. Michler: *Neue Methoden zur Bestimmung der Verteilung Poincaré'scher Rückkehrzeiten*, Diploma thesis, Technische Universität Dresden, Fachrichtung Physik, (2007).

[21] V. I. Arnold and A. Avez: *Ergodic Problems of Classical Mechanics*, (Benjamin, NewYork), (1968).

[22] I. P. Cornfeld, S. V. Fomin, and Ya. G. Sinai: *Ergodic Theory*, no. 245 in Grundlehren der Mathematischen Wissenschaften, (Springer Verlag, New York), (1982).

[23] C. F. F. Karney: *Long-time correlations in the stochastic regime*, Physica D **8** (1983), 360–380.

[24] B. V. Chirikov and D. L. Shepelyansky: *Correlation properties of dynamical chaos in Hamiltonian systems*, Physica D **13** (1984), 395–400.

[25] J. D. Meiss and E. Ott: *Markov-Tree Model of Intrinsic Transport in Hamiltonian Systems*, Phys. Rev. Lett. **55** (1985), 2741–2744.

[26] J. D. Meiss and E. Ott: *Markov Tree Model of Transport in Area-Preserving Maps*, Physica D **20** (1986), 387–402.

[27] B. V. Chirikov and D. L. Shepelyansky: *Chirikov and Shepelyansky Reply:*, Phys. Rev. Lett. **89** (2002), 239402.

[28] G. Cristadoro and R. Ketzmerick: *Universality of Algebraic Decays in Hamiltonian Systems*, Phys. Rev. Lett. **100** (2008), 184101.

[29] R. Artuso and C. Manchein: *Instability statistics and mixing rates*, Phys. Rev. E **80** (2009), 036210.

[30] F. Christiansen and P. Grassberger: *Escape and sensitive dependence on initial conditions in a symplectic repeller*, Physics Letters A **181** (1993), 47 – 53.

[31] E. G. Altmann and H. Kantz: *Hypothesis of strong chaos and anomalous diffusion in coupled symplectic maps*, EPL (Europhysics Letters) **78** (2007), 10008 (5pp).

[32] D. L. Shepelyansky: *Poincaré recurrences in Hamiltonian systems with a few degrees of freedom*, Phys. Rev. E **82** (2010), 055202.

[33] A. J. Lichtenberg and M. A. Liebermann: *Regular and chaotic dynamics*, (Springer–Verlag, New York), 2nd edn., (1992).

[34] R. S. MacKay, J. D. Meiss, and I. C. Percival: *Stochasticity and Transport in Hamiltonian Systems*, Phys. Rev. Lett. **52** (1984), 697–700.

[35] J. Meiss: *Symplectic maps, variational principles, and transport*, Rev. Mod. Phys. **64** (1992), 795–848.

[36] A. M. Ozorio de Almeida: *Hamiltonian Systems: Chaos and Quantization*, (Cambridge University Press, Cambridge), (1988).

[37] J. Moser and E. J. Zehnder: *Note on dynamical systems*, (American Mathematical Society, Rhode Island), 1st edn., (2005).

[38] D. K. Arrowsmith and C. M. Place: *an introduction to Dynamical Systems*, (Cambridge University Press, Cambrige), 3rd edn., (1994).

[39] S. M. Graff: *On the conservation of hyperbolic invariant tori for Hamiltonian systems*, J. Differ. Equations **15** (1974), 1–69.

[40] S. Wiggins: *Normally hyperbolic invariant manifolds in dynamical systems*, (Springer–Verlag, Berlin), 1st edn., (1994).

[41] À. Haro: *Center and center-(un)stable manifolds of elliptic-hyperbolic fixed points of 4D-symplectic maps. An example: The Froeschlé map*, in: *Hamiltonian Systems with Three or More Degrees of Freedom*, 403–407, (1999).

[42] M. Jolly and R. Rosa: *Computation of non-smooth local centre manifolds*, J. Num. Anal. **25** (2005), 698–725.

[43] À. Jorba: *Numerical Computation of Normal Forms, Centre Manifolds and First Integrals of Hamiltonian Systems*, Experimental Mathematics **8** (1999), 155–195.

[44] E. Lega, M. Guzzo, and C. Froeschlé: *Detection of Arnold diffusion in Hamiltonian systems*, Physica D **182** (2003), 179–187.

[45] J. M. Greene: *A method for determining a stochastic transition*, J. Math. Phys. **20** (1979), 1183–1201.

[46] S. Honjo and K. Kaneko: *Is Arnold diffusion relevant to global diffusion?*, in: *Over the resonance, 35th Symposium on Celestial Mechanics* (Eds. E. Kokubo, H. Arakida and T. Yamamoto), 367–376, (2003).

[47] R. E. Gillilan and W. P. Reinhardt: *Barrier recrossing in surface diffusion: A phase-space perspective*, Chem. Phys. Lett. **156** (1989), 478 – 482.

[48] R. E. Gillilan: *Invariant surfaces and phase space flux in three-dimensional surface diffusion*, J. Chem. Phys. **93** (1990), 5300.

[49] R. E. Gillilan and G. S. Ezra: *Transport and turnstiles in multidimensional Hamiltonian mappings for unimolecular fragmentation: Application to van der Waals predissociation*, J. Chem. Phys. **94** (1991), 2648.

[50] S. Honjo and K. Kaneko: *Structure of Resonances and Transport in Multidimensional Hamiltonian Dynamical Systems*, in: *Geometric Structures of Phase Space in Multidimensional Chaos*, 437–463. John Wiley & Sons, Inc., (2005).

[51] Y.-S. Sun and Y.-N. Fu: *Diffusion Character in Four-Dimensional Volume-Preserving Map*, Celest. Mech. Dyn. Astr. **73** (1999), 249–258, 10.1023/A:1008315601491.

[52] C. Froeschlé: *On the number of isolating integrals in systems with three degrees of freedom*, Astrophysics and Space Science **14** (1971), 110–117.

[53] B. P. Wood, A. J. Lichtenberg, and M. A. Lieberman: *Arnold diffusion in weakly coupled standard maps*, Phys. Rev. A **42** (1990), 5885–5893.

[54] B. P. Wood, A. J. Lichtenberg, and M. A. Lieberman: *Arnold and Arnold-like diffusion in many dimensions*, Physica D **71** (1994), 132–145.

[55] K. Richter and D. Wintgen: *Stable planetary atom configurations*, Phys. Rev. Lett. **65** (1990), 1965–1965.

[56] M. Katsanikas, P. A. Patsis, and A. D. Pinotsis: *Chains of rotational tori and filamentary structures close to high multiplicity periodic orbits in a 3D galactic potential*, arxiv:nlin.CD/1103.3981 (2011).

[57] C. Froeschlé: *Numerical Study of a Four-Dimensional Mapping*, Astron. Astrophys. **16** (1972), 172–189.

[58] M. Richter: *Classical and quantum investigations of four-dimensional maps with a mixed phase space*, Ph.D. thesis, Technische Universität Dresden, Fachrichtung Physik, (2012).

[59] J. Laskar: *The chaotic motion of the solar system: A numerical estimate of the size of the chaotic zones*, Icarus **88** (1990), 266–291.

[60] J. Laskar: *Frequency analysis of a dynamical system*, Celest. Mech. Dyn. Astr. **56** (1993), 191–196.

[61] A. Bazzani, L. Bongini, and G. Turchetti: *Analysis of resonances in action space for symplectic maps*, Phys. Rev. E **57** (1998), 1178–1180.

[62] F. Onken: *Fraktale Strukturen im 4D-Phasenraum der stark gekoppelten Standardabbildung*, Bachelor thesis, Technische Universität Dresden, Fachrichtung Physik, (2012).

[63] R. Bartolini, A. Bazzani, M. Giovannozzi, W. Scandale, and E. Todesco: *Tune evaluation in simulations and experiments*, Part. Accel. **52** (1996), 147–177.

[64] C. Froeschlé, M. Guzzo, and E. Lega: *Graphical Evolution of the Arnold Web: From Order to Chaos*, Science **289** (2000), 2108–2110.

Acknowledgments

It is a pleasure to thank Prof. Dr. Roland Ketzmerick for this interesting research project, valuable discussions, and his continuous support.

I am truly indebted and thankful to my supervisor Martin Richter for his support, the many stimulating discussions, his continuous encouragement, and his patient way of explaining. I benefited a lot from his physical knowledge and his numerical and IT skills.

I thank Dr. Arndt Bäcker, Dr. Matthias Michler, Martin Körber, Falk Haßler, Stefan Majewsky, Clemens Löbner, Franziska Onken, Norman Mertig, and Dr. Steffen Löck for helpful discussions and comments during several stages of this work.

I am particularly grateful to Martin Richter, Clemens Löbner, Dr. Steffen Löck, Dr. Arndt Bäcker, Martin Körber, and Norman Mertig for proof-reading parts of this thesis.

Furthermore, I thank all members of the computational physics group and the secretary G. Schädlich for the pleasant work atmosphere.

Especially I would like to thank my parents for their support during the past years.

I owe sincere and earnest thankfulness to my girlfriend Lena Engemann for understanding my temporal lack of time and the affecting care with which she was concerned about me eating, drinking, and sleeping properly.

Finally, I am obliged to my roommates for proving that even after a long day in the office there is a life apart from physics.

Erklärung

Hiermit erkläre ich, dass ich die vorliegende Arbeit im Rahmen der Betreuung im Institut für Theoretische Physik ohne unzulässige Hilfe Dritter verfasst. Die aus fremden Quellen direkt oder indirekt übernommenen Gedanken sind als solche gekennzeichnet. Die Arbeit wurde bisher weder im Inland noch im Ausland in gleicher oder ähnlicher Form einer anderen Prüfungsbehörde vorgelegt.

Steffen Lange
Dresden, 25. Mai 2012